

UNIVERSITY OF BELGRADE
SCHOOL OF ELECTRICAL ENGINEERING

Nikola N. Vuković

Risken-Nummedal-Graham-Haken
instabilities and self-pulsing in
quantum cascade lasers

Doctoral Dissertation

Belgrade, 2018

УНИВЕРЗИТЕТ У БЕОГРАДУ
ЕЛЕКТРОТЕХНИЧКИ ФАКУЛТЕТ

Никола Н. Вуковић

Рискен-Нумедал-Грахам-Хакен
нестабилности и само-пулсирање у
квантним каскадним ласерима

докторска дисертација

Београд, 2018

Ментор:

др Јелена Радовановић, редовни професор
Универзитет у Београду – Електротехнички факултет

Чланови комисије:

др Витомир Милановић, професор емеритус
Универзитет у Београду – Електротехнички факултет

др Љупчо Хаџиевски, научни саветник
Универзитет у Београду – Институт за нуклеарне науке Винча

др Владимир Арсоки, доцент
Универзитет у Београду – Електротехнички факултет

др Ненад Цакић, редовни професор
Универзитет у Београду – Електротехнички факултет

Датум одбране: _____

Acknowledgments

I was privileged to work with two great professors, my advisor Dr. Jelena Radovanovic, and Dr. Vitomir Milanovic. I have learnt a great deal from them and I am deeply influenced by their enthusiasm, magnetic personalities and open-mindedness which makes working with them a very rewarding process. I also thank them for their great support and perseverance during the whole process of applying for Teaching Assistant position at School of Electrical Engineering.

I would like to give special thanks to Dr. Dmitri L. Boiko from Centre Suisse d'Electronique et de Microtechnique (CSEM), Neuchâtel (Switzerland) who was FastIQ project leader and my host at CSEM during three short term scientific missions. It was my privilege to collaborate and to learn so much from him. I not only have learned a great deal scientifically from him, but am also deeply influenced by his enthusiasm and broad interests in science. I hope that we will continue our collaboration in the future.

I would like to thank Dr. Ljupco Hadzievski from Vinca Institute of Nuclear Sciences, III 45010 project leader; prof. Dragan Indjin from University of Leeds, UK, Chair of COST ACTION BM1205; prof. Mauro Pereira from Sheffield Hallam University, UK, Chair of COST ACTION MP1204; Dr. Aleksandar Danicic with whom I was privileged to work in the beginning of my PhD studies.

I would like to acknowledge support from Swiss National Science Foundation project "Ultrafast Infrared Emitter on a Quantum Cascade – FastIQ" (SCOPES 2013-2016: Joint Research Projects) (SNSF)(IZ73Z0_152761); Ministry of Education, Science and Technological Development (Republic of Serbia), (III 45010); European Cooperation in Science and Technology (COST) ACTIONs BM1205 ("European Network for Skin Cancer Detection using Laser Imaging") and MP1204 ("TERA-MIR Radiation: Materials, Generation, Detection and Applications").

I would also like to thank my family and friends for their support and encouragement, and believing in me.

Risken-Nummedal-Graham-Haken instabilities and self-pulsing in quantum cascade lasers

Abstract

A theoretical study on low-threshold multimode instabilities in quantum cascade lasers (QCLs) with Fabry-Pérot cavity is presented. Previously, low threshold Risken-Nummedal-Graham-Haken (RNGH) instabilities were reported in several experimental investigations of QCLs. They were attributed so far to the combined effect of the induced grating of carrier population and of a built-in saturable absorption feature that may be present in the monolithic single-section cavity of QCLs. Here we show that low-threshold RNGH instabilities in QCLs occur due to a combined effect of the carrier coherence grating and carrier population grating induced in the gain medium and not due to an intracavity saturable absorption. We find that QCLs with a few mm long cavity exhibit intermittent RNGH self-pulsations while regular self-pulsations are possible in short-cavity QCLs, with the cavity length of 100 μm or smaller. We examine a transient behavior to RNGH self-pulsations in short-cavity QCLs and find features that resemble cooperative superradiance. Our findings open a practical way of achieving ultra-short pulse production regimes in the mid-infrared spectral range. Applying same approach to semiconductor laser diodes (LDs) we explain the absence of RNGH self-pulsation in single-section LDs based on a quantum well gain media, while practically established method for reaching the ultrafast coherent emission regimes in LDs is to incorporate a separately contacted saturable absorber section in the LD cavity.

Furthermore, we have obtained a closed-form expression for the threshold of RNGH multimode instability in a Fabry-Pérot (FP) cavity quantum cascade

laser which can easily be applied in practical situations which require analysis of QCL dynamic behavior and estimation of its RNGH multimode instability threshold. In the model, the RNGH instability threshold is analyzed using a second-order biorthogonal perturbation theory and we confirm our analytical solution by a comparison with the numerical simulations and experimental data available in the literature.

In this dissertation RNGH self-pulsations in external cavity QCLs are also analyzed. On one hand, the propagation time in the external cavity (the pulse delay time) serves to provide a memory effect and is thus expected to improve coherence for long QCL samples otherwise suffering from formation of incoherent domains. On the other hand, in short QCL chips, the external cavity is expected to reduce the repetition rate of self-pulsations.

Keywords: Quantum cascade laser, laser stability, instabilities and chaos, ultrafast nonlinear optics, external cavity

Scientific field: Electrical and Computer Engineering

Specific topic: Nanoelectronics and Photonics

UDC number: 621.3

Рискен-Нумедал-Грахам-Хакен нестабилности и само-пулсирање у квантним каскадним ласерима

Сажетак

Приказано је теоријско истраживање мултимодних нестабилности са ниским прагом у квантним каскадним ласерима (ККЛ). Претходно су у више експерименталних студија о ККЛ-у уочене нестабилности Рискен-Нумедал-Грахам-Хакен (РНГХ) типа мало изнад ласерског прага. До сада је њихова појава приписивана комбинованом ефекту индуковане решетке популације носилаца и сатурабилном апсорберу који је присутан у монолитној ласерској шупљини Фабри-Перо типа сачињеној од једне секције. У дисертацији ће бити показано да се РНГХ нестабилности са ниским прагом код ККЛ-а јављају услед комбинованог ефекта решетке поларизације носилаца и решетке популације носилаца које су индуковане у појачавачком медијуму, а не услед сатурабилне апсорпције у ласерској шупљини. Показаће се да ККЛ чија је ласерска шупљина дугачка неколико милиметара испољава нерегуларне РНГХ само-пулсације, док су регуларне само-пулсације могуће код ККЛ са кратком ласерском шупљином чија је дужина 100 μm или краћа. Испитујемо транзијентни режим до РНГХ само-пулсација код ККЛ са кратком ласерском шупљином и проналазимо понашање које подсећа на кооперативну суперрадијансу. Наша истраживања отварају практичне могућности за остваривање режима ултра-кратких импулса у средњем инфрацрвеном делу спектра. Када исти приступ применимо на полупроводничке ласерске диоде (ЛД) можемо да објаснимо одсуство РНГХ само-пулсација код ласерских диода сачињених од једне секције базиране на појачавачком медијуму сачињеном од квантних јама, док је проверени метод за реализацију ултра-брзе кохерентне емисије код ЛД

да се инкорпорира посебна секција са сатурабилним апсорбером унутар шупљине ласерске диоде.

Поред тога, извели смо израз за праг мултимодних нестабилности РНГХ типа код ККЛ-а са Фабри-Перо шупљином, који се може једноставно применити у практичним ситуацијама које захтевају анализу динамичког понашања ККЛ-а и процену прага РНГХ мултимодних нестабилности. У моделу је праг за РНГХ нестабилности анализиран коришћењем биортогоналне теорије пертурбација и потврђена је валидност аналитичког решења поређењем са нумеричким симулацијама и експерименталним подацима доступним у литератури.

У овој дисертацији су анализирани и само-пулсације РНГХ типа код ККЛ-а у конфигурацији са екстерном ласерском шупљином. Са једне стране, време пропагације у екстерној шупљини (време кашњења импулса) служи да обезбеди меморијски ефекат и очекује се да може да побољша кохеренцију код дугих узорака ККЛ-а који иначе имају непогодност узроковану формирањем некохерентних домена. Са друге стране, код кратких ККЛ чипова очекује се да екстерна шупљина смањи фреквенцију само-пулсација.

Кључне речи: Квантни каскадни ласер, стабилност ласера, нестабилности и хаос, ултрабрза нелинеарна оптика, екстерна шупљина

Научна област: Електротехника и рачунарство

Ужа научна област: Наноелектроника и фотоника

УДК број: 621.3

Contents

1. Introduction	1
2. Model description	8
2.1. QCL laser as a model system for RNGH instabilities	8
2.2. Travelling wave rate equation model.....	11
2.3. Approximation of coupled-mode rate equation model.....	12
2.4. Linear stability analysis	15
3. RNGH self-pulsations in monolithic QCL chip.....	24
3.1. RNGH instability threshold	24
3.2. Experimental observations of RNGH instability in QCLs	31
3.3. RNGH instability in a QCL with long cavity	36
3.4. RNGH instability in a QCL with short cavity	46
3.5. Comment on coherence length.....	49
3.6. The role of carrier diffusion	53
3.7. The role of carrier population and carrier coherence gratings	60
4. Analytical expression for RNGH instability threshold in QCLs.....	66
4.1. Second-order biorthogonal perturbation theory	67
4.2. Validation of the analytic solution for the RNGH instability threshold	72
4.3. Link to the original RNGH theory	80
5. Regular self-pulsations in external cavity MIR Fabry-Pérot quantum cascade lasers.....	83
5.1. Motivation for inclusion of an external cavity	84
5.2. Model system	86
5.3. Numerical results for 100 μm chip.....	88
5.3.1. Standalone QCL.....	88

5.3.2. QCL in ~mm long external cavity	92
5.3.3. QCL in ~cm long EC	97
5.4. Numerical results for long QCL chip in EC configuration.....	102
5.4.1. Pulse correction with a two-beam interference.....	107
6. Conclusion.....	109
References.....	111
Appendix A.....	122
Appendix B.....	127
Appendix C.....	129
Appendix D.....	133
Appendix E.....	142
Appendix F.....	144
Appendix G.....	145
Biographical details (in Serbian)	147
Списак публикација	149

1. Introduction

Following the first demonstration at Bell Labs in 1994 by F. Capasso and J. Faist [1], quantum cascade lasers (QCLs) have experienced rapid and dramatic improvements in operating temperature [2], output power [3], efficiency and wavelength span [4], [5]. At room temperature, continuous wave output powers of several W can now routinely be achieved in the mid-infrared (MIR) spectral range [3], and widely tunable designs are available [6]. Wall-plug efficiencies of 50% have been demonstrated at cryogenic temperatures [7], [8] and up to 27% at room temperature [3]. Commercial QCLs and QCL-based systems are already available from various companies [9], [10], [11]. Continuously operating QCLs in the MIR (3.5-20 μm) have important applications in security, health, gas sensing and gas analysis [10], [12]. Production of frequency combs in QCLs has been demonstrated and proven to be very promising for spectroscopic applications [13]. Yet, QCL potential as a versatile spectroscopic tool could be significantly enhanced if operation in the ultra-short pulse regime would be possible. Such regime would enable time-resolved spectroscopic measurements in MIR and far-infrared (FIR) ranges for a wide spread of applications such as LIDARs (Light Detection and Ranging), Earth observation, environmental remote sensing of molecules, in particular, of greenhouse gases, high-speed QCL based communications utilizing the atmospheric transmission windows of 3-5 μm or 8-12 μm and many more [14]-[20].

However, ultrafast carrier relaxation at picosecond time scale prohibits passive mode-locking or Q-switching operation in QCLs because of the cavity round-trip time being longer than the gain recovery time [21]–[23]. Therefore gain switched pulse production has been attempted, yielding 120 ps pulse width [24]. On the other hand, active mode-locking was achieved in QCLs utilizing diagonal transition (“superdiagonal” gain structure), with the upper state lifetime being increased to 50 ps so as to match the cavity round-trip time [25], [26]. Stable operation with these devices was obtained by current modulation of only a short section of the waveguide, while the whole waveguide was biased slightly above threshold (see also [27]). Nevertheless, the diagonal transition renders QCL operation temperature out of the practical use. Self-induced transparency together with a fast saturable absorber was proposed in [28] to be used to passively mode lock QCLs.

Another promising approach to generate short MIR pulses has emerged from experimental observations that some of CW operating QCL samples exhibit features of low-threshold [29] Risken-Nummedal-Graham-Haken (RNGH) multimode instabilities [30], [31] and hence they might be capable of producing ultra-fast self-pulsations. However, the second-order interferometric autocorrelation measurements have shown that the output optical pulses have significant stochastic constituent [26], if these autocorrelation traces should be attributed to coherence spikes at all . In order to confirm RNGH instability and to understand conditions for reaching regular self-pulsation in QCLs, one should figure out the origin of such low second threshold in these lasers.

In general, the multimode RNGH instabilities are related to a non-adiabatic [32] behavior of the medium polarization, excitation of rapid coupled oscillations of the medium polarization P and population inversion N . They show up as self-pulsations in the output laser emission, whereas the optical

spectrum is expected to be split in two mode clusters (sidebands) with frequency separation of the order of the Rabi oscillation frequency.

Below the RNGH instability threshold, the optical mode is fully controlled by the laser cavity. The buildup of Rabi oscillations at above the second threshold indicates that now a medium macroscopic polarization (coherence) has the major impact on the optical field in the laser cavity. The original RNGH theory, which was established for a CW operating *unidirectional ring laser*, requires the pump rates of at least 9 times above the lasing threshold in order for multimode instability to occur.

However, the experiments revealed a different second threshold behavior. In [33], a ring-cavity dye laser with homogeneously broadened gain line has shown RNGH-like multimode instability at small excess above the lasing threshold. More specifically, quenching of the main lasing mode and excitation of two optical sidebands was observed at 1.2 times above the lasing threshold. The frequency separation of the sidebands was close to the Rabi oscillation frequency or one of its sub-harmonics and it was increasing with the pump rate. Later on, there were several claims on RNGH instabilities in CW operating Er^{3+} doped ring fiber lasers [34], [35], [36], and ring Nd:YAG lasers [37]. However, interpretation of these experimental observations remained doubtful. Since the period of self-pulsations was close to the cavity round-trip time they were attributed to mode-locking phenomena. Most unexpectedly, the self-pulsations were occurring almost at the lasing threshold, contrary to the theoretical predictions for at least 9-fold excess above the lasing threshold. Note that the relaxation T_1 and dephasing T_2 times in the active gain media of these lasers are relatively long as compared to their semiconductor counterparts and hence their Rabi oscillation frequencies are low. It was understood that (i) the cavity length must be made very long in order to match the intermodal frequency separation to that of the Rabi

oscillations, and (ii) the lowering of second threshold in Er^{3+} doped ring fiber lasers can be attributed to a 3-level structure of the optical transitions in Er^{3+} ions [38]. Nevertheless, the fact of experimental observation of RNGH instability remained debatable.

Ten years later, a clear Rabi frequency splitting between two clusters of modes was observed in the lasing spectra of CW operating QCLs [29], indicating multimode RNGH instability in these *Fabry-Pérot (FP) cavity lasers*. Interestingly, the RNGH instability was observed both in ridge waveguide QCLs and in buried heterostructure QCLs. Although the role of spatial hole burning (SHB) effect in lowering the second threshold was understood, it was thought [39] that the low-threshold RNGH instability does not occur just as a result of the induced grating of carrier population. Therefore, an additional assumption was made in [39] on a built-in saturable absorber in the cavity of QCL, allowing for a reduction of the 2nd threshold from 9-fold excess to about 1.1 times above the lasing threshold. As a matter of fact, the saturable absorber has been shown to lower the instability threshold in a CW ring laser [40]. However, the nature of saturable absorption in QCLs has never been fully clarified [12]. In particular, the authors in [39] have evoked the Kerr lensing effect as a possible mechanism responsible for the saturable absorption. In case of narrow ridge waveguide lasers, due to overlap of the waveguide mode tails and the metal contact deposited on the waveguide, the Kerr lensing may indeed lead to saturable absorption. However, it cannot produce the saturable absorption effect of the same strength in buried heterostructure QCLs. At the same time low-threshold RNGH instability was observed in both ridge waveguide and buried heterostructure QCLs.

An alternative approach to explain the unusually low RNGH instability threshold in QCLs was proposed in [41]. The idea stems from a parametric gain picture yielding instability of the main cavity mode, along the line of

comb generation in optically pumped dielectric micro-disk resonators with third-order $\chi^{(3)}$ non-linearity. MIR intersubband transitions in semiconductor QWs do produce strong third-order nonlinearity [42], [43]. However, optically passive microdisk resonators have special cavity design in order to reach parametric instability threshold. In particular they employ whispering gallery modes with very small transverse size, very high quality factor ($Q \sim 10^8$) and operate with circulating pump power in the resonator on the order of several hundreds of watts [44]. Electrically pumped MIR QCLs with FP cavities cannot reproduce such environment and reach parametric instability caused by material third-order nonlinearity $\chi^{(3)}$.

The origin of instability in [41] was attributed to parametric gain for an offset frequency wavelets co-propagating in the gain medium which is subjected to saturation by the main lasing mode. Essentially this consideration is based on a lumped gain rate equation model for a laser in which spatial hole burning is introduced in a phenomenological way. Apart from a lumped gain picture, this approach is conceptually identical to the original one by Risken and Nummedal [30] who consider propagation of perturbation wavelets in the traveling wave picture. The results reported in [41] agree with experimental observations, however, phenomenologically introduced spatial hole burning effect masks certain important points of the analysis and hence it leaves space for further study of the subject.

In this dissertation, another alternative model for low-threshold multimode RNGH instability in a QCL *without saturable absorber* is presented [45], [46]. The model *provides a strict consideration of the saturation and spatial modulation effects in the traveling wave picture*. This is a more realistic representation for a monolithic single-section *FP cavity laser*. Technically, a set of important corrections to the original treatment [30], [31], [39] was made. It consists in (i) accounting for the induced carrier coherence grating alongside with the carrier

population grating and in (ii) accounting for the carrier diffusion process that leads to relaxation of both gratings. In contrast to the lumped gain in [41], we will utilize travelling wave picture and clarify the role of carrier coherence grating.

The outcomes of the analysis for the second threshold in QCLs are in perfect agreement with the numerical simulations based on a travelling wave (TW) rate equation model [45], [47] as well as with the experimental data available in the literature [29], [39], [48]. Interestingly, we find that regular self-pulsations at picosecond time scale are possible in short-cavity QCLs. Our model also explains the nonexistence of multimode RNGH instability in quantum well (QW) laser diodes (LDs).

The model can also be adapted for the case of external cavity configuration, following the approach from [47] where one section provides description for the pulse propagation and amplification in the gain chip and another one describes pulse propagation in external cavity without interaction with the active medium [49], [50]. In this dissertation we propose to use external cavity (EC) QCLs in order to obtain regular RNGH self-pulsations with lower repetition rate compared to the case of monolithic QCL chip.

This dissertation is organized in the following manner: In Chapter 2 we introduce QCL as a model system and start from the Maxwell-Bloch equations for a Fabri-Perot cavity and use approximation of coupled mode model. Chapter 3 addresses the second threshold conditions and discusses the RNGH instability in long-cavity and short-cavity devices, as well as the importance of the carrier diffusion effects in QCLs and conventional LDs. In Chapter 4 we derive an analytical expression for RNGH threshold in QCL and make a link with the original theory. In Chapter 5 we elucidate the possibility of regular RNGH self-pulsations in external cavity quantum cascade laser and analyze

the periodicity of the output power waveforms. Chapter 6 summarizes the results presented in the dissertation.

2. Model description

2.1. QCL laser as a model system for RNGH instabilities

A quantum cascade laser is a unipolar device based on intersubband transitions. Its active region consists of a large number of periodically repeated epilayers. Each period (stage) comprises a gain and injection/relaxation regions. While the gain region serves to create a population inversion between the two levels of the lasing transition, the purpose of the injection/relaxation region is to depopulate the lower lasing level and to provide injection of electrons in the upper lasing level of the next stage [11], [12].

A careful design of the quantized states in the QCL heterostructure is essential for the development and optimization of experimental QCLs since the lasing frequency is determined by the energy difference between the upper and lower laser level and a careful energy alignment of the levels is necessary for an efficient injection into the upper (laser) level and depopulation of the lower level. Likewise, careful engineering of the wave functions is necessary because it governs the strength of both the optical and nonradiative transitions. The eigenenergies and wave functions are determined by solving the stationary Schrödinger equation or, if space charge effects are taken into account, the Schrödinger-Poisson equation system [11]. Widely used numerical approaches for solving the one-dimensional effective mass Schrödinger equation include

the transfer matrix method [11], [51], [52] and finite difference scheme [11], [53]. Effects such as nonparabolicity [54] can be included more easily into the transfer matrix approach [55], [56].

Although QCLs have a complicated structure of epilayers, it was understood and confirmed experimentally that the internal structure does not alter directly the appearance of multimode RNGH instabilities and that a semiclassical model with effective parameters of the laser gain medium suffices [27], [39].

Alongside with the studies of RNGH instabilities in InGaAs QCLs, we will apply our analytic model [46] (see Chapter 4) to QW LDs based on AlGaAs and InGaN alloys. For all of them we assume a simple single-section Fabry-Pérot (FP) cavity design. The parameters of the model for three types of lasers considered here are summarized in Table 1.

Table 1. Dynamic model parameters for QCL and QW LDs considered in this study [45], [57].

Parameter	Name	InGaAs QCL	AlGaAs QW LD	InGaN QW LD
λ	Lasing wavelength	10 μm	850 nm	420 nm
T_1	Carrier lifetime	1.3 ps		1-2 ns
T_2	Carrier dephasing time	140 fs		100 fs
T_{2_eff}	Effective carrier dephasing time in the presence of diffusion	138 fs	86 fs	84 fs
T_g	Relaxation time of the carrier population grating	0.927 ps	0.158 ps	0.13 ps
T_{2_g}	Relaxation time of the coherence grating	128 fs	41 fs	37 fs
α_i	Intrinsic material loss	24 cm^{-1}	5 cm^{-1}	35 cm^{-1}

D	Diffusion coefficient	180 cm ² /s	20 cm ² /s (ambipolar)	7 cm ² /s (ambipolar)
n _g	Group refractive index	3.3	3.8	3.5
R ₁ , R ₂	Cavity facet reflection coefficients	27%	27%	18 %
Γ	Optical mode confinement factor	0.5	0.01	0.02
∂g/∂n	Differential material gain	2.1×10 ⁻⁴ cm ³ /s	1×10 ⁻⁶ cm ³ /s	2.2×10 ⁻⁶ cm ³ /s
n _t	Transparency carrier density	7×10 ¹⁴ cm ⁻³	2×10 ¹⁸ cm ⁻³	1.6×10 ¹⁹ cm ⁻³

As a model system for RNGH instability, we consider an InGaAs QCL with a direct transition, having the carrier lifetime (longitudinal relaxation time) T_1 of about one picosecond. This is much smaller than the cavity round-trip time. As in the case of heterostructure epilayers, we do not examine any particular lateral cavity design since it was shown experimentally that the laser design (ridge waveguide [39] or buried heterostructure [29]) has no or little impact on the RNGH instability in QCLs. Although our QCL model parameters are slightly different from the ones in Ref. [39], this difference has no impact on the main conclusions of the dissertation, in particular, regarding the occurrence of low-threshold RNGH instability. In the table, the optical mode confinement factor and transparency carrier density for QCL are defined using the overall thickness of epilayers in the period. In Section 3.6 we apply our model to AlGaAs QW LDs and InGaN QW LDs (last two columns in Table 1) with the objective to verify the model agreement with experimental observations that single-section QW LDs do not reveal any feature of RNGH instability [45], [46], [58].

For all model systems considered here, the photon lifetime in the cavity exceeds the dephasing time (transverse relaxation time) T_2 , so the dynamic

behavior reported here is intrinsically different from the Class-D laser dynamics discussed in [59], [60].

2.2. Travelling wave rate equation model

As a starting point of our analysis we use semiclassical Maxwell-Bloch (MB) equations for a two-level system. Following along the lines of the approaches in [61], [62] and accounting for the diffusion term in the Schrödinger equation [63], we obtain the following system of rate equations (see Appendix A):

$$\partial_t \rho_{ab} = i\omega \rho_{ab} + i \frac{\mu E}{\hbar} \Delta - \frac{\rho_{ab}}{T_2} + D \partial_z^2 \rho_{ab} \quad (2.1)$$

$$\partial_t \Delta = -2i \frac{\mu E}{\hbar} (\rho_{ab}^* - \rho_{ab}) + \frac{\Delta_{pump} - \Delta}{T_1} + D \partial_z^2 \Delta \quad (2.2)$$

$$\partial_z^2 E - \frac{n_g^2}{c^2} \partial_t^2 E = \Gamma \frac{N\mu}{\epsilon_0 c^2} \partial_t^2 (\rho_{ab}^* + \rho_{ab}) + \frac{n_g l'_0}{c} \partial_t E \quad (2.3)$$

where $\rho_{ab} = \rho_{ba}^*$ is the off-diagonal element of the density matrix, the non-equilibrium carrier density $N\Delta = N(\rho_{bb} - \rho_{aa})$ is represented as the population inversion between the upper (index “ bb ”) and lower (index “ aa ”) levels of the lasing transition, $N\mu(\rho_{ab}^* + \rho_{ab})$ is the active medium polarization (“coherence”). Furthermore, ω and μ denote the resonant frequency and the dipole matrix element of the lasing transition, respectively, T_1 and T_2 are the longitudinal and transverse relaxation times, $N\Delta_{pump}/T_1$ is the pump rate due to injection of electrons into the upper lasing level, N is defined by the doping density in the injector region and D is the diffusion coefficient for electrons in the plane of active QWs of the QCL structure (for a LD, the ambipolar diffusion coefficient for the holes and electrons is used instead). E , Γ and n_g

stand for the cavity mode electric field, the overlap between the optical mode and the active region, and the group refractive index for the cavity mode, respectively. Note that the differential material gain is $\partial g / \partial n = \omega T_2 \mu^2 / \hbar n_g^2 \epsilon_0$ and l'_0 is the linear loss coefficient. The difference between our MB equations for QCLs and equations used in [27], [39] is the coherence diffusion term $D \partial_z^2 \rho_{ab}$ that appears in (2.1). Numerical simulations with the travelling wave rate equation model reported below were accomplished by introducing in (2.1)-(2.3) two slowly varying amplitudes for the counter propagating waves in the Fabry-Perot (FP) cavity and distinguishing the medium's polarizations associated with the forward and backward traveling waves as in [47].

2.3. Approximation of coupled-mode rate equation model

The system of MB equations (2.1)-(2.3) is not ideally suited for analytical study on multimode RNGH instability. In Ref [64] a comprehensive approach for analysis of multimode instabilities in a ring laser was established using a truncated set of coupled-mode equations. A similar approach was applied in [39] for the case of FP-cavity QCLs. However, the key point of such truncated modal expansion is to take into account all coupled harmonics *in a self-consistent way* [64]. We argue that the previous theoretical treatment of RNGH instabilities in QCLs [39] does not take into account the spatial harmonics of induced macroscopic polarization of the gain medium *in the FP-cavity laser or bidirectional ring laser*. As a result, in the limit of adiabatic elimination of the medium polarization, the truncated set of coupled-mode equations from [39] does not agree with well-established models for a Class-B laser dynamics [65]. (See discussion of equations (2.7)-(2.11) below and also the Appendix B. We stress that our considerations for *bidirectional ring lasers* and *FP cavity lasers* can by no means be applied to the *unidirectional ring laser* considered in Refs. [30],

[31]. Furthermore, in order to match the experimentally measured second threshold of $\sim 1.1 I_{\text{th}}$ (I_{th} is the lasing threshold pump current), the model in [39] assumes that there is a built-in saturable absorber in the monolithic cavity of QCL due to the Kerr lensing effect. As a matter of fact, the saturable absorber does lower the RNGH instability threshold in a CW laser [40]. However, in the buried heterostructure QCLs, which also exhibit low second threshold, the proposed Kerr-lensing mechanism for saturable absorption has never been unambiguously confirmed [12].

In order to elucidate another possible origin of the low-threshold RNGH instability, we have expanded the MB equations (2.1)-(2.3) into a truncated set of self-consistent coupled mode equations. The waves traveling in the two directions are coupled as they share the same gain medium and this gives rise to SHB effect [66]: the standing wave formed by a cavity mode imprints a grating in the gain medium through gain saturation resulting in other modes becoming more favorable for lasing and triggering of multimode operation. Our analysis of the SHB effect has shown that as soon as the spatial grating of carrier population is taken into account (the terms Δ_2^\pm below), the third-order spatial harmonics of the induced macroscopic polarization grating (the terms η_{++} and η_{--} below) have to be accounted for in the coupled-mode expansion:

$$E(z,t) = \frac{1}{2} \left[E_+^*(z,t) e^{-i(\omega t - kz)} + E_+(z,t) e^{i(\omega t - kz)} \right] + \frac{1}{2} \left[E_-^*(z,t) e^{-i(\omega t + kz)} + E_-(z,t) e^{i(\omega t + kz)} \right] \quad (2.4)$$

$$\rho_{ab}(z,t) = \left(\eta_+(z,t) + \eta_{++}(z,t) e^{-2ikz} \right) e^{i(\omega t - kz)} + \left(\eta_-(z,t) + \eta_{--}(z,t) e^{2ikz} \right) e^{i(\omega t + kz)} \quad (2.5)$$

$$\Delta(z,t) = \Delta_0(z,t) + \Delta_2^+(z,t) e^{2ikz} + \Delta_2^-(z,t) e^{-2ikz}, \quad (2.6)$$

where $E(z, t)$ and $\Delta(z, t)$ are real-valued variables ($\Delta_2^{+*} = \Delta_2^-$) and the amplitudes E_{\pm} , η_{\pm} , $\eta_{\pm\pm}$, Δ_0 and Δ_2^{\pm} vary slowly in time and space as compared to the plane wave carriers. The + and - subscripts label the two directions of propagation. The spatially dependent inversion is written as a sum of three terms, where Δ_0 is the average inversion and Δ_2 is the amplitude of the inversion grating. The two optical carrier waves propagating at frequency ω and wavenumbers $\pm k$ stand for the initial lasing mode in the cavity.

Substitution of Eqs. (2.4)-(2.6) in MB equations (2.1)-(2.3) leads to the following coupled-mode equations in the slowly varying envelope approximation (SVEA) [45]:

$$\frac{n}{c} \partial_t E_{\pm} = \mp \partial_z E_{\pm} - i \frac{N \mu \Gamma \omega}{c n_g \epsilon_0} \eta_{\pm} - \frac{1}{2} l_0 E_{\pm} , \quad (2.7)$$

$$\partial_t \eta_{\pm} = \frac{i \mu}{2 \hbar} (\Delta_0 E_{\pm} + \Delta_2^{\mp} E_{\mp}) - \frac{\eta_{\pm}}{T_2} - k^2 D \eta_{\pm} , \quad (2.8)$$

$$\partial_t \eta_{\pm\pm} = \frac{i \mu}{2 \hbar} E_{\pm} \Delta_2^{\mp} - \frac{\eta_{\pm\pm}}{T_2} - 9 D k^2 \eta_{\pm\pm} , \quad (2.9)$$

$$\partial_t \Delta_0 = \frac{\Delta_{pump} - \Delta_0}{T_1} + \frac{i \mu}{\hbar} (E_+^* \eta_+ + E_-^* \eta_- - c.c) , \quad (2.10)$$

$$\partial_t \Delta_2^{\pm} = \frac{i \mu}{\hbar} (E_{\pm}^* \eta_{\mp} - E_{\mp} \eta_{\pm}^* - E_{\pm} \eta_{\pm\pm}^* + E_{\mp}^* \eta_{\mp\mp}) - \frac{\Delta_2^{\pm}}{T_1} - 4 k^2 D \Delta_2^{\pm} . \quad (2.11)$$

where l_0 is the cavity loss coefficient that comprises intrinsic material losses and output coupling losses. In order to verify our coupled-mode expansion (2.4)-(2.6), we have performed the adiabatic-following approximation test [32] (see Appendix B) and found that the adiabatic approximation for our set of equations is in excellent agreement with the well-established Class-B laser

model. Note that this is not the case for a set of coupled-mode equations used in [39]. The second important difference is that our coupled-mode system (2.7)-(2.11) shows high-frequency instabilities at Rabi oscillation frequency while the one of Ref. [39] shows instabilities at much lower frequency (see Section 3.7).

2.4. Linear stability analysis

In this Section we carry out a linear stability analysis of our model system (2.7)-(2.11). We introduce the effective relaxation times that account for the contribution from the diffusion terms $T_g = (T_1^{-1} + 4Dk^2)^{-1}$, $T_{2_g} = (T_2^{-1} + 9Dk^2)^{-1}$ and $T_{2_eff} = (T_2^{-1} + Dk^2)^{-1}$ (these relaxation times are quoted in Table 1). We also define new variables $e_{\pm} = l_0 E_{\pm} \mu / \hbar$, $\pi_{\pm} = \eta_{\pm} l_0 / (\Delta_{th} T_{2_eff})$, $n_0 = \Delta_0 l_0 / (\Delta_{th} T_{2_eff})$, $n_{\pm} = \Delta_{\pm} l_0 / (\Delta_{th} T_{2_eff})$. The pump rate is accounted for by the parameter $p = \Delta_{pump} / \Delta_{th}$, which measures the pump rate normalized to the lasing threshold in the absence of SHB, and $N\Delta_{th} = c\hbar\epsilon_0 n_g l_0 / \Gamma\omega T_{2_eff} \mu^2$ is the carrier density at the lasing threshold.

We obtain the steady-state solution of Eqs. (2.7)-(2.11) assuming an arbitrary initial phase θ of the wave propagating in the positive z -axis direction (forward wave). Because the optical mode field $E(z, t)$ and the population parameter $\Delta(z, t)$ in Eqs. (2.4)-(2.6) are the real-valued variables, the phase of the wave propagating in the backward direction is $-\theta$, yielding the following solution for CW lasing regime [45]:

$$\begin{aligned}
e_{\pm} &= e^{\pm i\theta} l_0 \mathcal{E} \\
n_0 &= \frac{\nu_0 l_0}{T_{2_eff}}, \quad n_{\pm} = \frac{-e^{\mp i 2\theta} l_0 (\nu_0 - 1)}{T_{2_eff}} \\
\pi_{\pm} &= \frac{i}{2} e^{\pm i\theta} l_0 \mathcal{E}, \quad \pi_{\pm\pm} = -\frac{T_{2_g}}{T_{2_eff}} \frac{i}{2} (\nu_0 - 1) e^{\pm i 3\theta} l_0 \mathcal{E}
\end{aligned} \tag{2.12}$$

where

$$\mathcal{E} = \sqrt{\frac{p - \nu_0}{2T_1 T_{2_eff}}} \tag{2.13}$$

is the normalized field amplitude. Note that variables $n_-^* = n_+$, $e_-^* = e_+$, are complex conjugate while the variables $\pi_-^* = -\pi_+$, $\pi_{--}^* = -\pi_{++}$ are anti-conjugate. The SHB effect increases the effective lasing threshold and reduces the slope efficiency. To account for this effect, we introduce an additional parameter $\nu_0 = \Delta_0 / \Delta_{th}$, which is the ratio of the fundamental harmonic of the average carrier density $N\Delta_0$ to its value at the lasing threshold $N\Delta_{th}$ (at $p=1$), when SHB does not yet settle-in. We obtain the following expression for ν_0 [45]:

$$\begin{aligned}
\nu_0 &= \frac{1}{2} \left(p + 1 + \frac{T_{2_eff}}{T_{2_g}} + \frac{2T_1 T_{2_eff}}{T_g T_{2_g}} \right) \\
&\quad - \sqrt{\frac{1}{4} \left(p + 1 + \frac{T_{2_eff}}{T_{2_g}} + \frac{2T_1 T_{2_eff}}{T_g T_{2_g}} \right)^2 - p \left(1 + \frac{T_{2_eff}}{T_{2_g}} \right) - \frac{2T_1 T_{2_eff}}{T_g T_{2_g}}}
\end{aligned} \tag{2.14}$$

At lasing threshold, $\nu_0 = 1$ and it increases above the threshold (at $p > 1$). At very high pump rate ($p \gg 1$), ν_0 asymptotically approaches the value of $1 + T_{2_eff} / T_{2_g}$.

The linear stability analysis of the steady-state solution (2.12)-(2.14) is performed by introducing small perturbations $\delta e_{\pm} = \delta e_r + i\delta e_i$, $\delta \pi_{\pm} = \delta \pi_r + i\delta \pi_i$, $\delta \pi_{\pm\pm} = -(\delta \pi_{rr} + i\delta \pi_{ii})$, δn_0 and $\delta n_{\pm} = \delta n_r + i\delta n_i$ in the corresponding variables of

the coupled-mode equations (2.7)-(2.11). Taking into account the complex conjugate and anti-conjugate relationships between the variables $\delta n_- = \delta n_+^*$, $\delta e_- = \delta e_+^*$, $\delta \pi_- = -\delta \pi_+^*$, $\delta \pi_{--} = -\delta \pi_{++}^*$, we obtain the following linearized system of differential equations:

$$\begin{aligned} \partial_t(\delta \pi_r) + \frac{1}{T_{2_eff}}(\delta \pi_r) = & \left(-\frac{E \sin(\theta)}{2} \right) \delta n_0 + \frac{E \delta n_i \cos(\theta)}{2} + \frac{E \delta n_r \sin(\theta)}{2} \\ & - \frac{l_0 \delta e_i [\nu_0 + \cos(2\theta)(\nu_0 - 1)]}{2T_{2_eff}} + \frac{l_0 \delta e_r \sin(2\theta)(\nu_0 - 1)}{2T_{2_eff}} \end{aligned} \quad (2.15)$$

$$\begin{aligned} \partial_t(\delta \pi_i) + \frac{1}{T_{2_eff}}(\delta \pi_i) = & \left(-\frac{E \sin(\theta)}{2} \right) \delta n_i + \frac{E \delta n_0 \cos(\theta)}{2} + \frac{E \delta n_r \cos(\theta)}{2} \\ & + \frac{l_0 \delta e_r [\nu_0 - \cos(2\theta)(\nu_0 - 1)]}{2T_{2_eff}} - \frac{l_0 \delta e_i \sin(2\theta)(\nu_0 - 1)}{2T_{2_eff}} \end{aligned} \quad (2.16)$$

$$\begin{aligned} \partial_t(\delta \pi_{rr}) + \frac{1}{T_{2_g}}(\delta \pi_{rr}) = & \left(-\frac{E \cos(\theta)}{2} \right) \delta n_i + \frac{E \delta n_r \sin(\theta)}{2} \\ & - \frac{l_0 \delta e_i \cos(2\theta)(\nu_0 - 1)}{2T_{2_eff}} - \frac{l_0 \delta e_r \sin(2\theta)(\nu_0 - 1)}{2T_{2_eff}} \end{aligned} \quad (2.17)$$

$$\begin{aligned} \partial_t(\delta \pi_{ii}) + \frac{1}{T_{2_g}}(\delta \pi_{ii}) = & \left(-\frac{E \cos(\theta)}{2} \right) \delta n_r + \frac{l_0 \delta e_r \cos(2\theta)(\nu_0 - 1)}{2T_{2_eff}} \\ & - \frac{E \delta n_i \sin(\theta)}{2} - \frac{l_0 \delta e_i \sin(2\theta)(\nu_0 - 1)}{2T_{2_eff}} \end{aligned} \quad (2.18)$$

$$\partial_t(\delta n_0) = 4E\delta \pi_r \sin(\theta) - 4E\delta \pi_i \cos(\theta) - 2El_0\delta e_r \cos(\theta) - 2El_0\delta e_i \sin(\theta) - \frac{\delta n_0}{T_1} \quad (2.19)$$

$$\begin{aligned} \partial_t(\delta n_r) = & \delta e_i El_0 [\sin(\theta) + (\nu_0 - 1) \sin(3\theta)] + 2E\delta \pi_{ii} \cos(\theta) - 2E\delta \pi_i \cos(\theta) \\ & - 2E\delta \pi_r \sin(\theta) - 2E\delta \pi_{rr} \sin(\theta) - El_0 \delta e_r \left[\cos(\theta) - \cos(3\theta) \frac{T_{2_g}}{T_{2_eff}} (\nu_0 - 1) \right] - \frac{\delta n_r}{T_g} \end{aligned} \quad (2.20)$$

$$\begin{aligned}
\partial_t(\delta n_i) = & \delta e_r E l_0 [\sin(\theta) - (v_0 - 1) \sin(3\theta)] + 2E \delta \pi_{rr} \cos(\theta) - 2E \delta \pi_r \cos(\theta) \\
& + 2E \delta \pi_i \sin(\theta) + 2E \delta \pi_{ii} \sin(\theta) + E l_0 \delta e_i \left[\cos(\theta) + \cos(3\theta) \frac{T_{2-g}}{T_{2-eff}} (v_0 - 1) \right] - \frac{\delta n_i}{T_g}
\end{aligned} \tag{2.21}$$

$$\partial_z(\delta e_r) + \frac{n}{c} \partial_t(\delta e_r) = \delta \pi_i - \frac{1}{2} l_0 \delta e_r \tag{2.22}$$

$$\partial_z(\delta e_i) + \frac{n}{c} \partial_t(\delta e_i) = -\delta \pi_r - \frac{1}{2} l_0 \delta e_i \tag{2.23}$$

which can be recast in the following matrix form:

$$\partial_t \begin{bmatrix} \delta \pi_r \\ \delta e_r \\ \delta n_0 \\ \delta n_r \\ \delta \pi_{ii} \\ \delta e_i \\ \delta n_i \\ \delta \pi_{rr} \end{bmatrix} = \begin{bmatrix} -\frac{1}{T_{2-eff}} & \frac{v_0 - (v_0 - 1) \cos 2\theta}{2T_{2-eff}} & \frac{\mathcal{E} \cos \theta}{2} & \frac{\mathcal{E} \cos \theta}{2} & 0 & 0 & -\frac{(v_0 - 1) \sin 2\theta}{2T_{2-eff}} & -\frac{\mathcal{E} \sin \theta}{2} & 0 \\ \frac{1}{\tau} & -\frac{1}{2\tau} - i\Omega & 0 & 0 & 0 & 0 & 0 & 0 & 0 \\ -4\mathcal{E} \cos \theta & -2\mathcal{E} \cos \theta & -\frac{1}{T_i} & 0 & 0 & 4\mathcal{E} \sin \theta & -2\mathcal{E} \sin \theta & 0 & 0 \\ -2\mathcal{E} \cos \theta & \left[(v_0 - 1) \frac{T_{2-g}}{T_{2-eff}} \cos 3\theta - \cos \theta \right] \mathcal{E} & 0 & -\frac{1}{T_g} & 2\mathcal{E} \cos \theta & -2\mathcal{E} \sin \theta & \left[(v_0 - 1) \frac{T_{2-g}}{T_{2-eff}} \sin 3\theta + \sin \theta \right] \mathcal{E} & 0 & -2\mathcal{E} \sin \theta \\ 0 & \frac{(v_0 - 1) \cos 2\theta}{2T_{2-eff}} & 0 & -\frac{\mathcal{E} \cos \theta}{2} & -\frac{1}{T_{2-g}} & 0 & \frac{(v_0 - 1) \sin 2\theta}{2T_{2-eff}} & -\frac{\mathcal{E} \sin \theta}{2} & 0 \\ 0 & \frac{(v_0 - 1) \sin 2\theta}{2T_{2-eff}} & -\frac{\mathcal{E} \sin \theta}{2} & \frac{\mathcal{E} \sin \theta}{2} & 0 & -\frac{1}{T_{2-eff}} & -\frac{v_0 + (v_0 - 1) \cos 2\theta}{2T_{2-eff}} & \frac{\mathcal{E} \cos \theta}{2} & 0 \\ 0 & 0 & 0 & 0 & 0 & -\frac{1}{\tau} & -\frac{1}{2\tau} - i\Omega & 0 & 0 \\ 2\mathcal{E} \sin \theta & \left[-(v_0 - 1) \frac{T_{2-g}}{T_{2-eff}} \sin 3\theta + \sin \theta \right] \mathcal{E} & 0 & 0 & 2\mathcal{E} \sin \theta & -2\mathcal{E} \cos \theta & \left[(v_0 - 1) \frac{T_{2-g}}{T_{2-eff}} \cos 3\theta + \cos \theta \right] \mathcal{E} & \frac{1}{T_g} & 2\mathcal{E} \cos \theta \\ 0 & -\frac{(v_0 - 1) \sin 2\theta}{2T_{2-eff}} & 0 & \frac{\mathcal{E} \sin \theta}{2} & 0 & 0 & -\frac{(v_0 - 1) \cos 2\theta}{2T_{2-eff}} & -\frac{\mathcal{E} \cos \theta}{2} & -\frac{1}{T_{2-g}} \end{bmatrix} \begin{bmatrix} \delta \pi_r \\ \delta e_r \\ \delta n_0 \\ \delta n_r \\ \delta \pi_{ii} \\ \delta e_i \\ \delta n_i \\ \delta \pi_{rr} \end{bmatrix} \tag{2.24}$$

where $\tau = n_g / c l_0$ is the photon lifetime in the cavity.

Using the ansatz from Ref. [31], we recast all perturbations δX to the main lasing mode in the form of propagating wavelets $\delta X \propto \exp(in_g \Omega z / c + \Lambda t)$, where Λ can be interpreted as the Lyapunov exponent, $\Omega n_g / c$ is the detuning of the propagation constant from the one of the lasing mode and $-\text{Im}(\Lambda)$ is the frequency offset. Note that among all possible solutions $\Lambda(\Omega)$ of the dispersion equation that follows from Eq. (2.24), only the solutions with positive increment $\text{Re}(\Lambda) > 0$ will build-up in the cavity after several round-

trips, which fulfills the cavity round-trip phase self-repetition condition $2\Omega L n_g / c = 2\pi n$, where L is the cavity length and n is an integer number. Nevertheless, it is convenient to carry out our stability analysis considering Ω as a continuous parameter. It can be regarded as the offset frequency from the lasing mode because for all practical situations of interest in this study, the approximation $\text{Im}(\Lambda) \approx -\Omega$ suffices.

Numerical solution of Eq. (2.24) reveals that only one Lyapunov exponent of the 9×9 linear stability matrix may have positive real part and thus may lead to a multimode instability in the practical range of pump rates considered here (see Fig. 2.1 below and related discussion).

Via a transformation of variables, the 9×9 matrix in Eq. (2.24) can always be altered into a block-diagonal form with 5×5 and 4×4 blocks, as depicted in Eq. (2.25) below [45], [58]. Out of these two matrices, only the smaller-size matrix may exhibit Lyapunov exponent with the positive real part in the practically feasible range of pump currents (see discussion to Fig. 2.1 below). The required transformation, and hence the set of variables responsible for instability, are both changing with the initial phase of the mode θ . However, the instability increment $\text{Re}(\Lambda)$ remains fixed, attesting that the initial phase has no impact on the occurrence of instability. For simplicity, in what follows we assume that the laser initially operates in a CW lasing regime and the phase of the mode is $\theta=0$. Such transformation is straightforward, yielding the following eigenproblem [45]:

$$\begin{bmatrix}
-\frac{1}{T_{2_eff}} - \Lambda & \frac{1}{2T_{2_eff}} & \frac{\mathcal{E}}{2} & \frac{\mathcal{E}}{2} & 0 & 0 & 0 & 0 & 0 \\
\frac{1}{\tau} & -\frac{1}{2\tau} - i\Omega - \Lambda & 0 & 0 & 0 & 0 & 0 & 0 & 0 \\
-4\mathcal{E} & -2\mathcal{E} & -\frac{1}{T_1} - \Lambda & 0 & 0 & 0 & 0 & 0 & 0 \\
-2\mathcal{E} & \left[(\nu_0 - 1) \frac{T_{2_g}}{T_{2_eff}} - 1 \right] \mathcal{E} & 0 & -\frac{1}{T_g} - \Lambda & 2\mathcal{E} & 0 & 0 & 0 & 0 \\
0 & \frac{(\nu_0 - 1)}{2T_{2_eff}} & 0 & -\frac{\mathcal{E}}{2} & -\frac{1}{T_{2_g}} - \Lambda & 0 & 0 & 0 & 0 \\
0 & 0 & 0 & 0 & 0 & -\frac{1}{T_{2_eff}} - \Lambda & -\frac{(2\nu_0 - 1)}{2T_{2_eff}} & \frac{\mathcal{E}}{2} & 0 \\
0 & 0 & 0 & 0 & 0 & -\frac{1}{\tau} & -\frac{1}{2\tau} - i\Omega - \Lambda & 0 & 0 \\
0 & 0 & 0 & 0 & 0 & -2\mathcal{E} & \left[(\nu_0 - 1) \frac{T_{2_g}}{T_{2_eff}} + 1 \right] \mathcal{E} & -\frac{1}{T_g} - \Lambda & 2\mathcal{E} \\
0 & 0 & 0 & 0 & 0 & 0 & -\frac{(\nu_0 - 1)}{2T_{2_eff}} & -\frac{\mathcal{E}}{2} & -\frac{1}{T_{2_g}} - \Lambda
\end{bmatrix}
\begin{bmatrix}
\delta\pi_i \\
\delta e_r \\
\delta n_0 \\
\delta n_r \\
\delta\pi_{ii} \\
\delta\pi_r \\
\delta e_i \\
\delta n_i \\
\delta\pi_{rr}
\end{bmatrix} = 0
\tag{2.25}$$

which can also be presented in the following form:

$$\det \begin{bmatrix}
-\frac{1}{T_{2_eff}} - \Lambda & \frac{1}{2T_{2_eff}} & \frac{\mathcal{E}}{2} & \frac{\mathcal{E}}{2} & 0 \\
\frac{1}{\tau} & -\frac{1}{2\tau} - i\Omega - \Lambda & 0 & 0 & 0 \\
-4\mathcal{E} & -2\mathcal{E} & -\frac{1}{T_1} - \Lambda & 0 & 0 \\
-2\mathcal{E} & \left[(\nu_0 - 1) \frac{T_{2_g}}{T_{2_eff}} - 1 \right] \mathcal{E} & 0 & -\frac{1}{T_g} - \Lambda & 2\mathcal{E} \\
0 & \frac{(\nu_0 - 1)}{2T_{2_eff}} & 0 & -\frac{\mathcal{E}}{2} & -\frac{1}{T_{2_g}} - \Lambda
\end{bmatrix} = 0,$$

$$\det \begin{bmatrix}
-\frac{1}{T_{2_eff}} - \Lambda & -\frac{(2\nu_0 - 1)}{2T_{2_eff}} & \frac{\mathcal{E}}{2} & 0 \\
-\frac{1}{\tau} & -\frac{1}{2\tau} - i\Omega - \Lambda & 0 & 0 \\
-2\mathcal{E} & \left[(\nu_0 - 1) \frac{T_{2_g}}{T_{2_eff}} + 1 \right] \mathcal{E} & -\frac{1}{T_g} - \Lambda & 2\mathcal{E} \\
0 & -\frac{(\nu_0 - 1)}{2T_{2_eff}} & -\frac{\mathcal{E}}{2} & -\frac{1}{T_{2_g}} - \Lambda
\end{bmatrix} = 0
\tag{2.26}$$

We find that only one eigenvalue of the lower 4×4 block may have $\text{Re}(\Lambda) > 0$ and may lead to unstable CW lasing regime observed in experiment. The

upper 5×5 block shows only stable solutions in a large range of pump rates above the lasing threshold. Thus for a QCL from Table 1, this behavior is observed up to $p \sim 60$ times above the lasing threshold (Fig. 2.1). For AlGaAs QW LD from Table 1, it is continuous up to $p \sim 1100$. In what follows the discussion will be limited to this sufficiently large range of pump rates when only one eigenvalue in Eq. (2.25) may lead to a multimode instability.

The instability in Eq. (2.25) is related to variables $\delta\pi_r$, δe_i , δn_i and $\delta\pi_{rr}$. When the initial phase of the mode θ is detuned from $\theta=0$, the variables associated with the lower 4×4 block are altered. For example, for $\theta = \pi/2$, the instability is due to perturbations $\delta\pi_i$, δe_r , δn_r and $\delta\pi_{ii}$. Therefore, it is not possible to identify the nature of instability (RNGH-like or of a different kind) from the set of variables involved. At the same time we find that whatever the initial phase θ , the offset frequency Ω_{\max} at the maximum increment $\text{Re}(\Lambda)$ is close to the Rabi oscillation frequency $\Omega_{Rabi} = \sqrt{(p - \nu_0) / T_1 T_{2_eff}}$ (see Section 3.3 below). This allows us to attribute this instability to the RNGH-like behavior discussed in Refs. [30], [31].

This behavior should be contrasted with the one reported in [39], where (i) the carrier coherence grating given by Eq. (2.9) has not been taken into account and (ii) truncated coupled mode equations for carrier population grating and medium polarization contained errors (see our discussion to Eqs. (2.7)-(2.11), Appendix B and analytical solution [46] obtained in Section 4.1). If one omits the variables $\delta\pi_{rr}$ and $\delta\pi_{ii}$ associated with the carrier coherence grating, the lower 4×4 matrix block in Eq. (2.26) simply becomes of 3×3 size [45]. It still exhibits an instability at small pump rate above the lasing threshold. According to [39] the instability occurs at significantly lower frequencies around $\Omega_{SHB} = \sqrt{T_1^{-1} \sqrt{(p-1) / 3T_1 T_2}} \sim \sqrt{\Omega_{Rabi} / T_1} / \sqrt[4]{3}$. Therefore, this instability has been attributed in [39] to the SHB effect. It will be shown below that this

instability occurs, in fact, at a much higher frequency close to Ω_{Rabi} . These outcomes of our numerical studies [45] agree very well with our analytic solution reported in [46] (see Section 4.1).

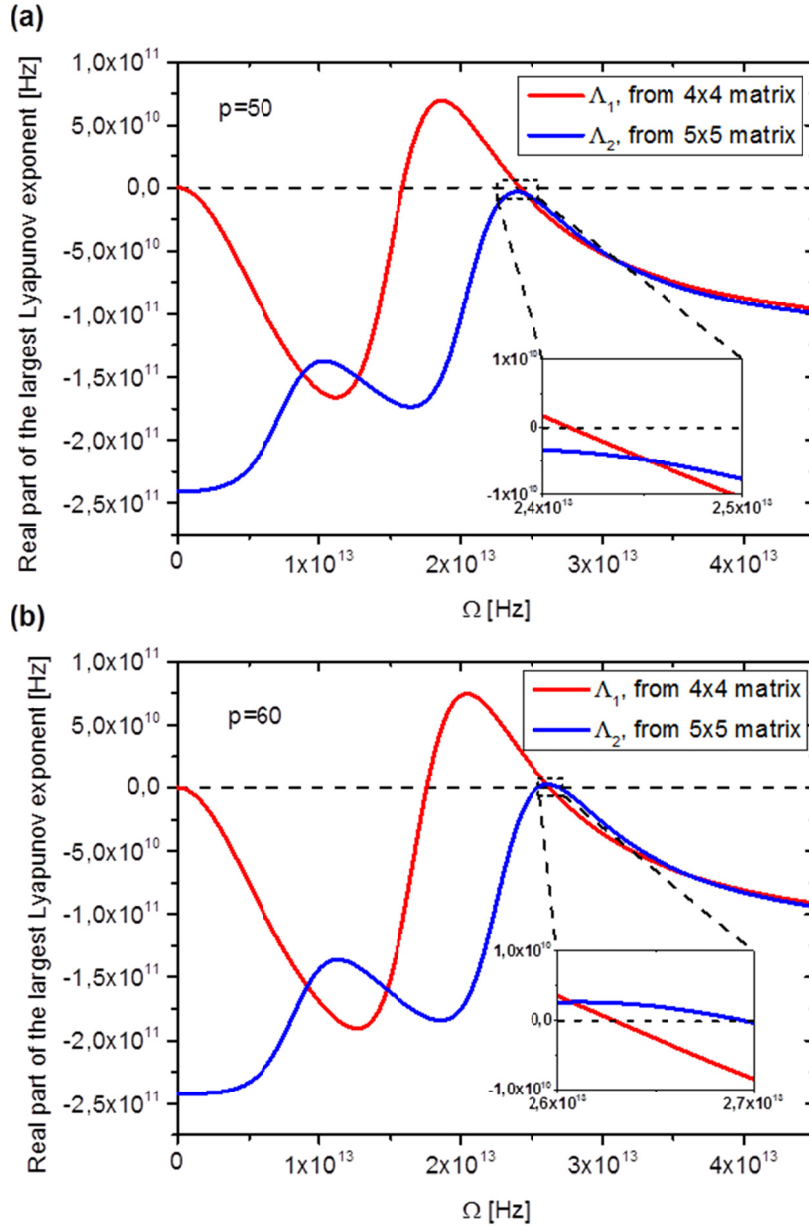


Fig. 2.1. Spectra of instability increments (largest real parts of the Lyapunov exponents) of the 4x4 (red curves) and 5x5 matrix (blue curves) blocks at $p=50$ (panel (a)) and $p=60$ (panel (b)) for QCL with parameters from Table 1.

The upper 5×5 matrix block in (2.26), which shows only stable solutions in the presence of the carrier coherence grating (2.9) and in the reasonable range of pump rates, takes the form of a 4×4 matrix after dropping out the variables $\delta\pi_{rr}$ and $\delta\pi_{ii}$. Our analysis shows that it may lead to RNGH instability at the pump rate approximately 10 times above the lasing threshold, in agreement with the theoretical predictions from [30], [31]. The second threshold always remains that high unless a saturable absorber is introduced to the model system [40], the possibility which was studied in [39].

We thus argue that inclusion of both grating terms (2.9) and (2.11) allows one to obtain low-threshold RNGH instability in a *FP cavity laser* (or *bidirectional ring laser*) without saturable absorber. This instability is of different origin from the one discussed in Ref. [39]. In our case it originates from the lower 4×4 matrix block in Eq. (2.26) and not from the upper 5×5 block. The coherence grating (2.9) renders the second threshold associated with the 5×5 block prohibitively higher (at $p \sim 60$ instead of the initial value of $p \sim 9-10$ in the original RNGH instability case for a *unidirectional ring laser* without SHB effect), see Fig. 2.1. Note that it is impossible to make similar parallels with the treatment from [41] because it utilizes the laser rate equation model in the lumped gain picture. In the following sections these points will be elucidated in further detail.

3. RNGH self-pulsations in monolithic QCL chip

3.1. RNGH instability threshold

For QCLs that have the (standard) cavity length of 2-4 mm, our linear stability analysis (Section 2.4) predicts the multimode RNGH instability at a pump rate of a few percent above the lasing threshold. This prediction is in agreement with numerous experimental data available in the literature [29], [39], [48]. The numerical simulations based on TW rate equation model [45], [47] also confirm this behavior and the transition to multimode operation at just above the lasing threshold (see Section 3.3).

In the case of a short-cavity single-section QCL of just 100 μm long, our numerical simulations (see Section 3.4) reveal stable CW operation regime up to the pump rate of 2-2.5 times above the lasing threshold [45], [46], [58]. The RNGH-like self-pulsations occur above the second threshold of $p_{th2} \sim 2.5$ (see below). However, the linear stability analysis based on Eq. (2.26), 4x4 determinant, shows that the real part of the Lyapunov exponent $\text{Re}(\Lambda)$ becomes positive at the pump rate p just slightly above 1 (lasing threshold, first threshold). Moreover, with increasing p , the instability increment $\text{Re}(\Lambda)$ increases monotonically, without revealing any specific behavior at p_{th2} . Therefore it is necessary to examine the spectral behavior of the increment

$\text{Re}(\Lambda)$ and we arrive to a new insight into the second threshold condition, which is presented below.

Fig. 3.1 illustrates the spectral behavior of the increment $\text{Re}(\Lambda)$ in a QCL with the cavity length of 100 μm . Only positive offset frequencies are shown, because the spectral shape of $\text{Re}(\Lambda)$ is an even function of Ω . The instability increment is plotted normalized to the cavity mode separation, which yields us the spectrum of the round-trip gain coefficient $2\text{Re}(\Lambda)n_gL/c$ for various cavity modes. In the figure, the instability gain spectra are depicted at three different pump rates of $p=1.1$, 1.2 and 3 (green, red and blue curves, respectively). The locations of a few cavity modes are indicated by plotting the Airy function of the “cold cavity” (black curve, not in scale). The zero offset frequency corresponds to the initially lasing mode.

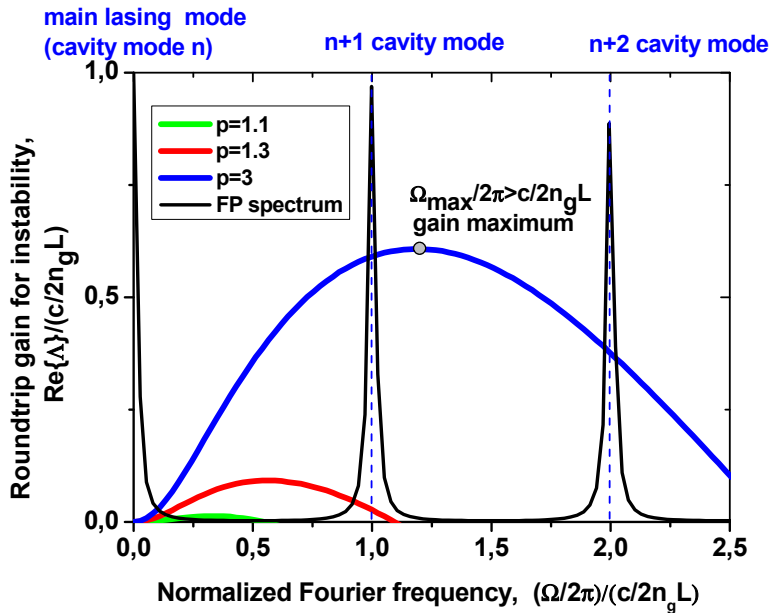


Fig. 3.1. Positive offset frequency part of the spectrum of the round-trip gain for instability in a 100 μm long QCL at normalized pump rate of $p=1.1$ (green curve), $p=1.3$ (red curve) and $p=3$. The black curve indicates the Airy function of the cold cavity (not in scale). Other QCL parameters are given in Table 1. © 2017 IEEE. Reprinted, with permission, from [45].

The RNGH condition [30], [31] for multimode instability in a CW operating single-mode laser requires that the instability increment is positive at a frequency of another cavity mode. An example that matches this definition is the instability gain curve plotted in Fig. 3.1 for $p=1.3$ (red curve). It shows a positive gain for the first two adjacent cavity modes at the offset frequencies $\Omega/2\pi = \pm c/2n_g L$. In Fig. 3.2, this gain coefficient is plotted as a function of the pump rate (dashed blue curve). According to the conventional definition of the second threshold, the multimode RNGH instability should occur at $p=1.25$, when the gain for instability becomes positive at some of the non-lasing cavity modes (blue dashed curve in Fig. 3.2).

Although the positive increment for instability of single mode CW lasing regime in Eq. (2.26) indicates the instability of the lasing mode, it does not imply that RNGH self-pulsations will occur (not every small-amplitude instability necessarily develops into large-amplitude RNGH self-pulsations) [45], [46]. The laser may just switch to another mode, which is also unstable. The increment for instability of the mode is small [e.g. see the red curve in Fig. 3.1 obtained at $p=1.3$] so the switching process will be slow and may be driven by technical noise. A classic example is a ring laser with reciprocal cavity for counter-propagating modes and absence of mode coupling via backscattering in the cavity: it shows sporadic switching of the lasing direction (spontaneous mode-jumps) at times much longer than the characteristic times T_1 , T_2 and τ [64]. A FP cavity laser may also exhibit such spontaneous mode-jumps [67] and the linear stability analysis in Eq. (2.26) does not exclude such possibility. Other possibility is related to multimode phase instability in semiconductor laser which admits adiabatic approximation for the medium polarization [68], [67]. Note that since RNGH instability is the multimode amplitude instability [69], our numeric model utilizes slowly varying envelope approximation for the field amplitude [47] and therefore it cannot reproduce spontaneous mode-jumps or slow phase instabilities. The main difference between RNGH

instability and all other instabilities is that, when the regime of RNGH self-pulsations sets in, the medium polarization does not follow adiabatically the optical field in the cavity. However, at the initial stage when the CW single-mode lasing regime just becomes unstable, there is only a small-amplitude perturbation of the optical field circulating in the cavity. In the most general case it has the form of an optical pulse. The interaction of the active medium with such a small-amplitude perturbation is still governed by adiabatic approximation [32] and does not necessarily give rise to a non-adiabatic behavior at a later stage [45].

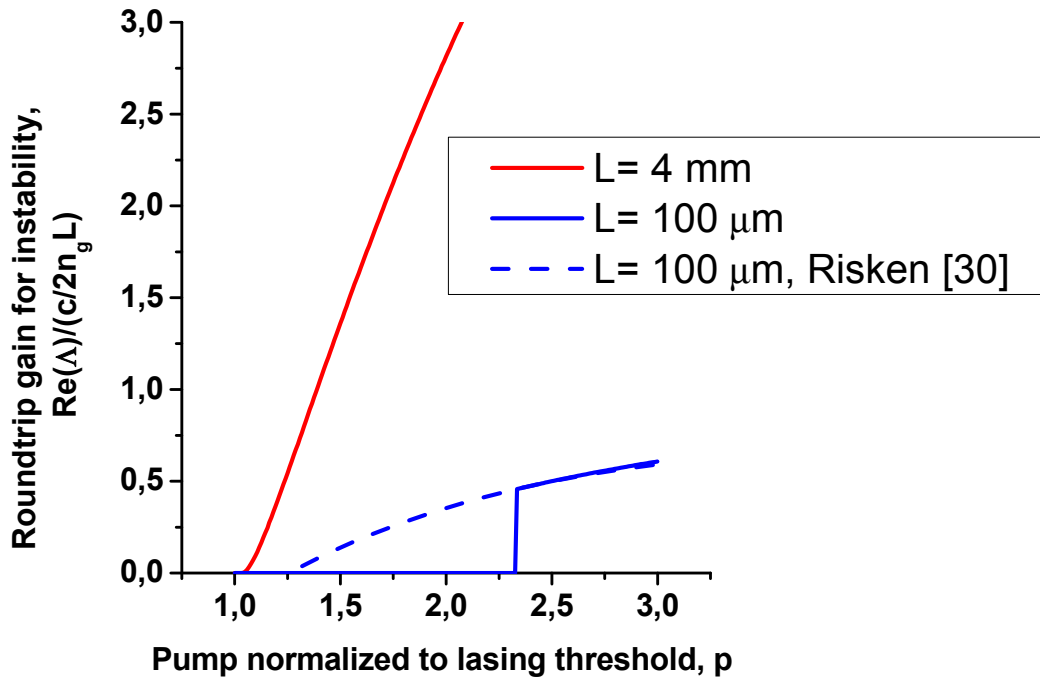


Fig. 3.2. Lyapunov stability analysis: round-trip gain for RNGH instability vs. pump excess above threshold for the QCLs with the cavity lengths of 4 mm (red curve) and 100 μm (solid blue curve). For explanations on the dashed blue curve, see discussion in the text. In long-cavity QCL, the second threshold is very low, at $p_{\text{th}2}=1.05$, while $p_{\text{th}2}=2.35$ in the short-cavity QCL. Other QCL parameters are given in Table 1.

In order to verify the RNGH threshold condition, we perform a series of numerical simulations based on the travelling wave rate equation model [45]. Our model is adapted from [47] by removing saturable absorber section. It utilizes slowly varying envelope approximation for the field amplitude, which is a real valued variable in the model. It cannot reproduce mode jumps, while the amplitude instabilities can be detected by examining the simulated waveforms. As a model system we use a short-cavity single-section sample ($L=100 \mu\text{m}$). The travelling wave model incorporates Langevin force terms that seed the spontaneous polarization noise into the system (these terms are not indicated in Eqs. (2.1)-(2.3), but an example can be found in [47]). We examine several different power levels of the noise injected into the system. Fig. 3.3 shows that the output power of amplified spontaneous emission P_{sp} varies over 6 orders of magnitude, from eight to two orders below the polarization noise level in homogeneously broadened ensemble of two-level quantum oscillators [45], [46], [70].

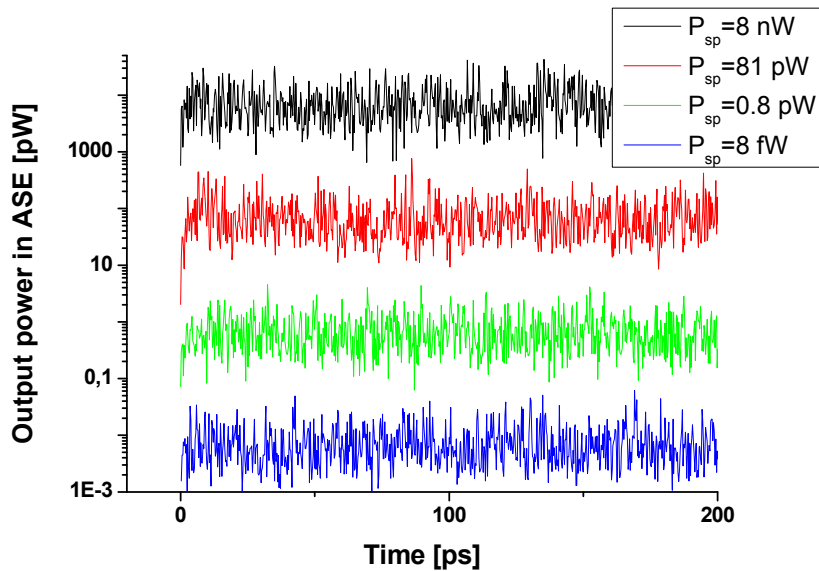


Fig. 3.3. Output power variation in amplified spontaneous emission (ASE) regime below the lasing threshold ($p=0.9$) for different levels of spontaneous polarization noise used in the numerical simulations. QCL cavity length is $100 \mu\text{m}$. Other parameters are given in Table 1.

In Fig. 3.4, for each set of parameters (p, P_{sp}) we perform a series of 20 simulations and calculate the probability of occurrence of the RNGH like self-pulsations (example of the waveforms can be found in Fig. 3.11 below). These statistical data are displayed in Fig. 3.4 as vertical bars with the color corresponding to the spontaneous polarization noise power in Fig. 3.3. It follows that there are no systematic correlations between the occurrence of RNGH instability and spontaneous noise power P_{sp} injected into the system. We have not seen the impact of the noise power on the lasing regime, only the delay time to the onset of emission was changing. The noise power that we will use in all the simulations throughout the rest of the manuscript is $P_{\text{sp}}=81$ pW (red trace in Fig. 3.3 and Fig. 3.4). In Fig. 3.4 we also plot the average probability over all 80 realizations at different P_{sp} (solid curve). It has the dispersion of ± 0.056 , which is indicated in Fig. 3.4 by the error bars.

The data in Fig. 3.4 attest that there is no multimode RNGH instability at the pump rate $p=1.5$. This is in contradiction with the conventional definition of the second threshold, foreseeing $p_{\text{th}2}=1.25$ (Fig. 3.2, dashed blue curve). At $p=2$, only a few realizations have resulted in RNGH self-pulsations [45]. The average probability of these is of 0.04, which is below the uncertainty limit. The RNGH instability develops at p between 2 and 2.5, with $p=2.5$ being the first point in Fig. 3.4 for which the probability exceeds the uncertainty range.

Clearly the results of our numerical simulations are not in agreement with the second threshold condition as originally proposed by Risken and Nummedal [30], and Graham and Haken [31]. Analyzing the data in Fig. 3.4, we find that RNGH instability occurs when the instability gain maxima located at the offset frequencies $\Omega_{\text{max}} \approx \pm \Omega_{\text{Rabi}}$ are either on resonance with the nearest-neighbor cavity modes at $\pm c\pi/n_g L$ or at a higher frequency offset as in the case indicated by the blue curve in Fig. 3.1.

The RNGH instability gain coefficient corresponding to this refinement of the second threshold is plotted in Fig. 3.2 as a function of the pump rate (solid blue curve). It reveals an abrupt switching-on behavior for the RNGH instability, the feature which is not seen in long-cavity QCLs because of the small frequency separation between the cavity modes (Fig. 3.2 red curve). The numerical results in Fig 5 are in reasonable agreement with the second threshold value of $p_{th2}=2.35$ in Fig. 3.2 (solid blue curve) obtained using our modified second threshold condition [45], [46].

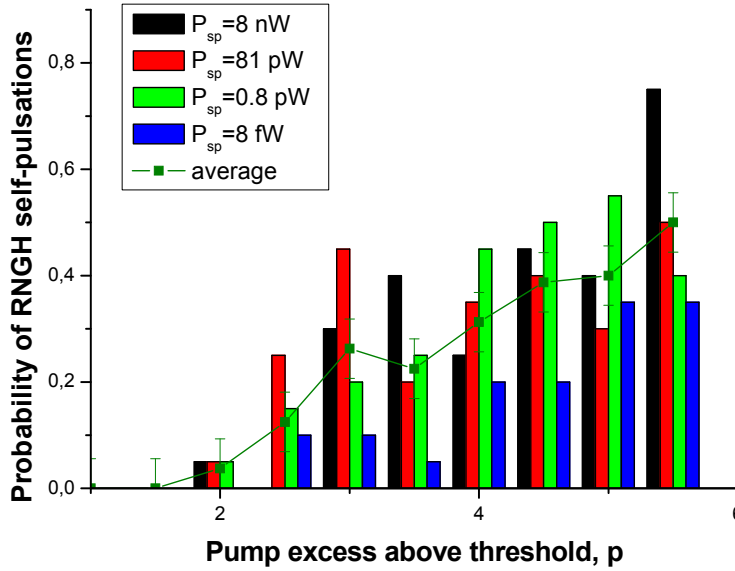


Fig. 3.4. Probability of occurrence for RNGH self-pulsations is plotted as a function of the pump excess above lasing threshold p for different levels of spontaneous polarization noise shown in Fig. 3.3 (bars) as well as for the average over all realizations (green curve). QCL cavity length is $100 \mu\text{m}$. Other parameters are given in Table 1. See further details in the text.

The proposed refinement for the second threshold has a clear physical meaning. Recall that RNGH instability in a CW single-mode laser arises due to Rabi splitting of the lasing transition induced by the lasing mode. As a result of such spectral broadening and reshaping of the gain curve, the laser can

provide sufficient optical gain to other longitudinal modes at the early stage of instability [71]. Most importantly, this shall lead to large-amplitude self-pulsations at a later stage such that the medium polarization does not simply follow adiabatically the optical field but instead it becomes a leading variable of this dynamical system [31]. Therefore we assume that the initial perturbation to the lasing mode has a pulse shape and we apply the pulse area theorem for non-adiabatic pulse propagation [32], [72]. In the most general case, the characteristic time of such perturbation pulse is roughly a half of the cavity round-trip time $\tau_p \sim Ln_g / c$. From the pulse area theorem, we have noticed that a perturbation in the form of an optical pulse is unstable and the pulse area grows so as the fast (non-adiabatic) medium polarization dynamics becomes possible if, initially, $\Omega_{Rabi} \cdot \tau_p > \pi$. Because the maximum gain for RNGH instability is located at the offset frequency $\Omega_{max} \approx \pm \Omega_{Rabi}$, we conclude that the multimode RNGH instability occurs only when [45]:

$$|\Omega_{max}| / 2\pi \geq c / 2Ln_g \quad (3.1)$$

The blue curve in Fig. 3.1 satisfies this condition while the red one does not. This condition has minor impact on QCLs with long cavities. However, it raises the second threshold considerably in short-cavity devices because of the large frequency separation between the cavity modes. In Ref. [46] and in Section 3.1 we have obtained an analytic expression for the pump rate at RNGH self-pulsations threshold (3.1).

3.2. Experimental observations of RNGH instability in QCLs

In Section 3.1 we have refined the necessary conditions for occurrence of multimode RNGH instability. The numerical simulations reveal regimes with either regular or chaotic self-pulsations (Sections 3.3 and 3.4 below). Therefore,

it is useful to clarify at this point which features provide an evidence for RNGH instability.

The experimental data available in the literature attest that RNGH instability does not always lead to observation of a clear Rabi splitting in the optical mode spectrum of a QCL. In some experimental realizations, RNGH instability causes just a broadening of the lasing spectrum to the offset frequencies of the order of the Rabi oscillation frequency. Indeed, the appearance of Rabi splitting in the optical spectrum can be tailored by changing the sample temperature [29], [39], [48]. For example, in [39] at low temperatures (80-150 K) the measured lasing spectra in a buried heterostructure QCL sample are just simply broadened, but with increasing temperature, the Rabi splitting between mode clusters becomes more apparent. At room temperature conditions, two distinct mode clusters emerge in the optical spectrum. Because temperature dependence of carrier diffusion has been found to produce a too weak contrast change in the SHB grating [39], the thermal population of injector levels yielding temperature-dependent saturable absorption has been suggested as one of the possible mechanisms. However, in [48], QCL samples show totally opposite spectral behavior with the temperature. The optical spectra reveal lasing mode clusters with separation of $\sim 20\text{-}30\text{ cm}^{-1}$ at liquid He temperature (6 K) while at an increased temperature of 77 K, no clear spectral splitting is observed in the broad multimode emission spectrum. Although available experimental reports do not elucidate the nature of the temperature effect, most importantly they allows us to spot one common feature: once a laser sample exhibits clear Rabi splitting at some temperature, it also reveals very broad multimode emission at other temperatures, which can be with or without mode clustering [45]. The overall spectral width of such multimode emission practically does not change with the temperature, reaching $\sim 35\text{-}40\text{ cm}^{-1}$ at the pump rate of $p\sim 1.7\text{-}1.8$ times above lasing threshold and the width of $\sim 60\text{ cm}^{-1}$ for $p\sim 3.5\text{-}3.6$. Therefore we

conclude that the multimode dynamics responsible for such large spectral broadening at different temperatures is governed by the same processes. Hence an observation of large spectral broadening on the order of Ω_{Rabi} already provides an indication of multimode RNGH instability, whilst the optical spectrum might not be split in two distinct mode clusters. This conclusion is in agreement with experimentally measured QCL spectra in [41].

Even if the two distinct mode clusters appear in the lasing spectrum, their frequency splitting is not necessarily equal to $2\Omega_{Rabi}$. The pump rate dependence of the Rabi frequency [see Eq. (3.2) below] assumes that this splitting is proportional to the square root of the output power. In [29], [39] this behavior is confirmed for the range of QCL output power up to 36 mW and the frequency splitting up to 1 THz is observed in 3 μm -wide buried heterostructure lasers. However, for 10-15 μm wide ridge waveguide lasers from [39] and [48], the spectral splitting is clamped at about 0.8 THz for the output power of ~ 25 mW and higher. This is not surprising because the notion of the Rabi splitting in the gain spectrum of a laser is introduced considering small-amplitude perturbations to the initial optical field in the cavity [45]. This small-signal picture is very different from the situation in the laser undergoing large-amplitude self-pulsations. At high pump rates, the overall spectral broadening due to multimode RNGH instability can be smaller than $2\Omega_{Rabi}$.

In the cited works, the complex structure of the lasing transition in QCL is usually not taken into account in the interpretation of experimental results. At the same time inhomogeneous features in the optical gain curve or dispersive characteristics of the cavity (e.g due to backscattering from microcracks [73]) may significantly reshape the spectral envelop of multimode RNGH emission [45].

All experimental studies cited here are limited to long-cavity QCL samples of 1.5-4 mm length. The data reported in [48] might lead to a conjecture that sample length has an impact on the appearance of the two distinct mode clusters. Unfortunately no detailed experimental study on the effect of the sample length on RNGH instability has been reported.

In [74] authors report on experimental observation of excitation and suppression of low-threshold RNGH instability in mid-infrared InGaAs/InAlAs QCLs with level alignment and resonant tunneling between injector and active quantum wells (QWs). They have identified two different mechanisms that can be used for tailoring RNGH instability with applied bias field and/or optical excitation of free carriers. The first mechanism is due to switching between a diagonal transition from injector to active region and a vertical transition within active QWs during a transient turning-on process. The second mechanism is based on unstable electric field domain (EFD) formation [75], [76] when the applied bias field is greater than that at the tunneling resonance. Note that their experimental results are in agreement with the analysis developed in this dissertation and [45], [46] that attribute the low-threshold RNGH instability in QCLs to the gratings of population inversion and coherences (medium polarization) induced by the standing cavity mode pattern. The authors attribute the onset of the RNGH instability at the turning-on process to the difference in the gain relaxation times T_1 on the diagonal (injector-active QWs) and vertical (within active QWs) transitions. On the other hand, the suppression of RNGH instability under EFD formation is explained by the washing out of the induced gratings by the inhomogeneous bias field and carrier distributions. In addition, in [74] is stated that the formation of a broad multimode emission (or a comb) with the overall spectral width of $\sim 2\Omega_{Rabi}$ (as opposed to the appearance of the mode clusters on the Rabi-frequency sidebands) is governed by the group delay dispersion in the cavity. Most importantly, in both cases the origin of the

multimode emission is related to RNGH instability. For spectroscopic applications of QCL combs [13], serious design efforts have been made to optimize active QWs, reduce group velocity dispersion and enlarge the spectral width of the gain curve on the active vertical transitions by incorporating several QWs with different transition energies.

The mechanism of instability in single-section QCLs that was proposed in [41] was linked to a parametric four-wave mixing gain instability, in full analogy with the phase-locked comb production in high-finesse optically pumped micro-cavities. Interestingly, as pointed out in [74] this mechanism should lead to a soliton formation in the time domain [44]. Nevertheless, very few measurements of the second-order interferometric autocorrelation (IAC) traces (see Appendix C) have been reported for QCLs [29], [39] and they don't provide an unambiguous conclusion about the output QCL waveform and eventually about the pulse shape. In addition, none of the previous reports indicated IAC variation in function of the pump current which otherwise would greatly streamline the identification of the dynamic behavior of QCLs in the time domain.

Note that all second-order IAC traces (see Appendix C) in DC-driven single-section FP cavity QCLs reported so far show the peak to background ratio close to 8:3, attesting rather a noisy (multimode) continuous wave (CW) lasing behavior [77] as opposed to formation of a pure phase-locked comb. Furthermore, none of the reported RF power spectra of intensity shows a comb with multiple harmonics of the fundamental cavity frequency- a feature which would confirm the phase locking of the optical modes [78], [79]. On the contrary, all RF power spectrum reports are limited to the beat note at fundamental frequency.

3.3. RNGH instability in a QCL with long cavity

As a model system for long-cavity devices we assume a single-section QCL with the cavity length of 4 mm. The linear stability analysis (Section 2.4) indicates the RNGH self-pulsations threshold [Eq. (3.1)] of $p_{th2}=1.05$. For the pump rate $p=1.2$, which is slightly above the instability threshold, we do observe a quasi-periodic chaotic behavior in the output power waveform [Fig. 3.5(a)]. Here the cavity round-trip time is 88 ps, much larger than the carrier lifetime T_1 (Table 1). Fig. 3.5(a) shows the first ten and the last ten cavity round-trips from the entire simulation domain which extends over 100 cavity round-trips. The laser is initially not pumped and the pump current is switched on at a time $t=0$ s. The onset of the lasing emission is seen in less than 3 cavity round-trips (at $t\sim 200$ ps, Fig. 3.5(a)). Comparing the self-pulsations in the first and last 10 round-trips in Fig. 3.5(a), one can see that after additional 3 cavity round-trips, the system reaches a steady regime of quasi-periodic (chaotic) self-pulsations, in good agreement with the inverse value of the gain coefficient in Fig. 3.2 (red curve, yielding $1/0.38=2.6$ round-trips). Therefore the considerations about thousands round-trips required to reach the steady operation do not apply for our single-section Fabry-Perot cavity laser [45]. In the original work of Risken and Nummedal [30], the steady regime of self-pulsations in a *unidirectional ring laser* is reached in less than 160 cavity round-trips. The carrier population grating and coherence grating in our *Fabry-Perot laser* not only drastically reduce the second threshold but also reduce the time needed for settlement of the self-pulsations. It is didactic to compare the build-up time of the lasing emission in Fig. 3.5(a) with an estimate based on the well-known text book expression that reads $\tau_c \ln(P_{LAS}/P_{SE})/(p-1)$ (see [66]). For the case considered in Fig. 3.5, the photon lifetime in the cavity is $\tau_c = 4$ ps while the power ratio in the steady lasing regime and in the initial regime of spontaneous emission (at $t=0$) is of $P_{LAS}/P_{SE} = 10^6$. For the pump excess above

threshold of $p=1.2$, the estimated build-up time is of 280 ps, which corresponds to 3 round-trips in the cavity. This estimate agrees very well with the rise time of the waveforms in Fig. 3.5 [45].

Once the lasing is reached, the round-trip gain coefficient for the multimode instability at $p=1.2$ becomes of 0.38 per cavity round-trip (see also [46]). That is, the amplitude of an unstable non lasing mode increases by a factor of $\exp\{0.38N\}$ after N round-trips. This process has the characteristic time scale of $1/0.38= 2.6$ cavity round-trip. Therefore reaching the steady regime of multimode self-pulsations just in additional 2-3 round-trips after the onset of lasing emission (by $t\sim 500$ ps in Fig. 3.5) appears very reasonable.

In the Fig. 3.5(b) we trace the evolution of the medium polarization P versus carrier density N . Both P and N values are taken in the vicinity of the laser facet and are normalized at transparency carrier density [47]. The P-N attractor has a characteristic butterfly shape typical for a chaotic behavior in a Lorenz-type system [80]. In total, QCL reaches the steady regime of chaotic self-pulsations just in 6 cavity round-trips (~ 530 ps). This time appears too short for establishing fixed phase relationships between many individual modes as in the case of actively mode-locked (ML) QCLs with built-in electroabsorber sections [81], [82]. However, the waveform in Fig. 3.5(a) clearly attests that our single-section QCL does not operate in ML regime. Indeed the peak to background ratio of IAC trace [corresponding to waveform in Fig. 3.5(a)] in Fig. 3.6 is worse than 8:3 while for a ML regime it should be close to 8:1 [77] (Appendix C). Thus, our quasi-periodic chaotic pulse train from Fig. 3.5 perfectly explains the experimentally measured IAC in [39], including nontrivial pulse structure in between cavity round-trips. The background-free intensity AC in Fig. 3.6 has the contrast of 2:1.75. This corresponds to the literature case of “noisy CW signal” [77]. Appearance of correlation peaks at cavity round-trips is due to the quasi-periodic nature of the waveform.

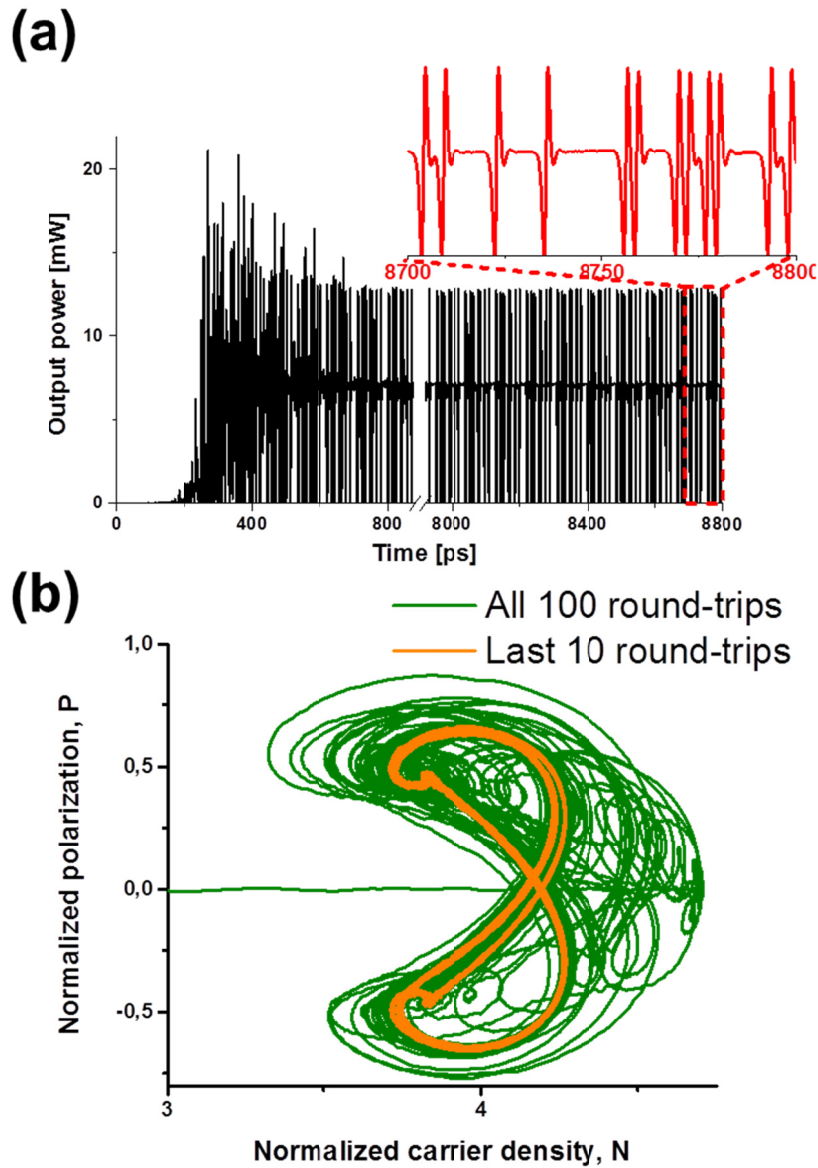


Fig. 3.5. Results of numerical simulations with TW model for 4mm long QCL (cavity round-trip time is 88 ps): Panel (a) depicts the output power waveform for the first ten and the last ten (out of 100) round-trips in the cavity with zoom on the last round-trip. (b) chaotic P-N attractor. The behavior during all 100 cavity round-trips is depicted with the green curve, while the orange curve signifies the last 10 round-trips, when the system reaches the steady regime of quasi-periodic (chaotic) self-pulsations. The QCL is pumped at $p=1.2$ times above the lasing threshold. Other parameters are shown in Table 1. © 2017 IEEE. Reprinted, with permission, from [45].

In relation to this example of non-regular pulse train we recall that observation of regular frequency comb in the optical spectrum does not indicate that the modes have fixed phase relationships and the laser produces a regular pulse train. With increasing pump rate, the optical field waveform develops into a quasi-periodic square wave [45].

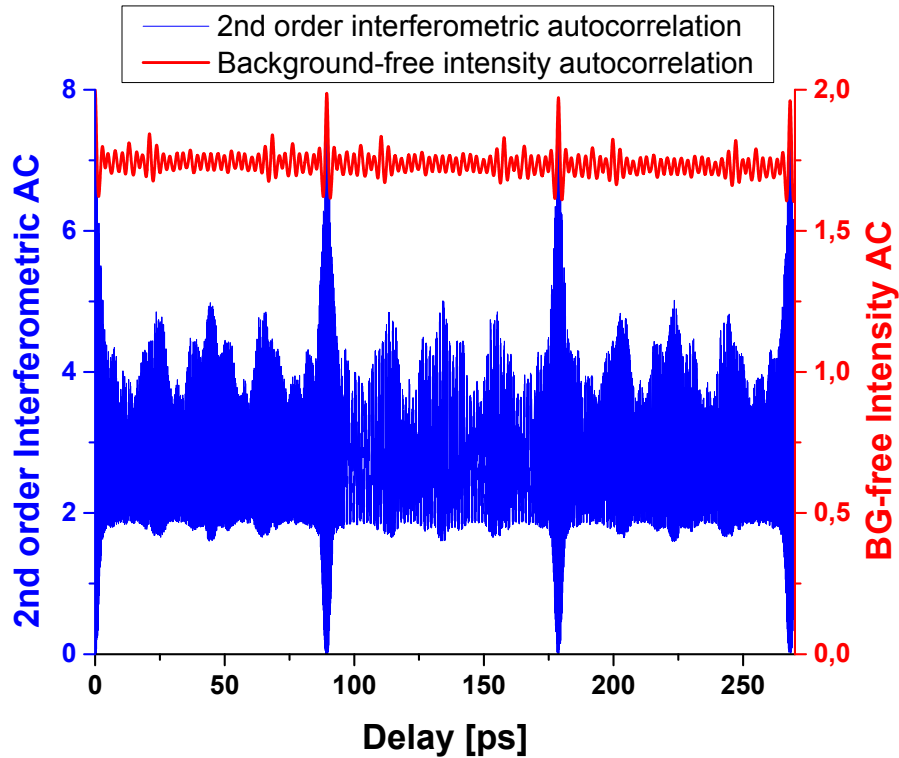


Fig. 3.6. Results of numerical simulations with TW model for 4mm long QCL (cavity round-trip time is 88 ps): Second-order interferometric AC (blue curve, left axis) and background free intensity AC trace (red curve, right axis) corresponding to the waveform in Fig. 3.5. The QCL is pumped at $p=1.2$ times above the lasing threshold. Other parameters are shown in Table 1. © 2017 IEEE. Reprinted, with permission, from [45].

An example of the temporal behavior of the optical field amplitude, medium polarization and carrier density is depicted in Fig. 3.7. The optical field behavior [Fig. 3.7(a), black curve, left axis] appears to be quite similar to the one predicted by *Lugiato et al.* in [64] for a long-cavity unidirectional ring laser

at high pump rates. However, in our case the average field amplitude is zero due to quenching of the initially CW lasing mode and emergence of the two symmetric sidebands in the optical spectrum. Like the optical field, the medium polarization shows the square-wave behavior. However, its waveform pattern is not identical to that one of the optical field [Fig. 3.7(a), red curve, right axis]. This is not surprising if one takes into account the scattering of counter-propagating waves on the induced gratings of carrier coherence and population. Most importantly, the medium polarization does not follow the optical field adiabatically. Instead, the medium polarization itself defines the optical field dynamics [45].

One can see in Fig. 3.7(a) that the pattern of the square wave almost repeats itself after each round-trip in the cavity (88 ps), indicating that a wave packet with complex envelope travels back and forth in the cavity. Its envelope just slightly changes at each round-trip, yielding the quasi-periodic chaotic behavior. A different pattern is seen in the waveforms of the optical power and carrier population [Fig. 3.7(b), left and right axis respectively]. These variables are either quadratic with respect to the optical field or have a contribution from the product of the optical field amplitude and the medium polarization [see Eqs. (2.7)-(2.11)]. Each waveform in Fig. 3.7(b) exhibits spikes that are superimposed on a steady level. The spikes are caused by intermittent behavior of the optical field and polarization, while the steady-state component attests for the symmetry of the field and polarization square wave patterns. The period of spikes is roughly a half of that for polarization waveform, yielding the Lorenz-type attractor as shown in the Fig. 3.5(b) [45].

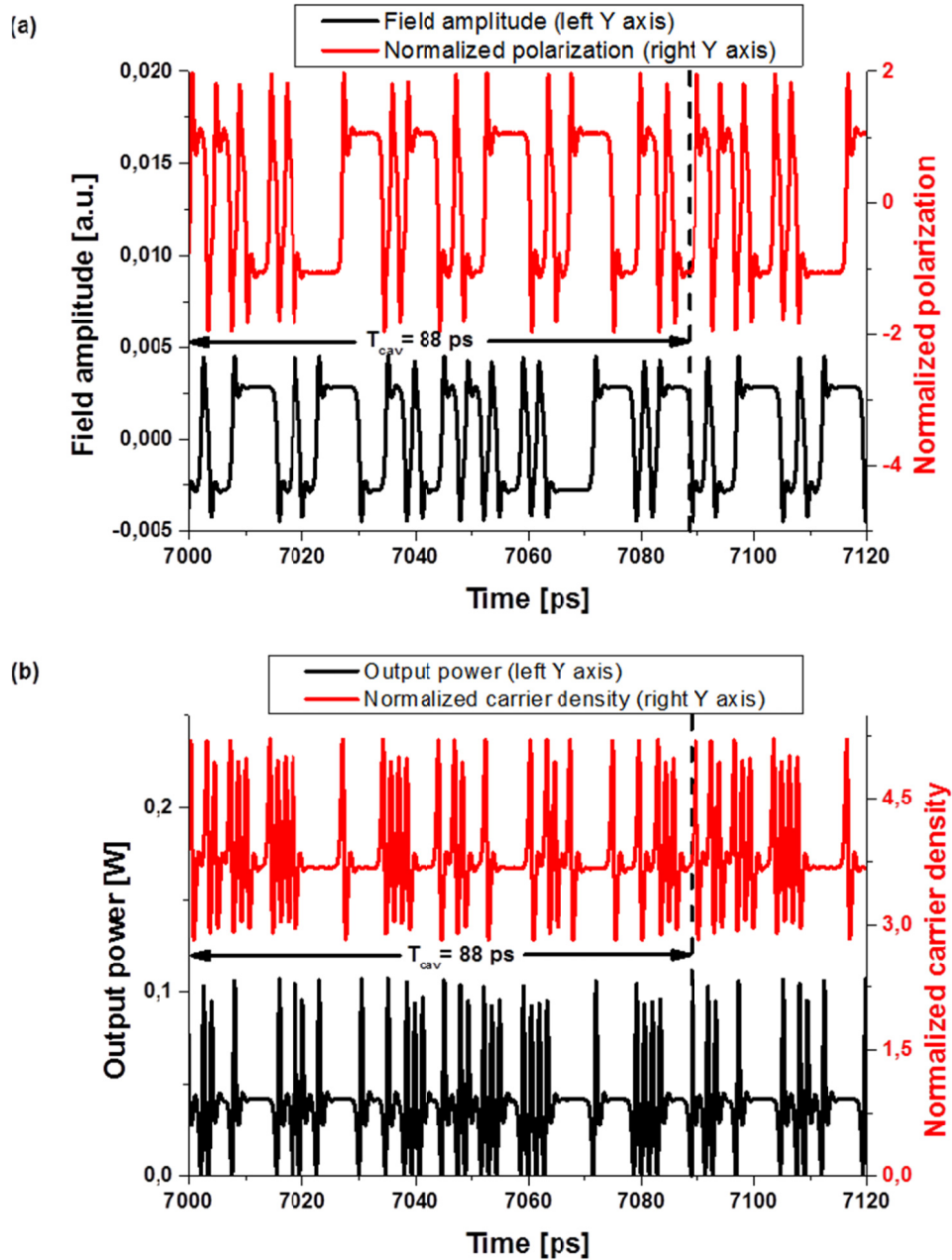


Fig. 3.7. Results of numerical simulations with TW model for QCL with the cavity length of 4 mm: The optical field waveform and normalized medium polarization for the wave propagating in the positive z axis direction (a), output power and normalized carrier density (b). All values are taken nearby the output facet of the laser cavity. The QCL model parameters are the same as in Fig. 3.5 but the pump rate is of $p=2.2$. © 2017 IEEE. Reprinted, with permission, from [45].

All these features seen in the time-domain waveforms are directly imprinted into the optical and radio frequency (RF) spectra. In Fig. 3.8(a) we show evolution of RF spectra with the pump rate and compare it with the Rabi oscillation frequency. Due to the standing wave pattern of the optical field in the cavity and induced carrier coherence and carrier population gratings, there are several Rabi oscillation modes in the cavity. In order to extract their frequencies, we have made an additional small-signal analysis of Eqs. (2.7)-(2.11). This time, we keep fixed the amplitude of the optical standing wave in the cavity. We find that Rabi oscillations are possible at the main frequency Ω_{Rabi} as well as at the two other frequencies $(1+2^{-1/2})^{1/2} \Omega_{Rabi}$ and $(1-2^{-1/2})^{1/2} \Omega_{Rabi}$, where [45]:

$$\Omega_{Rabi} = \sqrt{\frac{p - \nu_0(p)}{T_1 T_{2_eff}}} \quad (3.2)$$

Out of these three eigenmodes, only the main one (3.2) is associated with the gain medium variables in the lower 4×4 matrix block of Eq. (2.26), the one which is responsible for RNGH instability. In Fig. 3.8, we also compare the extracted spectra with the evolution of the peak gain frequency Ω_{max} for multimode RNGH instability (see Fig. 3.1) as well as with the possible frequency of multimode instability due SHB effect, which is predicted in [39] to be well below Ω_{Rabi} and Ω_{max} :

$$\Omega_{SHB}^{[39]} = \sqrt{\frac{1}{T_1} \sqrt{\frac{p-1}{3T_1 T_2}}} \quad (3.3)$$

All these frequencies (Ω_{Rabi} , Ω_{max} , and $\Omega_{SHB}^{[39]}$) are obtained using a small-signal approach. Because the optical power is $\propto E^2$ while the carrier dynamics is governed by terms $\propto EP$, in Fig. 3.8(a) and Fig. 3.8(b) we plot these

frequencies scaled by a factor of 2. Note that the peak gain frequency Ω_{max} is quite close to the Rabi oscillation frequency (compare the red and blue curves in Fig. 3.8).

The evolution of the RF power spectrum in Fig. 3.8(a) almost follows along the curves for $2\Omega_{Rabi}$ and $2\Omega_{max}$ frequencies, exhibiting the spectral broadening and the frequency shift of the modulation band that increases with the pump rate. Note however that it is unrealistically to expect the exact matching between the numerical simulations for large-amplitude self-pulsations and the outcomes of the small-signal analysis. At the same time the spectral broadening and the frequency shift in Fig. 3.8(a) are clearly much larger than for a possible multimode instability at the frequency $\Omega_{SHB}^{[39]}$ due to SHB [39] (green curve). Therefore we attribute the spectral behavior in Fig. 3.8(a) to RNGH-like instability. Since the output power waveform as in Fig. 3.7(b) can be regarded as a series of ultrafast spikes superimposed on a steady intensity level, the modulation band seen in the RF power spectrum at the frequency $2\Omega_{Rabi}$ is primarily due to the spiking behavior of the output power [45].

In Fig. 3.8(b) we plot the frequency-domain representation of the carrier density dynamics at different values of p . The spectra show broadening and modulation of the carrier density at frequencies up to twice the Rabi oscillation frequency. This behavior is similar to the evolution of RF spectra in Fig. 3.8(a). However, the modulation band nearby $2\Omega_{Rabi}$ is less pronounced and the spectra exhibit almost all frequency components down to $\Omega = 0$. This behavior can be attributed to a slow response of the carrier density and carrier population grating to rapid variations $\propto EP$ in Eqs. (2.10)-(2.11). The cutoff frequencies are of $1/2\pi T_1 = 122$ GHz and $1/2\pi T_g = 172$ GHz for the average density and population grating, respectively.

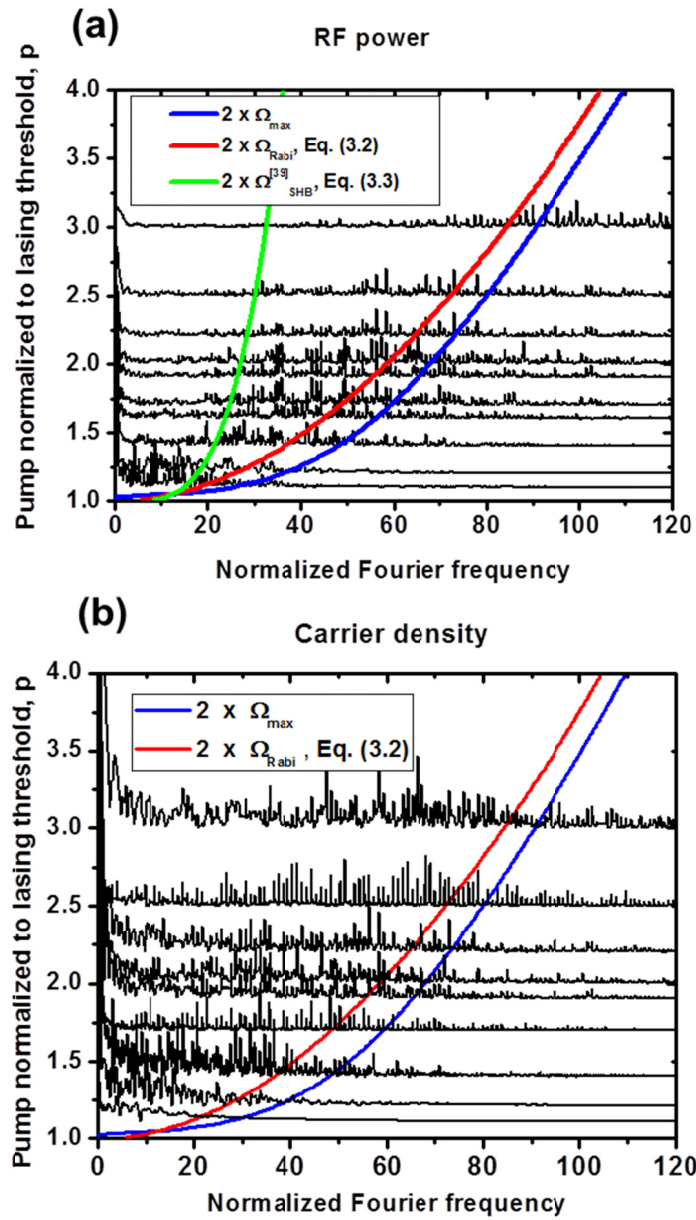


Fig. 3.8. Results of numerical simulations with TW model for QCL with the cavity length of 4 mm: Evolution of QCL (a) RF power spectra, (b) carrier density spectra, when pumped above the lasing threshold. Red and blue curves indicate expected location of modulation sidebands originating from Ω_{Rabi} and Ω_{\max} . The green curve shows that one for $\Omega_{\text{SHB}}^{[39]}$. The frequency is normalized to longitudinal mode spacing of 11.4 GHz. The model parameters are the same as in Fig. 3.5 and Fig. 3.7. © 2017 IEEE. Reprinted, with permission, from [45].

The optical power spectra and the medium polarization waveforms in the frequency domain representation are displayed in Fig. 3.9(a) and Fig. 3.9(b), respectively. As expected, the two sets of spectra show very good resemblance. In both sets, the initially lasing mode at $\Omega = 0$ (the carrier wave) is quenched and the spectra reveal two symmetric sidebands. Since the RF modulation spectra of the output power exhibit modulation bands at the frequency $2\Omega_{Rabi}$ [see Fig. 3.8(a)] one would expect to observe the modulation sidebands at frequencies $\pm\Omega_{Rabi}$ in the optical spectra as well. However, these considerations do not take into account large phase variations due to intermittent behavior of the optical field, as seen in Fig. 3.7(a). Obviously, the phase of the optical field does not contribute to the RF power spectrum.

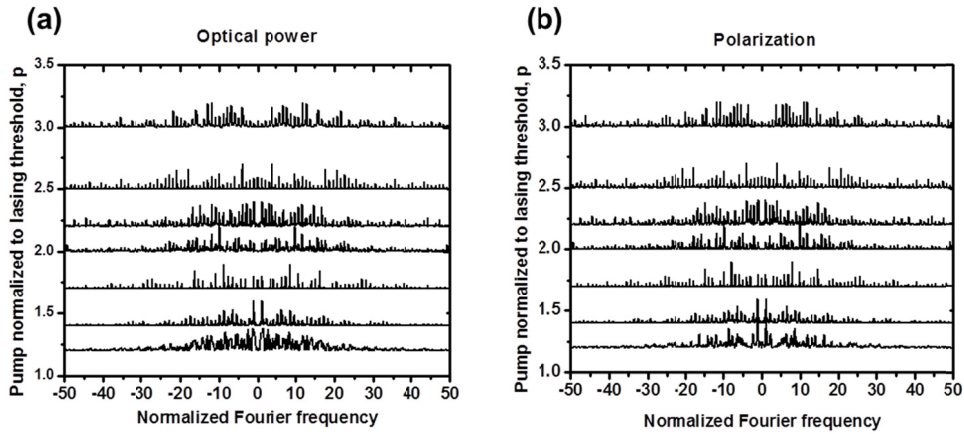


Fig. 3.9. Results of numerical simulations with TW model for QCL with the cavity length of 4 mm: Evolution of QCL (a) optical power and (b) polarization spectra when pumped above the lasing threshold. The frequency is normalized to longitudinal mode spacing of 11.4 GHz. The model parameters are the same as in Fig. 3.5 and Fig. 3.7. © 2017 IEEE. Reprinted, with permission, from [45].

At the same time, the large phase hops of $\pm\pi$ impact directly the overall optical spectrum, warping its envelope as compare to the envelope of the RF power spectrum. From the waveform in Fig. 3.7(a) one can see that the

average repetition frequency of such phase hops is much lower than the spectral band of each spike in Fig. 3.7(b). As a result, the modulation sidebands in the optical spectrum are shifted to lower frequency. Therefore one of the possible origins for experimentally reported clamping of the optical spectrum bandwidth (see Sec. 3.2) is that the optical field waveform develops into a quasi-periodic square wave, showing the intermittent behavior [45].

3.4. RNGH instability in a QCL with short cavity

We now move on to the case of short-cavity QCLs and consider an example of QCL with the cavity length $L=100\ \mu\text{m}$, for which the linear stability analysis predicts the RNGH threshold [Eq. (3.1)] of $p_{th2} = 2.35$ (see Fig. 3.2, solid blue line).

The results of TW model simulations for the pump rate of $p=1.5$, which is below the second threshold, are shown in Fig. 3.10(a) and Fig. 3.10(b).

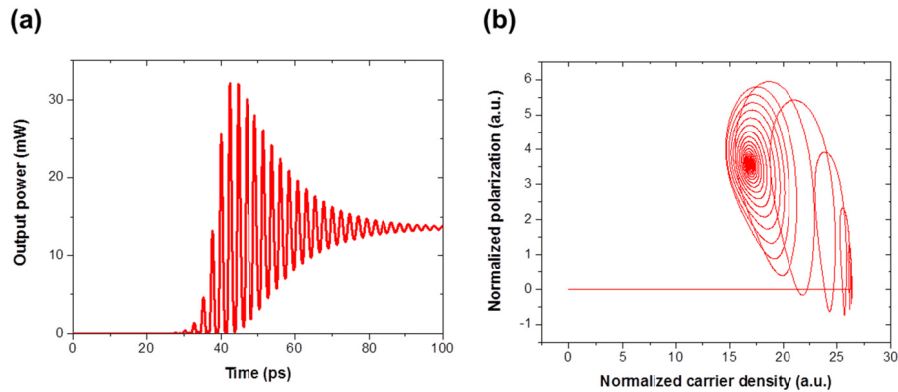


Fig. 3.10. Results of numerical simulations with TW model for QCL with the cavity length of $100\ \mu\text{m}$: Waveform (a) and P-N attractor (b) in case of $p=1.5$ (below 2nd threshold), the system is stable.

After several round-trips in the cavity, the laser reveals an onset of damped relaxation oscillations and a transit to CW lasing regime, as can be seen from both output power waveform [Fig. 3.10(a)] and spiral-shape P-N attractor [Fig. 3.10(b)]. The model simulations are thus in agreement with the predictions of the linear stability analysis in Fig. 3.2.

The QCL reveals a different behavior when pumped above the second threshold. At pump rate above the instability threshold, e.g. at $p=2.5$ as in Fig. 3.11, the first emission burst of high peak power is followed by steady regime of regular self-pulsations [Fig. 3.11(a)] [45]. The FWHM pulsewidth of the first emission burst is of 0.5ps while for regular self-pulsations it is of 0.6 ps width. The system attractor plotted in the P-N plane indicates that the laser transits to regular self-pulsations (or even self-oscillations) just after a few round-trips in the cavity [inset of Fig. 3.11(a)] once it is at lasing. The period of regular self-pulsations is close to the cavity round-trip time of 2.2 ps with the optical field amplitude (and the medium polarization) changing sign at each half period. This can be seen from the 8-like shape of P-N attractor in inset of Fig. 3.11(a). This behavior attests that this is not a usual mode-locking regime. In Fig. 3.11(b) the contrast ratio of the interferometric AC is 8:1.5 (blue curve, left axis) and the one for background-free intensity AC (red curve, right axis) is of 2:0.6. Although the process is coherent, the IAC does not reach the peak-to-background ratio of 8:1 (2:0) because intensity pulse width is close to the period of intensity self-pulsations.

Fig. 3.11(c) and Fig. 3.11(d) show the optical and RF power spectra respectfully, when the pump rate p is in the range of 2.2 to 3.9 times above the lasing threshold. In case of short-cavity QCL operating at just above the instability threshold, only two main frequency components are excited in the optical spectrum [Fig. 3.11(c)]. With increasing pump rate, the spectrum remains symmetric with respect to initially lasing mode and the two main

spectral components are located at the two nearest-neighbor modes. The multimode RNGH instability occurs when the frequency Ω_{\max} of the maximum gain for instability is on resonance with the first adjacent cavity mode [Fig. 3.11(c), blue curve]. However, with increasing pump rate, the frequency of self-pulsations does not follow the increasing frequency Ω_{\max} or Rabi oscillation frequency (red curve). Higher order modes start to appear in the optical spectrum as opposed to continuous frequency rise. We attribute this behavior to the cavity round-trip self-repetition condition (see Section 2.4). With the increase of normalized pump p the waveform is still periodic but it changes from regular sine-like shape to some more irregular one since more spectral components are included with the increase of pump p . Eventually it will become square wave for $p \sim 5$ (values that are not of practical importance).

Note that the frequency of self-pulsations is slightly lower than the cold cavity mode spacing due to the group velocity reduction. It can be attributed to propagation phenomenon of a high-energy pulse in resonant medium, the process which can be regarded as continual absorption of energy from the pulse leading edge and re-emission of energy into the pulse trailing edge [72].

A quite similar behavior is reported in [64] for a short-cavity unidirectional ring laser. However, in case of the ring laser, the optical field does not change the sign at each half-period. As a consequence, the main lasing mode at $\Omega = 0$ is not quenched. One can trace a few other similarities between multimode instability in QCLs discussed here and the RNGH instability in unidirectional ring lasers from [64]. In particular, one very important question has been challenged but has not been answered in [64]. More specifically, the mechanism, which is responsible for regular self-pulsations in case of short-cavity laser and chaotic pulsations in the long-cavity case, has not been elucidated. This qualitative change in dynamic behavior becomes even more wondering if one considers the affinity between the 8-shape attractor in case of

regular self-pulsations in Fig. 3.11(a) and the butterfly-shape attractor in case of chaotic self-pulsations in Fig. 3.5(b).

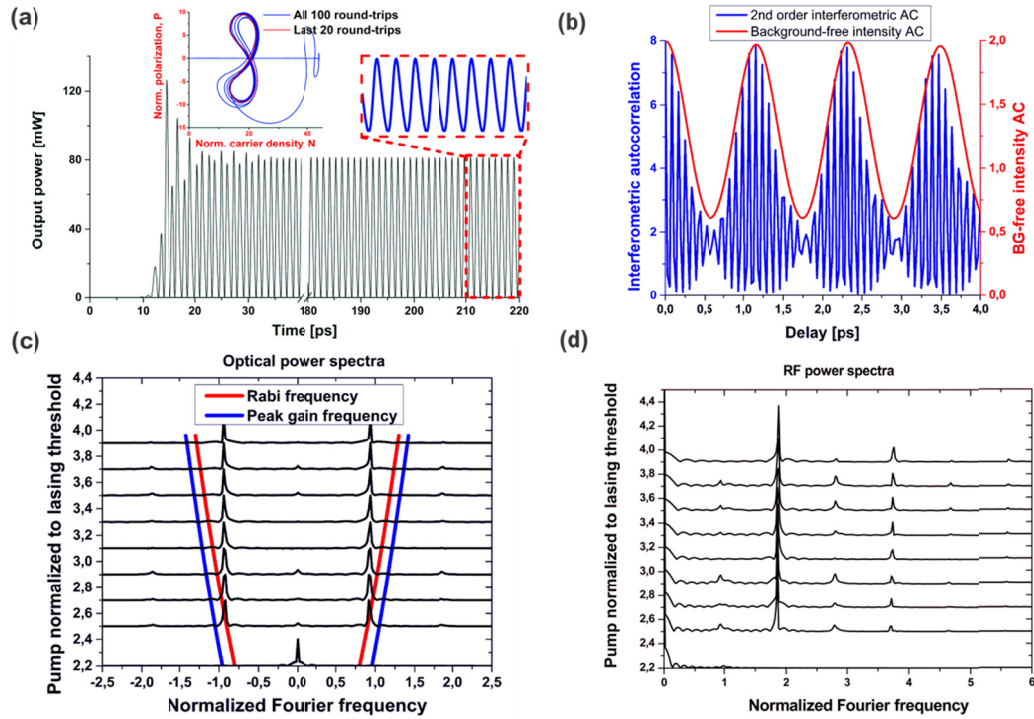


Fig. 3.11. Results of numerical simulations with TW model for QCL with the cavity length of 100 μm : (a) Waveform: zoom- in at the end of the simulation domain shows regular self-pulsations with sub-picosecond pulse width. Inset shows P-N attractor. (b) AC traces. In (a) and (b) $p=2.5$ (above the RNGH threshold). (c) Evolution of the optical spectrum with the pump rate. (d) RF power spectra which shows the main harmonic at about twice of the cold cavity mode spacing. © 2017 IEEE. Reprinted, with permission, from [45].

3.5. Comment on coherence length

Now we will address one possible explanation on the effect of the cavity length. To get an insight into its cause we study the P-N attractors in further details. The P and N variables used in this work are introduced following the approach of Ref. [47]. In particular, the variable P measures the order

parameter in the system (the carrier density in the coherent state) and has the same units as the carrier density N . In Fig. 3.5(b), Fig. 3.10(b) and Fig. 3.11(a) inset, both variables P and N are normalized on the transparency carrier density [45].

In Fig. 3.11 the order parameter P is high. It reaches about a half of the value for N that precedes the emission pulse when $P=0$. This feature is observed as in the first emission burst [Fig. 3.11(a) inset, blue line] as well as in the regime of regular RNGH self-pulsations [Fig. 3.11(a) inset, red line]. This behavior indicates an “off-diagonal long range order” in the system, as predicted in the pioneering paper by Graham and Haken [31]. Note that a similar behavior is also predicted for Dicke superradiance (SR) [47], [83]. The similarity is even far more striking. Thus as shown in [31], the master equation for RNGH instability behavior can be put in the form that bears a closed formal analogy to the description of condensation phenomena, such as superconductivity. But in [47] (and also in [84]), the SR emission is also shown to be governed by the master equation in the form of Ginzburg-Landau equation. Continuing these parallels we note that in the pioneering work of Risken and Nummedal [30], the approximate analytic solution for the regime of RNGH self-pulsations was obtained in the form of a hyperbolic secant pulse. This was achieved by considering the case, in which the optical field is entirely defined by the medium polarization, so as $E \propto P$. The same relationship between E and P as well as the same hyperbolic secant pulse shape applies to the case of Dicke superradiance [47], [85]. There is however one important difference between the two regimes. The RNGH instability is usually analyzed in a CW operating laser when the active medium is under continuous wave pumping. The SR pulse emission occurs from a strongly pumped active medium, when the initial optical field is close to zero. In practice this is achieved with pumping by short and intense optical or electrical pulses [83], [85]–[89].

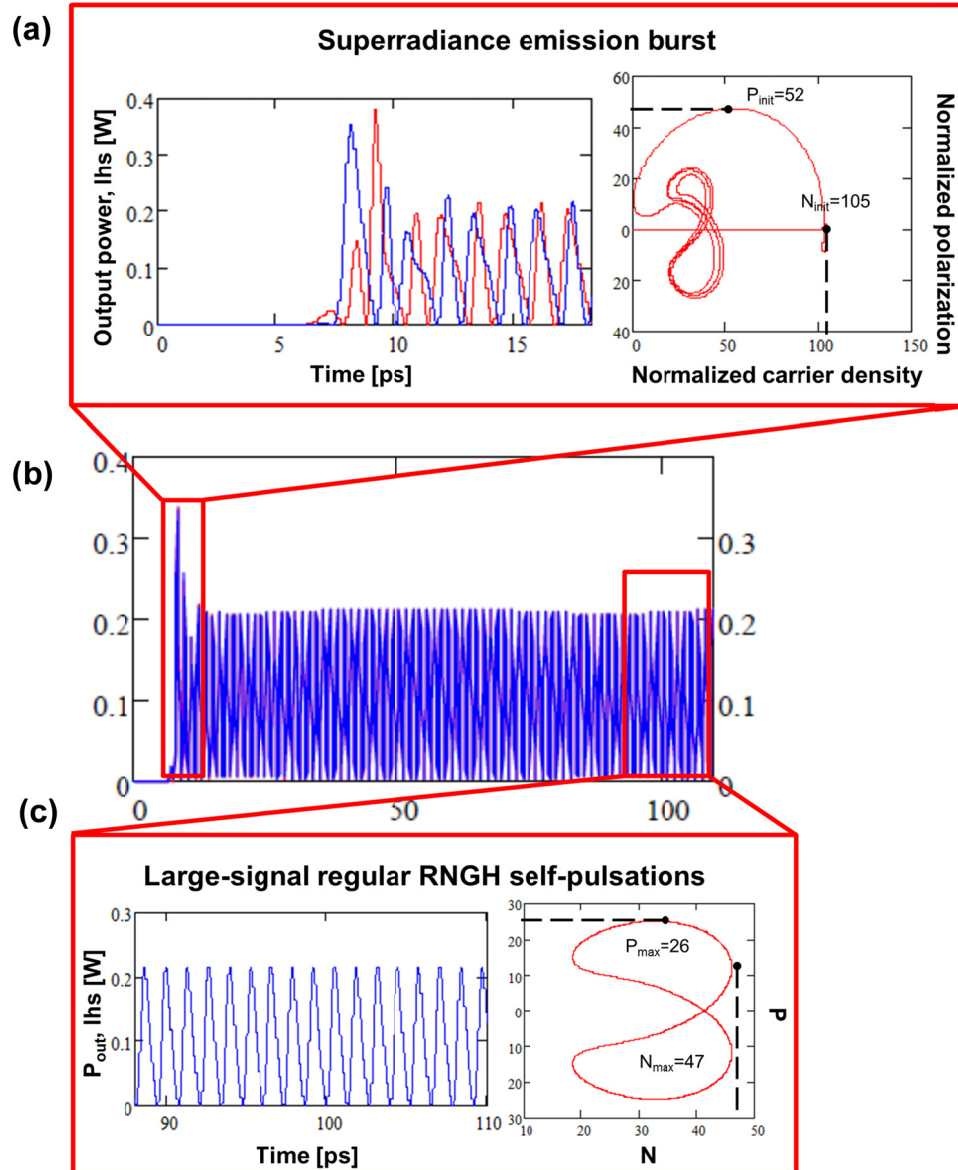


Fig. 3.12. TW model simulation for short cavity QCL ($L=100 \mu\text{m}$) just above lasing threshold ($p=2.5$), with $R_1=R_2=2.7\%$. All other parameters are from Table 1: (a) Zoom at the burst, where blue and red lines on the left panel represent output power trace on left (left hand side, I_{hs}) and right facet, respectively. Right panel is P - N attractor which shows that normalized initial carrier density (102) is approximately twice the normalized initial polarization (52), a characteristic feature of the ideal superradiance. (b) Time trace of output power which shows train of pulses preceded by a large burst. (c) Zoom at the end of simulation domain: periodic train of ultrashort (sub picosecond) pulses (left) and their P - N attractor. Reprinted by permission from Springer Nature, *Opt. Quantum Electron* [58] © (2016).

Taking all these considerations into account, we attribute the first emission burst in Fig. 3.11(a) to SR [45]. In order to more systematically show this behavior with zoom on superradiance burst and subsequent regular oscillations, we plot in Fig. 3.12 waveforms from a different realization for a QCL with the same length (100 μm) but with different reflectivity coefficients [Thus there are differences in the values of peak output power, P and N compared to Fig. 3.11(a)] [58].

It was shown that SR in short samples is different from the cooperative emission in long samples [47], [84], [90]. The borderline between the two cases is set by the coherence length of the SR pulse. In case of long samples, the situation is such that sample domains of the size of the coherence length emit independently of each other. The output pulse is the result of incoherent superposition of SR emission from different sample domains. As a result, the overall pulse width broadens and its amplitude decreases [45].

In a similar way, we may conjecture that the regular RNGH self-pulsations occur when the sample is shorter than the coherence length. Otherwise, in the case of a long sample, different sample domains are not mutually coherent with respect to instable cavity modes and compete with each other at the initial stage. As a result, an erratic pattern of the field is established in the cavity at a later stage. As seen in Fig. 3.7, the optical field pattern almost repeats itself on subsequent round-trips in the cavity, however the coherence length remains smaller than the cavity length. It is roughly the average time between the phase hops in Fig. 3.7(a), red curve.

The coherence time measured from the IAC trace in Fig. 3.6 as a half-width at half maximum (HWHM) of the central lobe above the background is about 2 ps, which corresponds to the duration of the transients in Fig. 3.5(a) (and Fig. 3.7(a)). The coherence length is thus about 180 μm which is very short compared to the millimeter cavity length. On the other hand, in short-cavity

QCLs, the coherence time is comparable to a single pass through the sample. The IAC traces in Fig. 3.6 and Fig. 3.11(b) provide an evidence for this keystone difference [45].

3.6. The role of carrier diffusion

We have shown in Section 2.3 that the carrier coherence grating and carrier population grating are both responsible for lowering the multimode instability threshold. The diffusion coefficient D , which affects their effective relaxation times T_g , T_{2_g} and $T_{2_{eff}}$, is sensitive to the temperature. Unfortunately the literature data about the temperature effect on RNGH self-pulsations are quite controversial (see Sec. 3.2), which is likely because the temperature also affects many other QCL parameters. On the other hand, the relaxation rates enhancement due to the carrier diffusion is proportional to the square of the photon wavenumber k [see the discussion to Eqs. (2.7)-(2.11)]. Therefore we elucidate the role of the carrier diffusion by considering various emission wavelengths.

First we consider the case of QCLs emitting in the MIR spectral range and discuss the effect of electron diffusion in the plane of active QWs in these devices. In Fig. 3.13 we compare the increments for multimode RNGH instability in QCLs samples emitting at 4 μm (green curve) and 10 μm (red curve) wavelengths. Without carrier diffusion, the second threshold is unrealistically low, at below $p=1.005$ in long-cavity samples (black dash-dotted curve). The relaxation due to diffusion raises the second threshold. As expected, this effect is more pronounced for shorter wavelength QCLs, where relaxation is faster (compare red and green curves). Thus for devices with the cavity length of 4 mm, the second threshold p_{th2} is of 1.04 at the wavelength of 10 μm , while $p_{th2}=1.32$ in QCL emitting at 4 μm . The effect of the diffusion on

the second threshold is seen as in the long cavity devices (solid curves) as in the short cavity QCLs (vertical dashed lines). In all considered cases, the carrier diffusion does not raise the second threshold to prohibitively high levels [45], [58], [91].

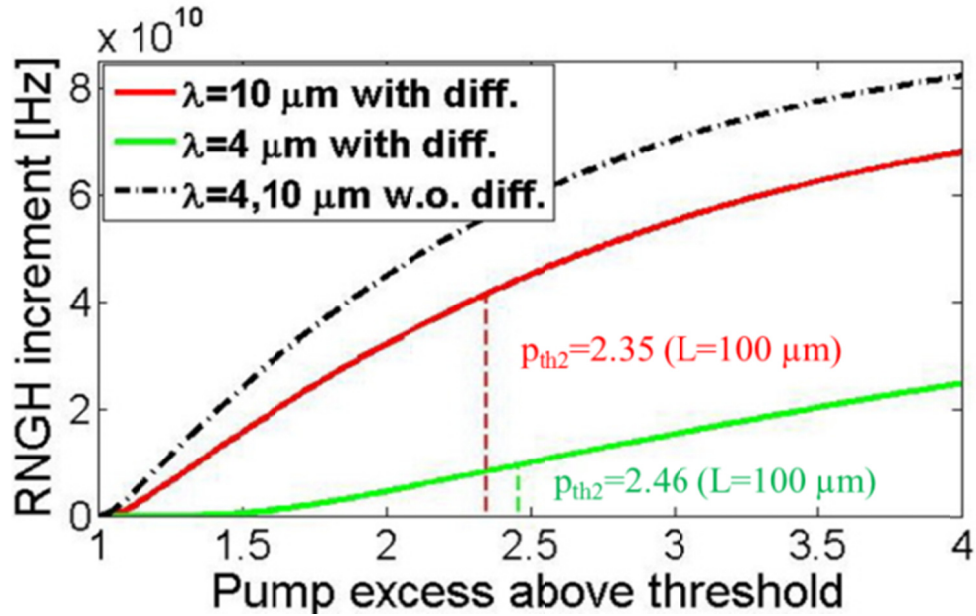


Fig. 3.13. Maximum RNGH instability increment vs pump excess above threshold for QCLs without relaxation due to carrier diffusion (black dash-dotted curve) as well as with the effect of the carrier diffusion when the emission wavelength is 4 μm (green curve) or 10 μm (red curve). The solid curves are obtained for long-cavity devices ($L=4\text{ mm}$), while the vertical dashed lines denote the second threshold for short-cavity devices ($L=100\text{ }\mu\text{m}$). Other parameters are indicated in Table 1. Reprinted by permission from Springer Nature, *Opt. Quantum Electron* [58] © (2016).

The implication of the carrier diffusion effect is totally different in the case of QW laser diodes operating in the visible (VIS) or near infra-red (NIR) spectral range. Even though the ambipolar diffusion in the QWs of these devices is much weaker than the diffusion of electrons in QCLs (see Table 1), the relaxation due to diffusion is more perceptible because of the shorter wavelength and smaller spatial period of the induced gratings. It is commonly

acknowledged that QW laser diodes with monolithic FP cavities do not show RNGH instabilities in the range of pump currents that can be reached in practice.

In Fig. 3.14, we study the increment for multimode RNGH instability in a FP-cavity GaN semiconductor laser diode operating at 420 nm and in a GaAs LD at 850 nm wavelength. In all cases examined in Fig. 3.14, the two LDs show quite similar behavior. In Fig. 3.14(a) and Fig. 3.14(b) we consider, respectively, the eigensolutions of the 4×4 and 5×5 matrix blocks in Eq. (2.26) and plot the largest real part of the Lyapunov exponents. The first matrix is related to the instability caused by the carrier population and carrier coherence gratings, which is the focus of this paper. The second matrix would reproduce the results of the original RNGH theory if both induced gratings are removed ($T_g, T_{2_g} \rightarrow 0$) while the carrier relaxation and carrier dephasing processes preserve their initial times scale (T_1 and T_{2_eff}). Recall that the RNGH theory [30], [31] was originally established for a *unidirectional ring laser*, where the gratings cannot be formed. It predicts the second threshold p_{th2} at more than 9 times above the lasing threshold. The second threshold of the original RNGH theory would be recovered by our model if, in particular, $T_{2_g} / T_{2_eff} \rightarrow 0$ (see Section 3.7 below). However, neither with carrier diffusion ($T_{2_g} / T_{2_eff} \sim 0.5$ see Table 1) nor without it ($T_{2_g} = T_{2_eff}$), the VIS-NIR LDs cannot reach this condition. As a result, the second threshold emerging from the 5×5 matrix block in Eq. (2.26) is very high in the VIS-NIR LDs (Fig. 3.14(b)) due to the presence of induced gratings [45], [58].

The carrier coherence and carrier population gratings have a different implication on the instability emerging from the 4×4 matrix block [Fig. 3.14(a)]. Thus in a *FP cavity lasers* as we consider here the induced coherence and population gratings lower significantly the second threshold.

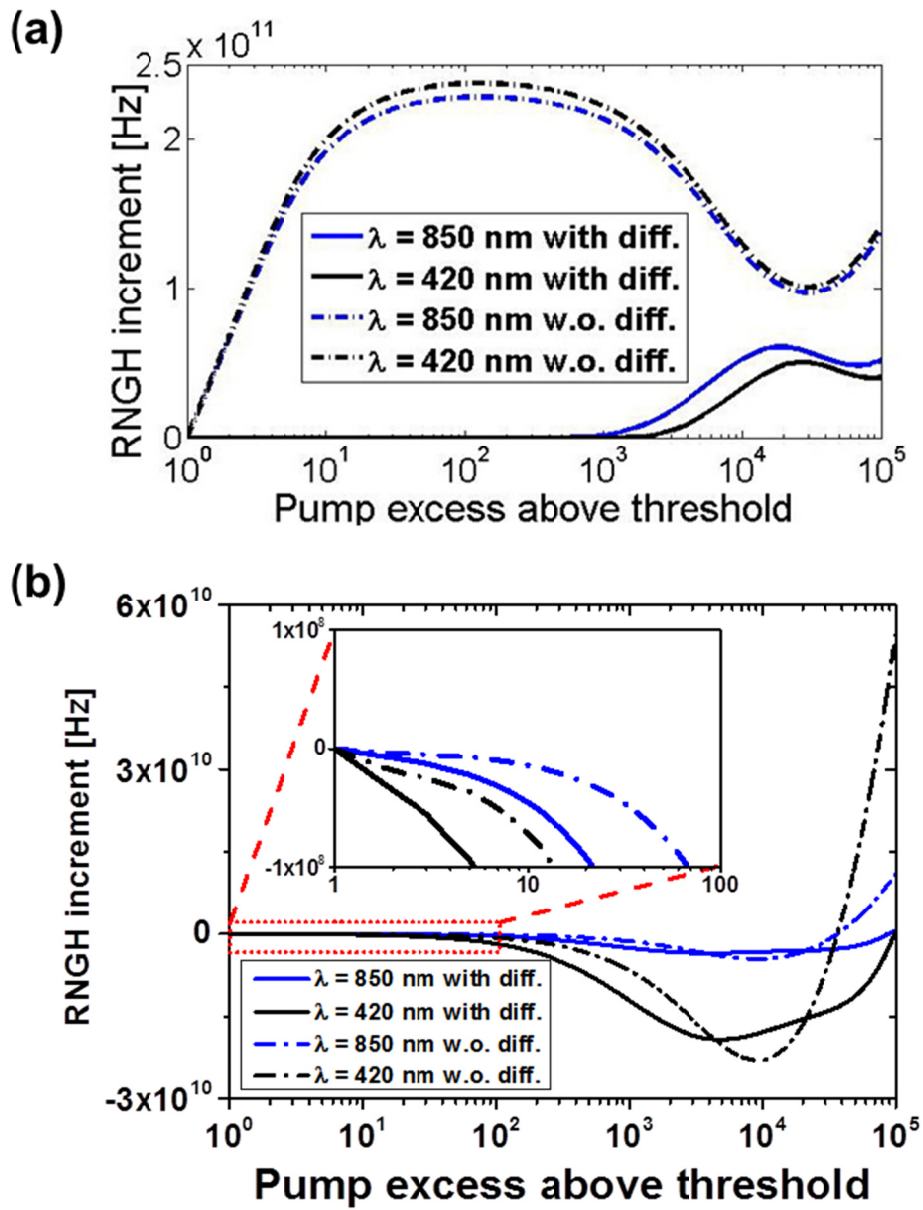


Fig. 3.14. (a) Maximum RNGH instability increment from the 4x4 matrix block in Eq. (2.26) [Reprinted by permission from Springer Nature, *Opt. Quantum Electron* [58] © (2016).] and (b) largest real part of the Lyapunov exponent from the 5x5 matrix block vs pump excess above the lasing threshold for GaN LDs (black curves) and GaAs LDs (blue curves), calculated with and without carrier diffusion (solid curves and dash-dotted curves respectively) calculated from (a) 4x4 and (b) 5x5 matrix block. Inset in (b) shows zoom at p from 1 to 100. The cavity length is $L=4$ mm, other parameters are shown in Table 1.

However, without the ambipolar diffusion of carriers, the model predictions for the second threshold in VIS-NIR LDs would be unrealistically low, of $p_{th2} \approx 1$ (dash-dotted curves in Fig. 3.14). The relaxation due to the carrier diffusion renders our model to be more realistic (solid curves in Fig. 3.14(a)) because the characteristic time constants $T_1=1$ ns and $T_2=0.1$ ps are now reduced to much shorter effective relaxation times of $T_g=0.1-0.2$ ps for the carrier population grating, $T_{2_g} \sim 0.05$ ps for the coherence grating and $T_{2_{eff}} \sim 0.09$ ps for the effective dephasing rate. This lifetime reduction strongly suppresses all effects induced by the standing wave pattern of the optical field in the cavity. As a consequence, the second threshold values predicted from the linear stability analysis are of several hundred times above the lasing threshold, as indicated in Fig. 3.14(a) [58], [91]. Recall that this analysis is based on the truncated set of coupled-mode equations (2.7)-(2.11) and the model predictions for the second threshold cannot be quantitatively accurate at such a high pump rate. Nevertheless these predictions are in a reasonable agreement with the outcomes of our numerical simulations based on the TW rate equation model, which we discuss next.

In Fig. 3.15 we show the output waveform and P-N attractor simulated numerically with TW model for a 100 μ m long single-section GaN LD pumped above the second threshold, at $p=400$ [45], [91]. At such high pump rate, LD exhibits behavior that is similar to QCLs biased at above the RNGH instability threshold. The output waveform at each cavity facet reveals the SR emission burst followed by regular RNGH self-pulsations [compare to Fig. 3.11(c) and Fig. 3.12]. Note that during the SR emission burst, the order parameter is large and approaches a half of the initial carrier density stored in the system. At the pump rates below second threshold, LD shows an ordinary behavior of a Class-B laser, which is characterized by excitation of damped relaxation oscillations followed by a transition to CW lasing regime [as in Fig. 3.10(a)].

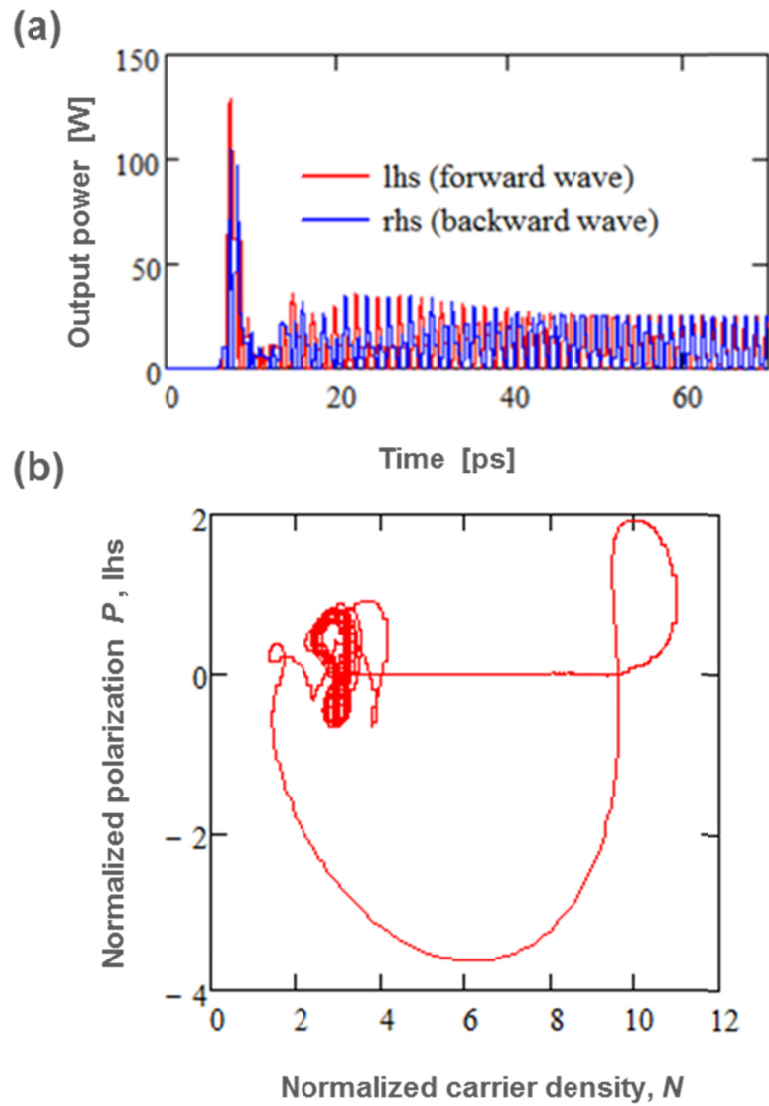


Fig. 3.15. Results of numerical simulations with TW model for GaN LD with the cavity length of $100 \mu\text{m}$: Waveform (a) and P-N attractor (b). The red (blue) trace corresponds to the wave propagating in the forward (backward) direction. © 2017 IEEE. Reprinted, with permission, from [45].

We thus conclude that VIS-NIR range QW LDs have very high second threshold because of rapid relaxation of the carrier coherence and population gratings. Whereas the RNGH instability threshold in single-section QW LDs is

not reachable under realistic experimental settings, there are several considerations that indirectly support our conclusion.

Reaching the SR emission in short-length mesa-etched structures comprising GaAs QWs was attempted in [92] under short-pulse optical pumping. However, no evidence of SR emission was observed. We may attribute this to the fact that threshold condition for RNGH instability has not been reached in these experiments as the pump rate was too low.

According to Fig. 3.14, lowering of RNGH instability threshold (and reaching SR emission) in single-section LD can be achieved by reducing the contribution of diffusion to the relaxation rates of the carrier coherence and population gratings. This brings us to the insight that low-dimensional semiconductor heterostructures such as quantum dots (QDs) or quantum dashes (QDash) can be used as active gain material in order to avoid prohibitively high second threshold. Surprisingly, in Ref. [93], starting from totally different considerations, a similar conclusion was made about semiconductor heterostructures suitable for SR emission. Thus according to [93], SR emission is not possible with the active gain medium utilizing bulk semiconductor material or QW heterostructures. One needs to use QDs or to introduce an additional quantization degree in a QW by applying a strong magnetic field. The SR emission from magneto-excitons in InGaAs/GaAs QW was confirmed in [85] under short-pulse optical pumping.

There is another way to reduce the second threshold in a semiconductor laser. It consists in incorporating a saturable absorber [40] (see also Introduction and Section 2.3). Technically this is achieved by implementing several separately contacted sections in the monolithic cavity of LD. The cavity sections which are positively biased provide the optical gain while a negatively biased section behaves as a saturable electroabsorber. Under moderate negative bias applied to the absorber section, the laser exhibits passive mode-locking or Q-switching

operation. However, with further increasing negative bias, yielding shorter recovery time and larger absorption coefficient, a different emission regime occurs. At threshold of Q-switched lasing operation and under pulsed current pumping, the laser reveals features of SR-like emission. These features have been experimentally observed in multi-section GaAs, AlGaInAs and GaN QW lasers [86]–[89]. Unfortunately all experimental studies reported in the literature do not distinguish the first emission burst from the subsequent self-pulsations, which can be modulated with a Q-switching pulse envelope. Nevertheless a clear Rabi splitting was observed in the optical spectrum of multi-section LDs when these were expected to produce SR emission [86]. Although there were no reports on experimental or theoretical studies on RNGH instability in a multi-section laser diode, we believe that this subject will receive further attention in the future [45].

3.7. The role of carrier population and carrier coherence gratings

In Fig. 3.16 we study the effect of coherence grating on the gain spectrum (increment) for multimode instability by examining the highest gain frequency Ω_{\max} in Eq. (2.26) as a function of the pump rate p [45]. These numerical studies complement and confirm the outcomes of our analytical studies from Ref. [46].

As a reference, we show the frequency Ω_{\max} obtained by numerically solving the eigenproblem (2.26) with QCL parameters from Table 1 and coherence grating relaxation time $T_{2_g} \neq 0$ (solid blue curve) as well as the calculated Rabi frequency (3.2) (dashed blue curve) under the same operation conditions. These two reference curves are thus obtained in the presence of mode coupling via scattering on the coherence grating in addition to the coupling via carrier population grating.

The effect of coherence grating can be excluded from Eq. (2.26) by considering the limit $T_{2_g} \rightarrow 0$. We achieve this via reducing T_{2_g} by a factor of 10^{11} while maintaining the average decoherence rate ($T_{2_{eff}} \neq 0$) and the mode coupling via SHB-induced grating of the carrier distribution ($T_g \neq 0$). This represents very well the limit of $T_{2_g} \rightarrow 0$, when there is no mode coupling via scattering on the coherence grating [45], [46].

We find that the system (2.26) still reveals instability and this instability is caused by the SHB effect only. For the pump rates up to $p \sim 10$, the spectral shape of the instability increment $Re(\Lambda)$ is similar to the one depicted in Fig. 3.1. (Compare this shape with the warped instability gain curve at much higher pump rate of $p \sim 50-60$ in Fig. 2.1.) Thus the instability gain spectra do not indicate a change in the mechanism of multimode instability. In Fig. 3.16 we add the superscript “(SHB)” in order to distinguish this case and plot the frequency $\Omega_{\max}^{(SHB)}$ calculated numerically from Eq. (2.26) and $\Omega_{Rabi}^{(SHB)}$ from Eq. (3.2) for the case when T_{2_g} is reduced by a factor of 10^{11} (solid and dashed red curves, respectively) [45].

In Gordon et al. [39], the expression (3.3) was obtained for the highest increment frequency for the multimode instability caused by the SHB effect, that is in the case we have just discussed above. In Fig. 3.16 we denote this frequency as $\Omega_{SHB}^{[39]}$ (green curve) and plot it as a function of the pump rate using the parameters of QCL from Table 1.

The following conclusions can be made from comparison between different curves in Fig. 3.16:

- (i) In the presence of coherence grating ($T_{2_g} \neq 0$), the highest instability gain is at the offset frequency Ω_{\max} which is very close to the Rabi

frequency Ω_{Rabi} . Like the last one, Ω_{max}^2 exhibits a linear growth with the pump rate p (solid blue curve in Fig. 3.16). This behavior is a signature of a multimode RNGH-like instability (see the Introduction).

- (ii) Without coherence grating ($T_{2_g} \rightarrow 0$), both the frequency Ω_{max} and the Rabi frequency reduce to $\Omega_{max}^{(SHB)}$ and $\Omega_{Rabi}^{(SHB)}$, respectively (solid and dashed red curves). However, $[\Omega_{max}^{(SHB)}]^2$ does not follow anymore the linear growth of $[\Omega_{Rabi}^{(SHB)}]^2$ and slightly deviates from the Rabi oscillation frequency. Thus even at the pump rate as high as $p=5$ times above the lasing threshold, $\Omega_{max}^{(SHB)}$ is only by a factor of 1.1 lower than $\Omega_{Rabi}^{(SHB)}$. Therefore we cannot attribute it to a markedly different behavior than the one observed in the presence of additional mode scattering on the coherence grating. Inclusion of the coherence grating just slightly increases the highest instability frequency in the 4×4 matrix in Eq. (2.26).
- (iii) The frequency $\Omega_{SHB}^{[39]}$ [Eq. (3.3)] obtained in [39] for the case without coherence grating, that is for case we discussed in (ii), is significantly lower than our frequency $\Omega_{max}^{(SHB)}$ and the Rabi flopping frequency $\Omega_{Rabi}^{(SHB)}$. As a consequence of such low frequency it was attributed to a multimode instability of a different kind and labeled as a multimode instability caused by the SHB effect. In fact the original system of the coupled mode equations in [39] contains a set of errors. Its adiabatic approximation for slowly varying medium, polarization does not recover the well-known Class-B laser model (See a discussion to our Eqs. (2.7)-(2.11) and the Appendix B). As a consequence of these errors, the frequency $\Omega_{SHB}^{[39]} \ll \Omega_{Rabi}^{(SHB)}$, which is not the case in our model [45].

In [46] we analyze this problem analytically and arrive to the same conclusions (the results of [46] will be presented in detail in Chapter 4). In particular, we obtain a closed form expression for the second threshold that indicates that coherence grating just slightly reduces the second threshold. The main source for low-threshold RNGH instability in QCLs is SHB and a set of the relaxation and diffusion time constants that result in T_g being comparable to T_1 .

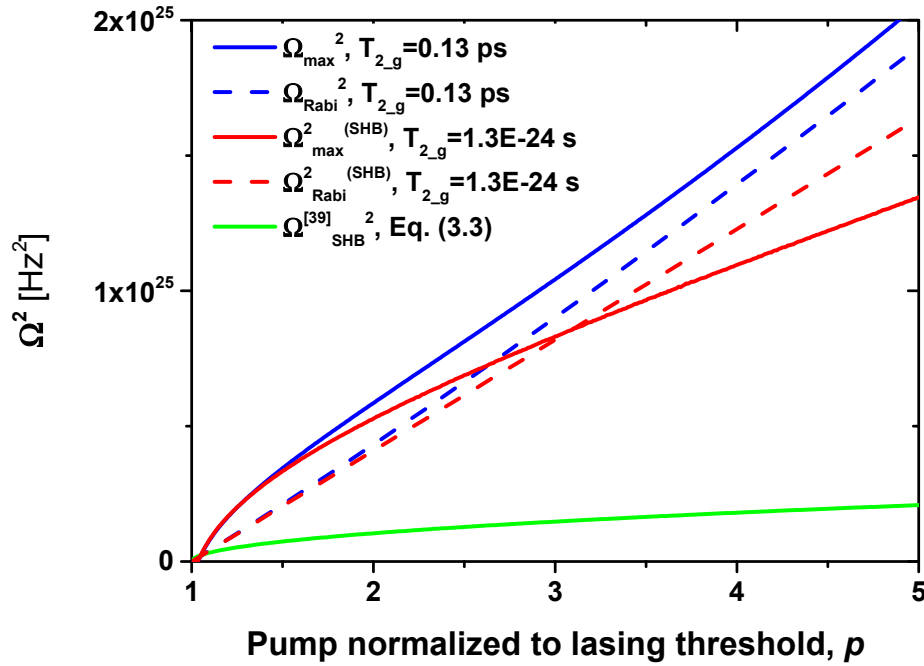


Fig. 3.16. We plot the squares of the following frequencies as a function of the pump rate, using parameters of QCL from Table 1 ($T_g=0.927$ ps, $T_{2_eff}=0.14$ ps and $T_{2_g}=0.13$ ps unless stated otherwise): the highest instability gain frequency Ω_{\max} calculated numerically from the eigenproblem (2.26) ($T_{2_g} \neq 0$, solid blue curve) and corresponding Rabi oscillations frequency (3.2) (dashed blue curve); the frequency $\Omega_{\max}^{(SHB)}$ (solid red curve) and the Rabi frequency $\Omega_{\text{Rabi}}^{(SHB)}$ (dashed red curve) obtained without coherence grating (T_{2_g} is reduced by a factor of 10^{11}); and finally the frequency $\Omega_{\text{SHB}}^{[39]}$ calculated from Eq. (3.3) (green curve). © 2017 IEEE. Reprinted, with permission, from [45].

The coherence grating has a much stronger impact on the eigensolutions of the upper 5×5 block in Eq. (2.26). In Fig. 3.17 we plot the spectra of the Lyapunov exponents with the largest real parts in the 4×4 (red curves) and 5×5 (blue curves) matrices in (2.26) for the two pump rates $p=9$ [Fig. 3.17(a)] and $p=10$ [Fig. 3.17(b)]. Once again we compare cases when the coherence grating is present ($T_{2_g} \neq 0$, solid curves) and when it is absent ($T_{2_g} \rightarrow 0$, dashed curves). We observe that without coherence grating (when $T_{2_g} \rightarrow 0$) the increment of instability in the 4×4 matrix (red curves) increases and its spectrum shifts to lower frequencies. It shows similar behavior at the two considered pump rates ($p=9$ and $p=10$). The behavior of the instability increment in the 5×5 matrix has much in common with the one in 4×4 matrix but the increment values are shifted down on the vertical axis in Fig. 3.17 toward negative Lyapunov exponents. Only without coherence grating ($T_{2_g} \rightarrow 0$, while $T_{2_{eff}}$ is unchanged), the increment becomes positive and RNGH instability occurs at $p=10$ (see the behavior of the dashed blue curve in the inset of Fig. 3.17(b)). Note that the RNGH instability does not occur at $p=9$ because $T_{2_{eff}} / T_1 \neq 0$ [30]. Once the coherence grating is present ($T_{2_g} \neq 0$), the RNGH instability threshold in 5×5 matrix increases by several times, to around $p=60$ in particular case (See Fig. 2.1) [45].

In this way it remains only one pleasurable explanation for the low second threshold observed in experiments with QCLs. Namely, we conclude that it is related with the instability arising from the 4×4 matrix block in Eq. (2.26) due to a combined effect of the carrier population and carrier coherence gratings.

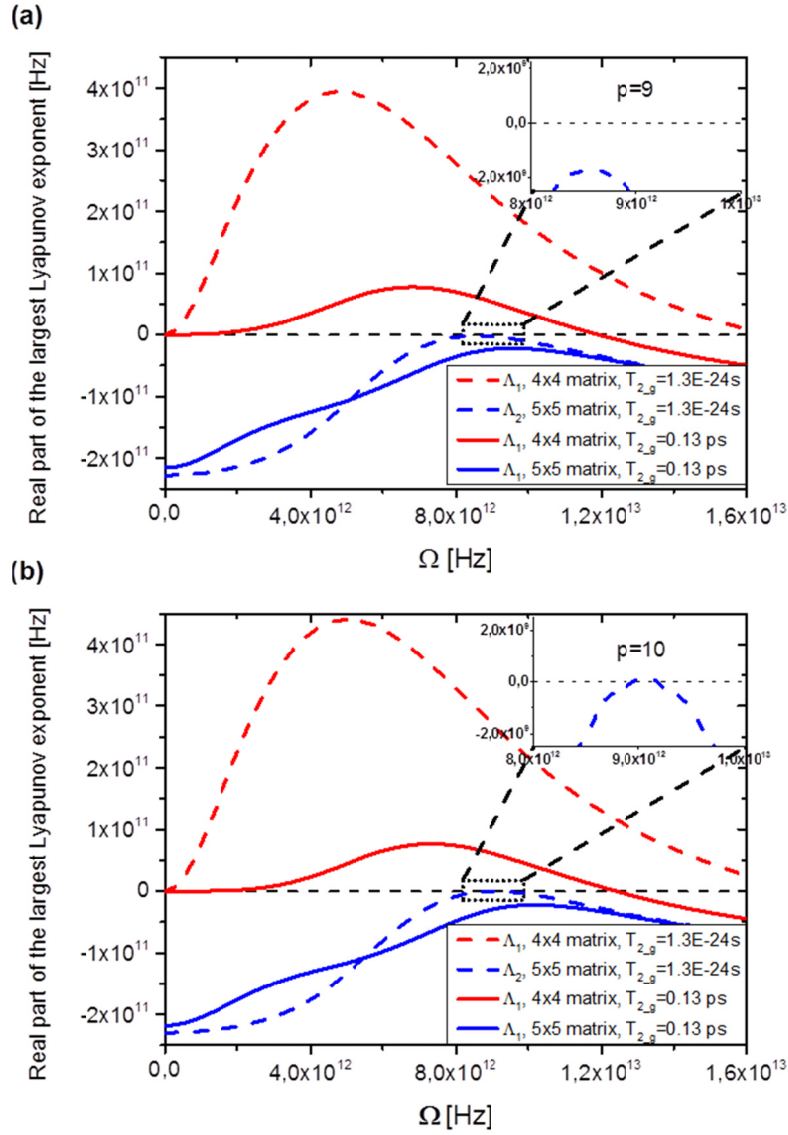


Fig. 3.17. Spectra of instability increments (largest real parts of the Lyapunov exponents) of the two matrix blocks of 4×4 (red curves) and 5×5 (blue curves) sizes for QCL with parameters from Table 1. The pump rate excess above threshold is $p=9$ (a) and $p=10$ (b) [© 2017 IEEE. Reprinted, with permission, from [45]]. The solid curves stand for the case considered in this paper when we include the coherence grating effects ($T_{2,g} = 0.13 ps$), while the dashed curves represent the case when the coherence grating relaxation time $T_{2,g}$ is reduced by a factor of 10^{11} , suppressing all effects caused by the coherence grating. The insets show zooms to the highest RNGH instability increments in the 5×5 matrix block when $T_{2,g} \rightarrow 0$ (no coherence grating effects).

4. Analytical expression for RNGH instability threshold in QCLs

In Chapter 3 we have analyzed conditions for multimode RNGH instability in a Fabry-Pérot cavity laser and proposed an alternative mechanism responsible for low RNGH instability threshold in QCLs. It also favors the RNGH instability threshold lowering by the SHB effect but does not require a saturable absorber. More specifically, we have shown that a combined effect of the carrier coherence grating, carrier population grating and relaxation processes due to carrier diffusion leads to the onset of multimode instabilities at Rabi flopping frequency. We consider such spectral behavior as an evidence of RNGH instability. Our approach to calculate the RNGH threshold has shown a convincing agreement with the available literature data and with the results of numerical simulations [45], [46], [58]. From a practical point of view, this can be converted into a useful engineering tool enabling to examine particular QCL design and predict its dynamic behavior or to tailor QCL design for a specific application. In this Chapter we obtain a simple closed-form analytical expression for the RNGH instability threshold in a QCL with monolithic FP cavity. The main result of the section is summarized by Eq. (4.9). Technically, it is obtained by using the second-order biorthogonal perturbation theory applied to the Lyapunov stability analysis of the single-mode lasing regime in a QCL [46], [94].

4.1. Second-order biorthogonal perturbation theory

For the reason we will explain later, we split the 4×4 matrix from Eq. (2.26) into two matrices $M^{(0)}$ and $M^{(1)}$ [46]:

$$\|M\| = \|M^{(0)}\| + \|M^{(1)}\| =$$

$$= \begin{bmatrix} -\frac{1}{T_{2_eff}} & -\frac{(2\nu_0-1)}{2T_{2_eff}} & 0 & 0 \\ -\frac{c}{n_g}l_0 & -\frac{c}{2n_g}l_0 - i\Omega & 0 & 0 \\ 0 & 0 & -\frac{1}{T_g} & 2E \\ 0 & 0 & -\frac{E}{2} & -\frac{1}{T_{2_g}} \end{bmatrix} + \begin{bmatrix} 0 & 0 & \frac{E}{2} & 0 \\ 0 & 0 & 0 & 0 \\ -2E & E \left[1 + (\nu_0 - 1) \frac{T_{2_g}}{T_{2_eff}} \right] & 0 & 0 \\ 0 & -\frac{(\nu_0 - 1)}{2T_{2_eff}} & 0 & 0 \end{bmatrix}$$

(4.1)

where we omit the subscript “ 4×4 ” because all matrices that will be discussed from now on will be of the 4×4 size (the remaining 5×5 block exhibits only stable solutions in the range of pump rates that are used in practice as we have shown in Sections 2.3 and 3.7).

At first glance, it is quite straightforward to solve the eigenproblem of the matrix from Eq. (4.1) and to find an analytic expression for the pump rate p_{th2} that fulfills *the RNGH instability threshold condition* (3.1) $[|\Omega_{\max}^{(th2)}| / 2\pi = c / 2Ln_g]$ for the spectrum of the positive Lyapunov exponent. However, the characteristic equation for the Lyapunov exponent is of the fourth order. Therefore we use a perturbation-theory approach. Since the matrix in Eq. (4.1) is not Hermitian, its eigenvectors are not orthogonal. For that reason we use the second-order biorthogonal perturbation theory [95], [96] and split the linear stability matrix into the zero-order approximation $M^{(0)}$ and perturbation $M^{(1)}$ matrices, as indicated in Eq. (4.1). An example of the

eigenvalue spectra of the initial matrix M (solid black curves) and its zero-order approximation $M^{(0)}$ (red dashed curves) for a QCL pumped at $p=1.5$ times above the lasing threshold is depicted in Fig. 4.1 [46].

The eigenvalue with the largest real part Λ_{max} is associated with the upper 2×2 block in $M^{(0)}$, which is independent of Ω_{Rabi} . In the zero order approximation, the increment $\text{Re}(\Lambda_{max})$ just barely increases with the pump rate p due to the SHB effect accounted for in the parameter ν_0 given by Eq. (2.14) in Section 2.3:

$$\Lambda_{max}^{(0)} = -\frac{1}{2T_{2_eff}} - \frac{1}{4\tau} - i\frac{\Omega}{2} + \frac{1}{2} \sqrt{\left(\frac{1}{T_{2_eff}} + \frac{1}{2\tau} + i\Omega\right)^2 - \frac{4i\Omega}{T_{2_eff}} + 4\frac{\nu_0 - 1}{T_{2_eff}\tau}}, \quad (4.2)$$

where $\tau = n_g / cl_0$ is the photon lifetime in the cavity. Note that $\Lambda_{max}^{(0)} = 0$ at the lasing threshold ($p=1$) and zero detuning from the main lasing mode ($\Omega = 0$). The second eigenvalue originating from the upper 2×2 block in $M^{(0)}$ has the largest negative real part, of $\sim \Lambda_{max}^{(0)} - 1/T_{2_eff} - 1/2\tau$ (see Fig. 4.1). In contrast to this behavior [See Eq. (4.2)], the two eigenvalues originating from the lower 2×2 block in $M^{(0)}$ are independent of the spectral detuning Ω but exhibit splitting that varies with Ω_{Rabi} . At the lasing threshold ($p=1$) the splitting is of $1/T_{2_g} - 1/T_g$ and decreases with increasing Ω_{Rabi} (Note that $\Omega_{Rabi}^2 \ll T_{2_eff}^{-2}, T_{2_g}^{-2}$). It can be seen from the example in Fig. 4.1 plotted for $p=1.5$, that the eigenvalues of the matrices M and $M^{(0)}$ are close to each other as compare to the splitting [46].

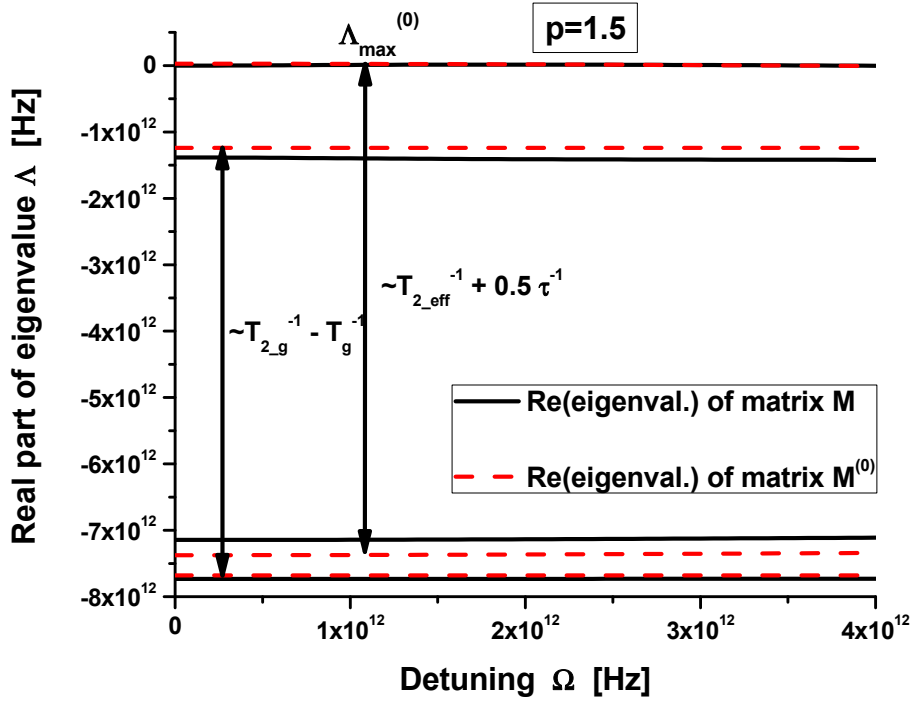


Fig. 4.1. Real part of eigenvalues of matrices M and $M^{(0)}$ from Eq. (4.1) for QCL with the cavity length $L = 4$ mm at pump rate $p=1.5$ times the lasing threshold. The red dashed curves show the real part of the eigenvalues of matrix $M^{(0)}$ and the black solid curves represent real part of eigenvalues of matrix M . The parameters used in simulations are listed in the 1st column in Table 1. © 2016 Optical Society of America. Reprinted, with permission, from [46].

The perturbation matrix $M^{(1)}$ has no diagonal elements. Therefore the first-order correction terms to the eigenvalues of $M^{(0)}$ vanish. Hence we apply the second order of biorthogonal perturbative expansion (see Appendix D for details) in Eq. (4.1) [46]:

$$\Lambda_i = \Lambda_i^{(0)} + \frac{\langle U_i^{(0)} | M^{(1)} | V_i^{(0)} \rangle}{\langle U_i^{(0)} | V_i^{(0)} \rangle} + \sum_{\substack{m=1, \\ m \neq i}}^4 \frac{\langle U_m^{(0)} | M^{(1)} | V_i^{(0)} \rangle \langle U_i^{(0)} | M^{(1)} | V_m^{(0)} \rangle}{(\Lambda_i^{(0)} - \Lambda_m^{(0)}) \langle U_m^{(0)} | V_m^{(0)} \rangle \langle U_i^{(0)} | V_i^{(0)} \rangle} \quad (4.3)$$

which provides a realistic approximation for the spectrum of RNGH instability gain $\text{Re}(\Lambda_{\max})$ in the vicinity of its maxima at $\Omega \sim \pm\Omega_{Rabi}$ (see Fig. 4.2, which we will discuss below). In Eq. (4.3), the diagonal term due to the first-order correction vanishes while the second-order correction terms are of the order of $\Omega_{Rabi}^2 T_{2_eff}$, $\Omega_{Rabi}^2 T_{2_g}$ which is much smaller than the initial spectral splitting indicated in Fig. 4.1. This justifies our decomposition onto the zero-order approximation $M^{(0)}$ and perturbation $M^{(1)}$ matrices in Eq. (4.1). In (4.3), the index i varies from 1 to 4, Λ_i denotes the eigenvalues, $V_i^{(0)}$ and $U_i^{(0)}$ are the concomitant partners, that is, these are the eigenvectors associated with the eigenvalues $\Lambda_i^{(0)}$ and $\Lambda_i^{(0)*}$ of the matrix $M^{(0)}$ and its adjoint matrix $M^{(0)\dagger}$ respectively, (see also Appendix D) [46]. The vectors $V_i^{(0)}$ and $U_i^{(0)}$ are used as the biorthogonal basis in the expansion (4.3). After some algebra, we obtain the following approximate expression for the Lyapunov exponent with the largest real part:

$$\text{Re}(\Lambda_{\max}) = -\frac{1}{2\tau} + \frac{C_0(p)}{\Omega^2 + 1/T_{2_eff}^2} + \frac{C_1(p)}{\Omega^2 + A(p)^2} + \frac{C_2(p)}{\Omega^2 + 1/T_{2_eff}^2} + \frac{C_3(p)}{(\Omega^2 + 1/T_{2_eff}^2)^2} \quad (4.4)$$

where coefficients $C_i(p)$ and $A(p)$ are independent of the offset frequency Ω (they are shown in the Appendix E) [46]. The first two terms in Eq. (4.4) originate from $\Lambda_{\max}^{(0)}$ in Eq. (4.2). The last three terms are due to the second order of perturbative expansion. For all cases considered here, $\Omega_{Rabi}, A \ll 1/T_{2_eff}$ so as the zero order terms and the two last terms in Eq. (4.4) vary slowly in the vicinity of the RNGH gain maxima at $\Omega \sim \pm\Omega_{Rabi}$. Furthermore, since $C_0 \gg C_2$, $T_{2_eff}^2 C_3$, the spectral locations of the gain maxima [at $\partial \text{Re}(\Lambda_{\max})/\partial \Omega = 0$] are mostly defined by the second and third terms in Eq. (4.4), yielding

$$\Omega_{\max}^2 \approx T_{2_eff}^{-2} \sqrt{-C_1 / C_0 - A^2} \quad (4.5)$$

Using the expressions from Appendix E for parameters A and $-C_1 / C_0$, we finally obtain that the highest gain for multimode RNGH instability is at the following offset frequencies [46]:

$$\Omega_{\max}^2 \approx \Omega_{Rabi}^2 \sqrt{\frac{1}{2} \frac{T_{2_g}}{T_{2_eff}} \left(1 + \frac{2}{\Omega_{Rabi}^2 T_g T_{2_g}} \right) - \frac{1}{T_g^2}} \quad (4.6)$$

This expression is valid when $\Omega_{Rabi}^2 \ll T_{2_eff}^{-2}$ (or $p - \nu_0 \ll T_1 / T_{2_eff}$), that is true in all cases of practical interest considered here. The frequency Ω_{\max} in Eq. (4.6) monotonically increases with the pump rate (e.g. see Fig. 4.2). Using Eq. (3.2), we find a reciprocal relationship to Eq. (4.6):

$$p - \nu(p) = \frac{T_1 T_{2_eff}}{T_g T_{2_g}} \left[\sqrt{1 + 2 \frac{T_{2_g} T_{2_eff}}{T_g^2} (1 + T_g^2 \Omega_{\max}^2)^2} - 1 \right]. \quad (4.7)$$

In Appendix F we obtain a general solution of Eq. (4.7) with respect to p . It appears that the instability increment (4.4) is negative and multimode instability is impossible at very small pump rates, when $p < p_{\min}$, where

$$p_{\min} = 1 + \frac{T_{2_eff}}{T_{2_g}} + \left(\frac{T_1 T_{2_eff}}{T_g T_{2_g}} - \frac{T_g^2}{T_{2_g}^2} \right) \left[\sqrt{1 + 2 \frac{T_{2_g} T_{2_eff}}{T_g^2} - 1} \right] \quad (4.8)$$

is the pump excess at which $\Omega_{\max}^2 = 0$ in Eq. (4.7). For the pump rates above this value, the increment (4.4) is positive at the frequency (4.5) [see Fig. 3.1], which may lead to multimode instability. Finally to obtain the RNGH instability threshold p_{th2} , we substitute our condition (3.1) for the Ω_{\max} in Eq. (4.7) and we get [46]:

$$\begin{aligned}
p_{th2} &= 1 + \theta_{th2} \left(1 + \left[\frac{2T_1}{T_g} + \frac{T_{2-g}}{T_{2-eff}} \theta_{th2} \right]^{-1} \right), \\
\theta_{th2} &= \frac{T_1 T_{2-eff}}{T_g T_{2-g}} \left[\sqrt{1 + 2 \frac{T_{2-g} T_{2-eff}}{T_g^2} \left(1 + \frac{c^2 \pi^2 T_g^2}{L^2 n_g^2} \right)^2} - 1 \right]
\end{aligned} \tag{4.9}$$

The RNGH instability threshold reduces towards p_{\min} [Eq. (4.8)] with increasing cavity length L . The meaning of p_{\min} corresponds to the notion of the RNGH instability threshold in the original RNGH theory. Nevertheless, by no means Eq. (4.8) can be directly compared with the RNGH instability threshold for a unidirectional ring laser obtained in [30], [31] (see also discussion in Section 4.3). However, the shape of the multimode instability gain curve (4.4) can be assessed against the one in a unidirectional ring laser. For this purpose we provide an approximate expression for the maximum of increment (4.4) at the offset frequency (4.6), which we will use later [46]:

$$\text{Re}(\Lambda_{\max}) \Big|_{\Omega=\Omega_{\max}} = -\frac{1}{2\tau} \left(1 - \frac{3}{2} \frac{\Omega_{Rabi}^2 T_{2-eff}^2}{2} \right) + \frac{2\nu_0 - 1}{2\tau} \left[1 - \Omega_{\max}^2 T_{2-eff}^2 - \frac{T_{2-eff}^2}{T_g^2} \right]^2. \tag{4.10}$$

4.2. Validation of the analytic solution for the RNGH instability threshold

In Fig. 4.2 we compare the instability gain curves obtained from the analytic expression (4.4) (red curves) and by solving numerically the eigenvalue problem of the linear stability matrix (4.1) (black curves). The results are plotted as the round-trip gain $2\text{Re}(\Lambda)n_g L/c$ vs the offset frequency $\Omega/2\pi$. In this example we use a QCL with the cavity length of 4 mm and other parameters from the first column in Table 1. For the pump rate p from 1 to 2.5 times above the lasing threshold and in the large spectral range, our analytical

expression (4.4) is in reasonable agreement with the RNGH roundtrip gain obtained by solving numerically for the eigenvalues of the matrix M in Eq. (4.1) [46].

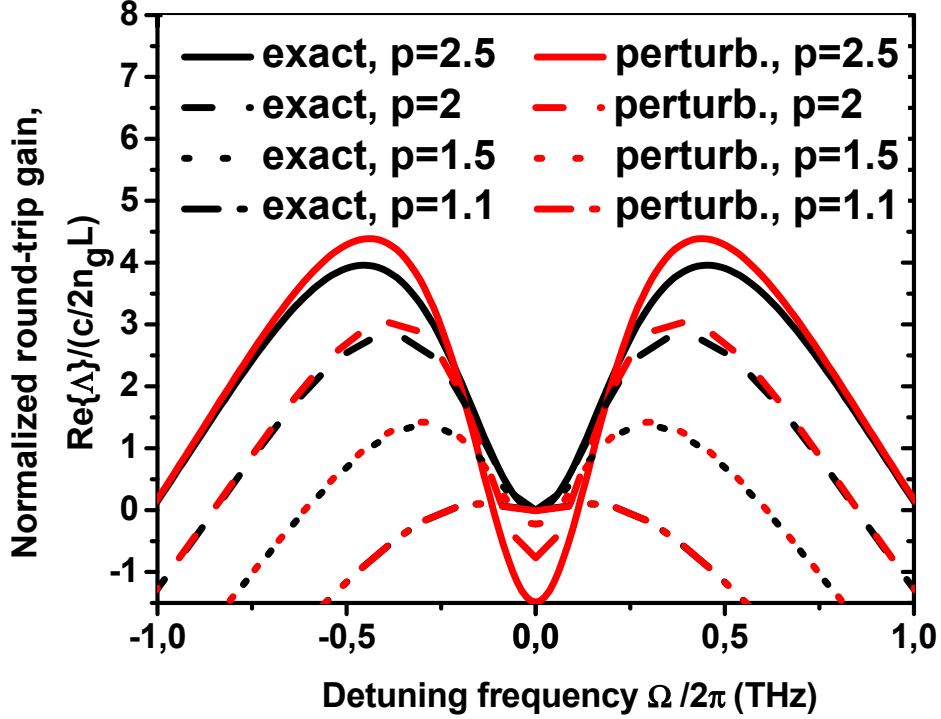


Fig. 4.2. The spectral behavior of the round-trip gain coefficient for multimode instabilities in QCL with the cavity length $L = 4$ mm (The cavity mode separation $c/2Ln_g = 11$ GHz) at different pump rates p in the range from 1 to 2.5 times above the lasing threshold. The red curves show the gain spectra obtained from the analytical expression (4.4) and the black curves are obtained by solving numerically the eigenproblem of the matrix (4.1). The parameters used in simulations are listed in the first column in Table 1. © 2016 Optical Society of America. Reprinted, with permission, from [46].

It is interesting to compare the instability gain curves for long -cavity QCL in Fig. 4.2 (the cavity mode separation is ~ 11 GHz) with the ones obtained in Fig. 3.1 for a QCL with the cavity length of $100 \mu\text{m}$ (the intermodal frequency is ~ 450 GHz). For concreteness we take the gain curves at $p=2.5$. Both gain

curves are peaked at the same offset frequency of $\Omega_{max} / 2\pi \sim 450 \text{ GHz}$. Our Eq. (4.6) also confirms that Ω_{max} is independent of the photon lifetime in the cavity.

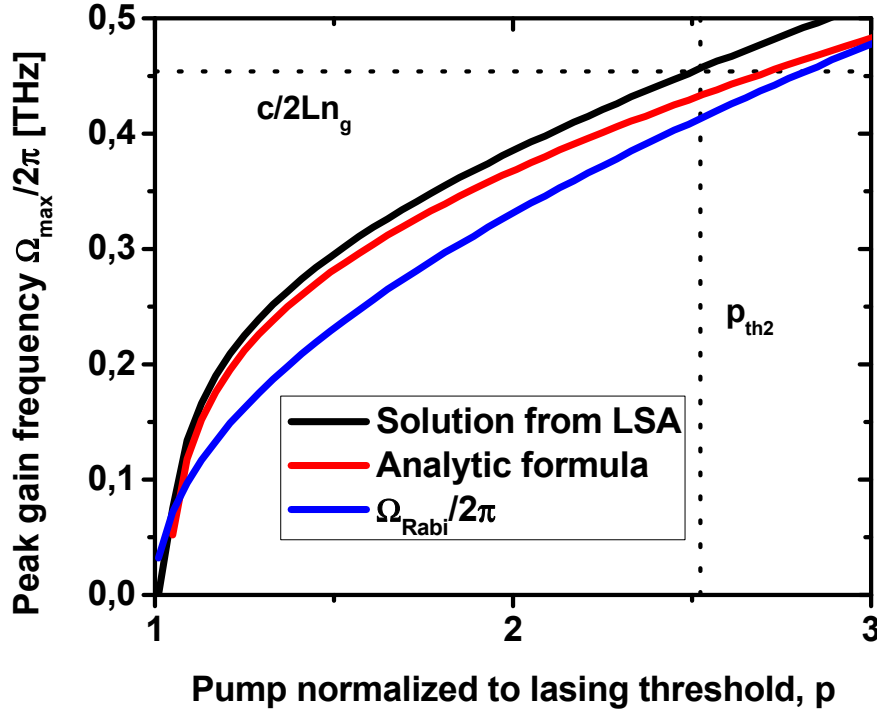


Fig. 4.3. Peak gain frequency of RNGH instability calculated numerically from our linear stability matrix (black curve) and from our analytic expression Eq. (4.5) (red curve) is plotted vs. pump normalized to lasing threshold p . It is shown in comparison with the behavior of Rabi oscillations $\Omega_{Rabi}/2\pi$ (blue curve). According to Eq. (3.1), the intersection between horizontal dotted line at $c/2Ln_g$ and the peak gain frequency defines the value of RNGH threshold (vertical dotted line) in case of the $100 \mu\text{m}$ long cavity. © 2016 Optical Society of America. Reprinted, with permission, from [46].

Fig. 4.3 provides a comparison between the frequency $\Omega_{max} / 2\pi$ obtained from the analytical expression (4.6) (red curve) and from the numerical solution of the eigenproblem of the matrix (4.1) (black curve). It follows that our analytical

expression for Ω_{max} is in reasonable agreement with the one obtained numerically. Note that the Ω_{max} frequency approaches the Rabi oscillation frequency Ω_{Rabi} at high p (blue curve) [45], [46].

In order to illustrate the RNGH instability threshold condition (3.1) we show in Fig. 4.3 a horizontal line at $\Omega/2\pi = c/2Ln_g$ for the cavity length of $L=100 \mu\text{m}$. Its crossing point with $\Omega_{max}/2\pi$ curve defines the RNGH instability threshold, which is indicated by a vertical line. Our analytic approach provides a realistic approximation for the RNGH threshold (the crossing point of the horizontal line with the red curve).

Table 2. Dynamic model parameters for QCL2 considered in this Section. All other parameters are the same as for the QCL in Table 1, first column.

Parameter	Name	QCL2 [39]
λ	Lasing wavelength	8 μm
T_1	Carrier lifetime	0.5 ps
T_2	Carrier dephasing time	67 fs
T_{2_eff}	Effective carrier dephasing time in the presence of diffusion	66 fs
T_g	Relaxation time of the carrier population grating	0.403 ps
T_{2_g}	Relaxation time of the coherence grating	62 fs

Fig. 4.4 shows variation of the RNGH threshold with the length of QCL cavity. (We plot the relative excess above the lasing threshold p_{th2-1} in logarithmic scale.) We consider two sets of QCL parameters: from Table 1, first column (QCL1) and Table 2 (QCL2). In both cases, our analytical expression (4.9) (curves) shows good agreement with the numerical solutions for the eigenvalues of the linear stability matrix (4.1) (points). Note that the RNGH

threshold behavior predicted in Fig. 4.4 is in agreement with the results of numerical simulations based on the TW model [45], [47] (see also Fig. 3.1) and with the numerous experimental reports indicating low RNGH threshold in QCLs with the cavity length of 2-4 mm [29], [39], [48].

Our small signal analysis is based on a truncated system of coupled-mode equations [45], [46], [58] and our analytical expressions are valid in the limited range of the pump rates, when $p - v_0 \ll T_1 / T_{2_eff}$. In the case of QCLs, we are practically limited to the range of $p < 3$.

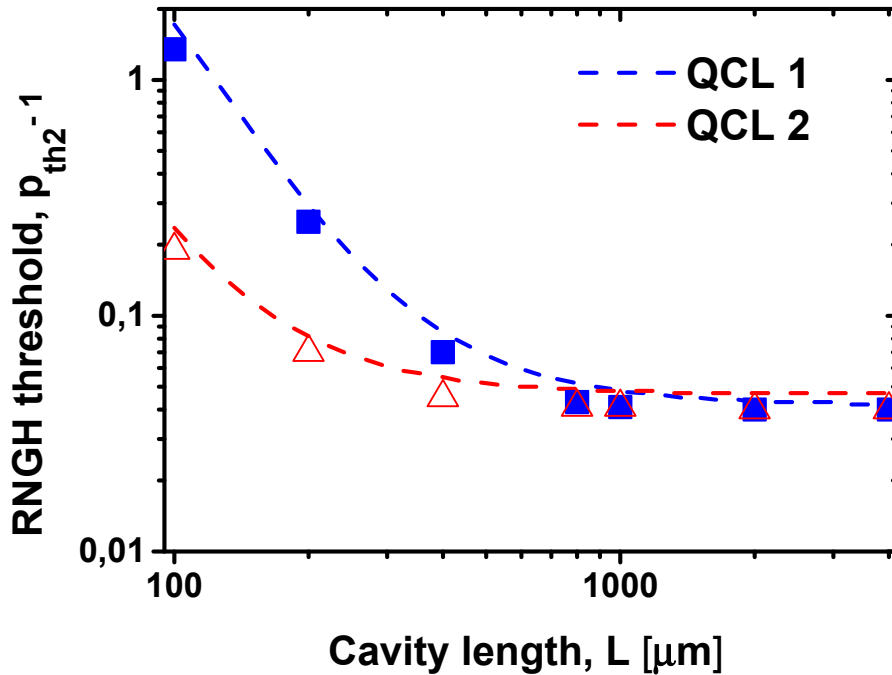


Fig. 4.4. RNGH instability threshold (represented as a relative pump excess above the lasing threshold p_{th2-1}) vs. cavity length. We compare p_{th2} calculated from our Eq. (4.9) (curves) and calculated by numerical solving of the eigenproblem of the matrix (4.1) (squares and triangles). The parameters for QCL 1 and QCL 2 are listed in Table 1. © 2016 Optical Society of America. Reprinted, with permission, from [46].

Expression (4.8) is approximately equal to p_{th2} when the cavity free spectral range (FSR) is much smaller than T_g^{-1} (e.g. in mm-length QCLs). For the case when $T_{2_g}T_{2_eff} \ll T_g^2$ the following approximation can be used [46]:

$$p_{th2} \approx p_{min} \approx 1 + \frac{T_{2_eff}^2}{T_g^2} \left[\frac{1}{2} + \frac{T_1}{T_g} \left(1 - \frac{T_{2_g}T_{2_eff}}{2T_g^2} \right) \right] \approx 1 + \frac{T_{2_eff}^2}{T_g^2} \left(\frac{1}{2} + \frac{T_1}{T_g} \right). \quad (4.11)$$

The expression (4.11) is very handy for clarification of the role of the SHB effect. For instance in MIR QCLs, the diffusion length of the electrons in the plane of active QWs is of $\sqrt{DT_1} \sim 0.1 \mu\text{m}$, which is much smaller than the wavelength. Therefore the induced population grating has a large contrast and lowers the 2nd threshold. Indeed, if we assume that $Dk^2 \ll T_2^{-1}, T_1^{-1}$ in Eq. (4.11) and thus neglect the diffusion, we find that the second threshold in QCLs is just above the lasing threshold $p_{th2}^{(QCL)} \rightarrow 1 + 3T_2^2/2T_1^2$ provided $T_2/T_1 \ll 1$.

For interband QW (or bulk) LDs operating in the VIS and NIR spectral ranges., an estimation of the typical carrier diffusion length yields the value of $\sqrt{DT_1} \sim 1 \mu\text{m}$ using the characteristic gain recovery time of $T_1 \sim 1$ ns and bimolecular diffusion coefficient of $D \sim 10$ cm²/s. The diffusion length exceeds the wavelength in the gain medium and hence the contrast of the induced population grating is low. Assuming in Eq. (4.11) that $Dk^2 \gg T_2^{-1}, T_1^{-1}$, we obtain $p_{th2}^{(LD)} \rightarrow 9 + 16T_1/T_g$, i.e. we partially recover the conclusion of Risken, Nummedal, Graham and Haken on the at least 9-fold pump excess above the lasing threshold required for the onset of multimode instability. However, in the LD case, it is even much higher because $T_1/T_g \gg 1$ in the second term. As a result of the shorter emission wavelengths and longer (bimolecular) diffusion lengths of the carriers, FP cavity QW LDs do not show RNGH

instability at experimentally achievable pumping currents [58], [74]¹. See also Section 3.6 and figures therein.

The mechanism of the RNGH instability switching from due to a change of the gain recovery time (see also Section 3.2) is illustrated in Fig. 4.5(a), where the behavior of the second threshold (4.8) is plotted in the range of typical carrier lifetimes for MIR QCLs [74], [97]. The diffusion coefficient used in Fig. 4.5(a) allows the formation of the population and coherence gratings and corresponds to QCL operating with equal voltage drops on all quantum cascade periods, within a stable part of I-V curve with positive differential resistance [74], [75]. Under these conditions, a sudden increase of the carrier lifetime T_1 (as a result of the lasing transition change) will cause a drop of p_{th2} , so that the QCL which was initially operating in the usual regime with emission of a few cavity modes will switch to broadband multimode RNGH self-pulsations [74].

The second mechanism of the RNGH instability switching due to the change of the contrast of the induced population grating is illustrated in Fig. 4.5(b) [74]. Vanishing of the population grating may occur in QCL operating at a bias higher than the one at a tunneling resonance, which would correspond to the unstable part of I-V curve with negative differential resistance if the voltage drops on all periods would be the same. However, instead of this, when a QCL is driven by a current source, the unstable part of I-V curve leads to a formation of electric field domains with non-uniform charge accumulation and depletion across multiple QCL periods [74]-[76].

¹ Note that these considerations do not apply to the case of quantum dot (QD) and quantum dash (QDash) laser diodes where the diffusion relaxation of the gratings along the cavity waveguide is prevented by the quantum confinement and the characteristic gain recovery time is on ps scale.

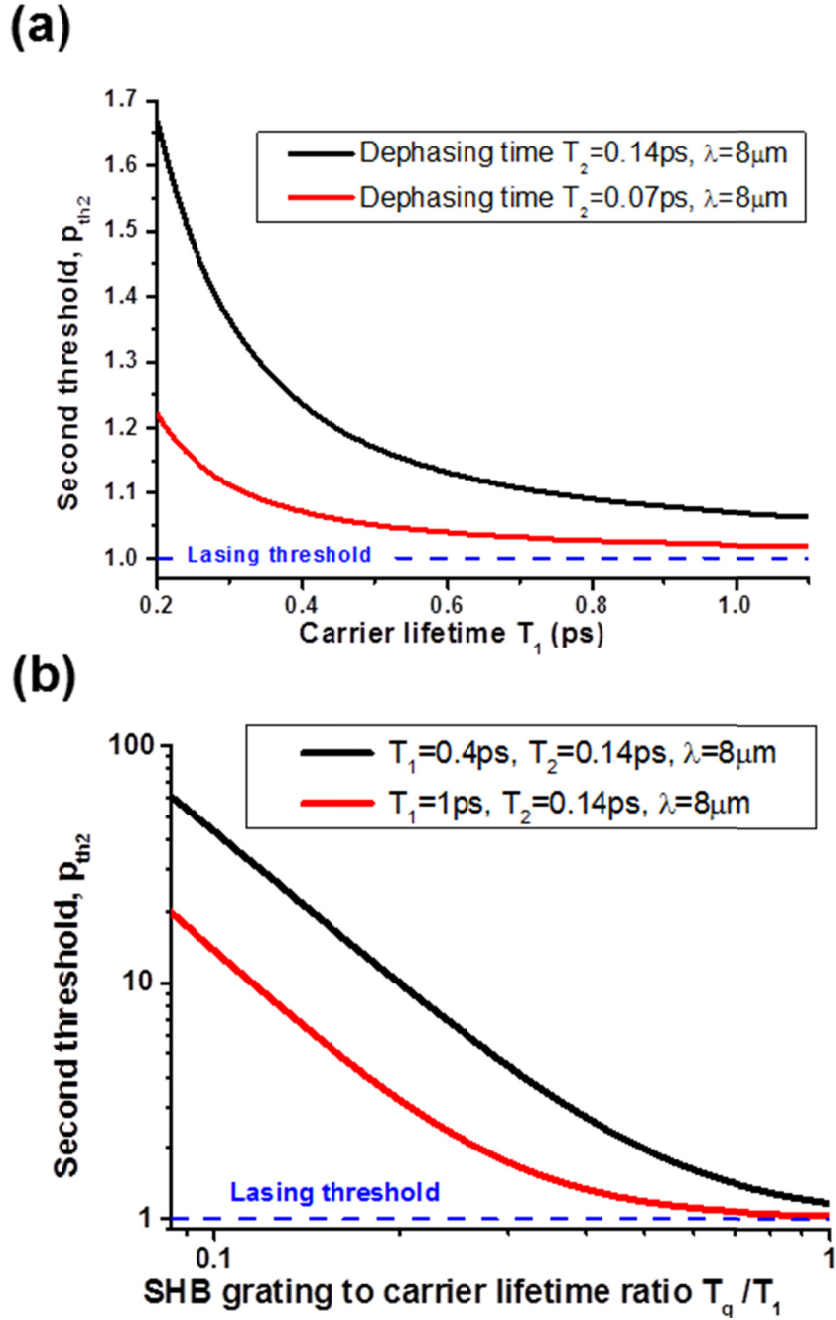


Fig. 4.5. (a): Normalized second threshold p_{th2} vs carrier relaxation time T_1 calculated for the carrier decoherence time T_2 of 70 fs (red curve) and 140 fs (black curve), diffusion coefficient $D=180$ cm²/s. (b): Normalized second threshold p_{th2} vs SHB grating relaxation time for population difference lifetime T_1 of 0.4 ps (black curve) and 1 ps (red curve), decoherence time $T_2=140$ fs. The horizontal dashed line indicates the lasing threshold given by Eq. (4.8). The emission wavelength is $\lambda=8$ μ m. Reprinted from [74].

In [74] authors elucidate that these inhomogeneities in the carrier distribution reduce the efficiency of the mode coupling through the induced carrier grating, the situation which is simulated in Fig. 4.5(b) by allowing the grating relaxation time T_g to decrease well below T_1 . The contrast reduction of the induced population grating leads to the increase of the second threshold to prohibitively high currents. Reference [74] reports on the experimental studies supporting both proposed mechanisms of RNGH instability switching in QCLs and explain it using a simple analytic expressions (4.8) and (4.11) [46].

4.3. Link to the original RNGH theory

We have shown in Section 2.3 that in the limit of $T_g, T_{2-g} \rightarrow 0$, that is when we exclude *both* carrier (SHB) and coherence gratings, our 9×9 linear stability matrix [Eq. (2.25)] reduces to a model for an unidirectional ring laser, like the one considered in [30], [31]. In this case, the submatrix corresponding to our 4×4 matrix (4.1) is always stable, while the other one originating from the 5×5 block exhibits the RNGH instability for $p \sim 10$ (for QCL in Table 1) or $p \sim 9$ (for LD), in agreement with the original RNGH theory [30], [31], [69]. Since our estimate for the RNGH threshold (4.9) originates from a different matrix block, by no means it may show a limiting transition to the original RNGH case of a unidirectional ring laser and recover the magic value for the RNGH instability threshold of $p=9$. However, the behavior of the multimode instability gain curve (4.4) can be assessed against the one in a ring laser. Below we provide approximate expressions for the maximum of instability increment (4.10) and compare it with the one obtained for RNGH instability in a unidirectional ring laser [69]. In both cases these maxima occur at respective frequencies Ω_{\max} quite close to the Rabi frequency Ω_{Rabi} .

First of all, we note that there is no effective threshold increase (2.14) in a unidirectional ring laser. Therefore to draw parallels between RNGH instability in a ring laser and the multimode instability in FP laser discussed here, we substitute $v_0=1$ in Eq. (4.10). Next, using that $\Omega_{Rabi} \ll 1/T_{2_eff}$, we find that the maximum increment for multimode instability in a FP cavity laser can be represented in the following form [46]:

$$\text{Re}(\Lambda_{\max}) \Big|_{\Omega=\Omega_{\max}} \approx \frac{3}{8\tau} \Omega_{Rabi}^2 T_{2_eff}^2 - \frac{1}{\tau} \Omega_{\max}^2 T_{2_eff}^2 \quad (4.12)$$

where the frequencies Ω_{Rabi} and Ω_{\max} are related by Eq. (4.6).

For the RNGH instability gain curve in a unidirectional ring laser, we use the expression from [69] (we refer to the Eq. (22.50) in there). Once again, using that, $\Omega_{Rabi} \ll 1/T_2$ we recast it into a simple form and obtain its peak value of

$$\text{Re}(\Lambda_{\max}^{(RNGH)}) \Big|_{\Omega=\Omega_{\max}^{(RNGH)}} \approx \frac{3}{2\tau} \Omega_{Rabi}^2 T_2^2 - \frac{1}{\tau} (\Omega_{\max}^{(RNGH)})^2 T_2^2, \quad (4.13)$$

where Ω_{Rabi} is given by Eq. (3.2) [with $v_0=1$]. However, the maximum increment is reached at a different frequency $\Omega_{\max}^{(RNGH)}$ [69] since there is no standing wave pattern in the ring cavity (see also Eq. (19) in [39]):

$$\Omega_{\max}^{(RNGH)} \approx \Omega_{Rabi} \sqrt[4]{2}, \quad \Omega_{Rabi} = \sqrt{\frac{p-1}{T_1 T_2}} \quad (4.14)$$

The two expressions, the Eq. (4.13) for RNGH instability in a unidirectional ring laser and our Eq. (4.12) for a FP cavity laser are surprisingly similar, indicating the same RNGH-like behavior in both cases [46].

For conclusion, in Chapter 4 and Appendix D, Appendix E and Appendix F we have derived an analytical expression for the RNGH instability threshold

in a quantum cascade laser with FP cavity. This simple analytical expression (4.9) and its approximation in case of long cavity QCLs (4.11) are versatile tools that can easily be applied in practical situations requiring analysis of QCL dynamic behavior and estimation of its RNGH instability threshold.

5. Regular self-pulsations in external cavity MIR Fabry-Pérot quantum cascade lasers

In this Chapter we will show that quantum cascade lasers operating in an external cavity (EC) configuration are capable of regular intensity self-pulsations (SP) at frequencies down to a practical range of ~ 100 GHz. Otherwise, in free-running QCLs, regular SPs due to multimode RNGH instability can occur only at Rabi flopping frequency on the THz scale (see Chapter 3). The very high oscillation frequencies in standalone QCLs are caused by the necessity to use very short cavities of ~ 100 μm lengths in order to preserve coherence over the round-trip time. Any attempt to increase the length of a standalone QCL cavity results in destruction of regular SPs and occurrence of broadband multimode quasi-periodic (chaotic) RNGH oscillations, also known as free-running (passive) QCL frequency combs. In contrast to these, we show that EC QCLs can achieve regular SPs with a reduced repetition frequency because (i) the delay time in the external cavity provides a memory effect preserving coherence of QCL pulse train and (ii) EC reduces the pulse repetition rate. We provide a detailed study on the effect of the EC length and pumping condition and find that SPs in EC QCLs should be excited with an initial kick, like the one put into practice for the worldwide popular Ti:S oscillators with passive Kerr-lens mode-locking [98].

5.1. Motivation for inclusion of an external cavity

In Section 3.4 we have shown a possibility of regular RNGH self-pulsations in standalone short-cavity QCLs ($\sim 100 \mu\text{m}$ long) provided that the cavity length is shorter than the coherence length. Note that the coherence time is of the order of $\sim 1 \text{ ps}$, which is of the same scale as the gain recovery time. Unfortunately, standalone QCLs with very short cavities would exhibit too high pulse repetition rates and have relatively high RNGH instability threshold [50], [98] (See also Section 3.4). Therefore, they are unsuitable for practical realization of ultrafast pulse production in QCLs. Otherwise, in the case of a few mm long QCLs with the cavity being much longer than the coherence length, different domains along the cavity start to produce mutually incoherent Rabi oscillations. Finally, because the gain medium does not provide “memory” to sustain regular pulsations, QCL emits intermittent pulse train consisting of quasi-periodic chaotic self-pulsations which are also of limited use for time-domain applications [45] (although the frequency combs can be stabilized and used for spectroscopy). Thus, in both cases of the short and long QCL cavities, the difficulties for practical use of RNGH self-pulsations in the time domain originate from the absence of the gain “memory effect” that can sustain low-frequency periodic regimes.

In this section, RNGH self-pulsations in external cavity (EC) QCL configuration are considered for the first time with an objective to reduce the frequency of self-pulsations. Because of otherwise tedious numerical simulations we limit the case study to a short $100 \mu\text{m}$ QCL chips.

The effect of optical feedback on QCL’s dynamics is yet to be explored since there are only few theoretical and experimental studies available in the literature indicating complex dynamics that could be of great interest in novel applications [99]–[104]. In particular, the theoretical studies [102], [103] predict

enhanced CW lasing stability for QCLs subjected to an optical feedback. Optical spectra measurements in [99] prove the existence of five distinct feedback regimes in MIR DFB QCL, which are similar to the five regimes identified in interband LDs [105].

Both MIR DFB QCL and FP QCL submitted to the optical feedback reveal five main regimes established for the LDs in function of the feedback strength and delay time [106] and labeled as Regimes I to V with increasing feedback strength [105]. At a weak optical feedback (Regime I), only the laser linewidth is affected by the phase of the optical feedback. Regime II is characterized by longitudinal mode hopping with the changing feedback delay time. In the Regime III the laser becomes stable and locks to the mode with minimum single-mode linewidth. Regime IV assumes further increased feedback strength resulting in dramatic broadening of the laser—spectrum, a phenomenon known as “coherence collapse.” With further increase in feedback strength, for which the laser facet usually needs to be AR coated, the LD enters Regime V: a stationary operation on external cavity mode [107].

It was proven that DFB QCL has an increased stability of CW lasing regime as compared to their LDs counterparts when they are subjected to an external optical feedback. Thus MIR DFB QCLs exhibit unstable Regime IV only in a narrow region of the feedback strengths, which however broadens with reducing external cavity length [99]. Although it was not possible to investigate this regime experimentally, the authors in [99] evoke a possibility of an unstable regime in the limiting case of ultra-short EC. Indeed, recently published work by the same group provides an experimental evidence of low-frequency ($\ll 1$ GHz) self-pulsations observed close to the lasing threshold [100], [108]. With increasing optical feedback strength, QCL output power bifurcates to periodic regimes at the EC frequency and then to a chaos, thus exhibiting the class A laser dynamics. There is also a recent theoretical study

which analyzes the conditions for a Hopf bifurcation destabilizing the CW output of the QCL in the limit of large delay times of the optical feedback [101].

However, none of these studies on QCLs with optical feedback or in the EC configuration has considered the coherence effects leading to multimode RNGH instabilities observed in standalone FP QCLs. Unlike the previous studies we account for the possibility of ultrafast coherent phenomena in the gain medium of QCL [98]. Also, in contrast to the previous studies, our EC QCL model system is a configuration with very strong optical feedback, in which one would expect to observe the Regime V.

5.2. Model system

We focus our study on external cavity quantum cascade lasers (EC QCLs) which are different from QCLs subjected to the optical feedback (see Fig. 5.1). The behavior of EC QCL is analyzed as a function of the EC length and pump rate, assuming that QCL gain chip is only 100 μm long.

In our model system, the front facet of the QCL chip facing the external cavity reflector is not reflecting at all, thus having an ideal anti-reflection (AR) coating. For the sake of simplicity, the back facet is assumed to be left uncoated ($R=27\%$). The cavity is closed by the output coupling mirror of the same reflectivity ($R=27\%$) to allow direct comparison between EC QCL and FP cavity QCL with natural reflectivity of both facets (the lasing threshold currents are the same in the two cases). The cold cavity modes are entirely defined by the two end mirrors. Suppression of reflections at the internal facet is crucial for our concept because we wish to utilize the external cavity as a delay line to provide a “memory” effect to the system [98].

Our model system is very different from a QCL which has non-vanishing reflectivity on the front facet and is subjected to the optical feedback, such as those considered in [99]–[103]. In the latter case, two distinct regions, the QCL chip and the free-space propagation region in EC, behave as two coupled cavities. This unwanted interaction would otherwise lead to strongly but slowly fluctuating intensities and mode hopping [109]. We exclude the possibility of such relatively slow dynamic regime, which is different from RNGH self-pulsations, by assuming a perfectly AR coated chip facet.

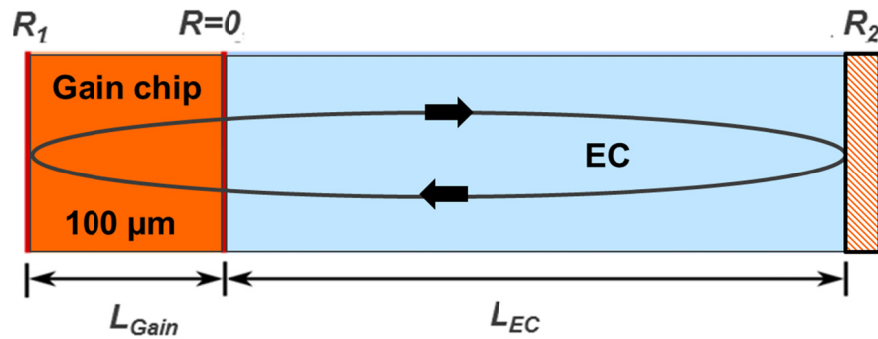


Fig. 5.1. Sketch of the EC configuration used in our modeling. Note that the back chip facet is AR coated and that we account for ultrafast coherent phenomena. From [98].

Parameters of FP QCLs used in numerical simulations are listed in column 1 of Table 1 in Section 2.1. We use again a semiclassical travelling wave (TW) rate equation model described in Refs. [45], [47] (see Sections 2.2 and 2.3) and adapt it for the case of external cavity configuration. Two different sections of the cavity are considered: one section provides description for the pulse propagation and amplification in the gain chip, the other describes pulse propagation in external cavity without interaction with the active medium [98], [110].

5.3. Numerical results for 100 μm chip

5.3.1. Standalone QCL

In this subsection we consider again a standalone FP QCL chip with a very short cavity ($L_{cav}=0.1$ mm) so as the cavity round-trip time $T_{cav}=2.2$ ps is comparable to the gain recovery time (see Section 3.4). At a pump rate above the instability threshold, e.g. at $p=3$, numerical simulations utilizing TW model reveal excitation of the self-pulsation within first 8 ps (~ 4 cavity round-trips) after the beginning of simulations with zero initial field condition. After 30 ps (~ 14 cavity round-trips), we observe a transit to a steady regime of regular sine-wave self-pulsations with FWHM pulsewidth of 0.6 ps [45]. The period of sine-wave is close to the cavity round-trip time of 2.2 ps, while the optical field and polarization of the gain medium change the sign at each passage in the cavity (a half of the sine-wave period). Consequently, the intensity pulses follow at 0.9 THz repetition rate.

First, we analyze the behavior of such standalone QCL with *increasing* pump current $p=I/I_{th}$. After each small change of p we reset the field amplitude to zero initial condition and let the QCL system to develop self-pulsations. Next, we consider the same behavior but with adiabatically *decreasing* pump current p in small steps of $\delta p=0.05$, such that QCL can reach a steady regime. For each p value, we perform numerical simulations over 50 cavity round-trips and use only the last 25 periods to analyze QCL dynamics after all transients. Figure 5.2(a) and Fig. 5.2(b) show the corresponding bifurcation diagrams of the extreme values (maxima and minima) in the output power waveform P_{out} . (More details about plotting such bifurcation diagrams can be found in [111]). The red (blue) circles indicate global and local maxima (minima). The largest values indicate peak power variation while zero values in the output power waveform are due to the change of the field sign [49], [98].

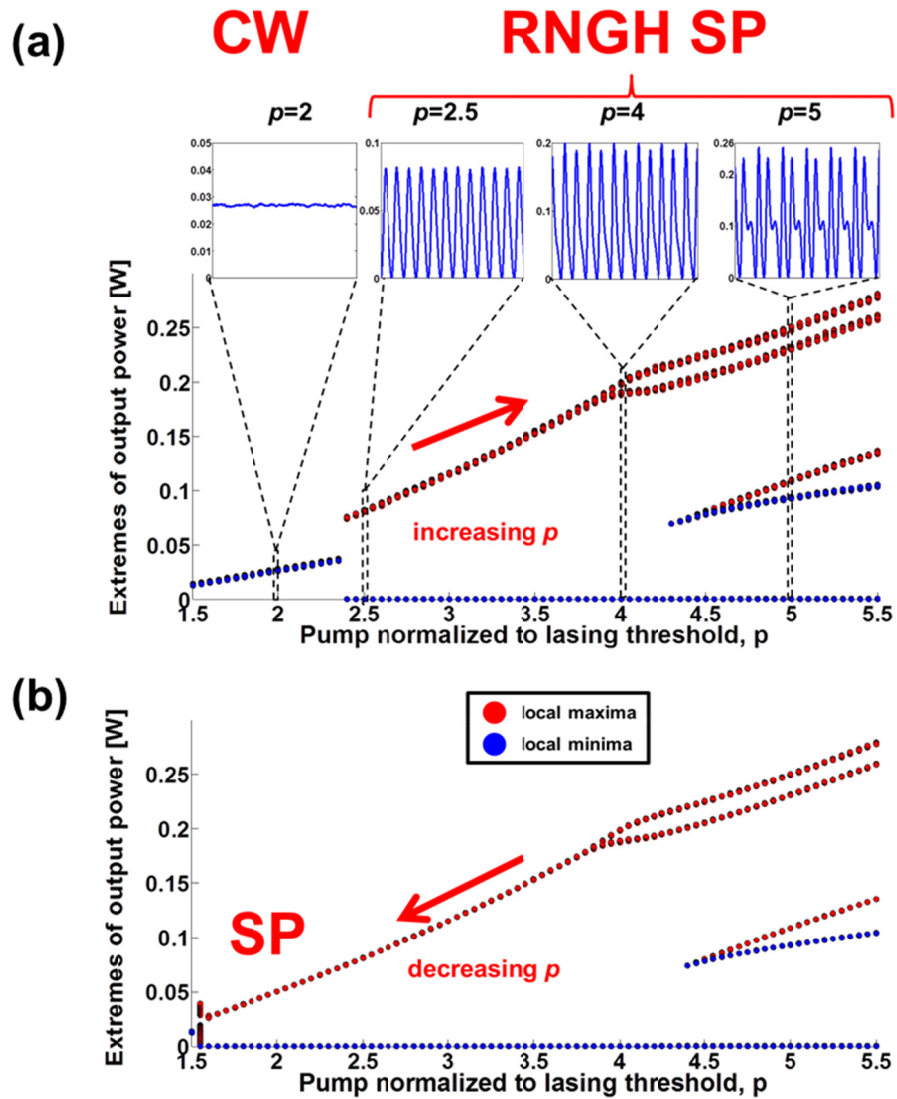


Fig. 5.2. Results of numerical simulations with TW model for monolithic QCL of the length 100 μm and normalized pump current $p=I/I_{th}$ changing in steps of $\delta p=0.05$. The total number of cavity round-trips per step is 50, out of which the initial 25 periods with transients are removed. (a) Bifurcation diagram of extreme values in the output power waveform (red circles for P_{\max} , blue for P_{\min}) when increasing p , showing only segment between $p=1.5$ and $p=5.5$. Insets show P_{out} waveform for 4 characteristic p values. (b) Bifurcation diagram for decreasing case; compare with (a) to see bistability between $p=1.55$ and $p=2.4$.

In the first case shown in Fig. 5.2(a), as expected for p increasing above the second threshold ($p_{th2}=2.4$), QCL shows self-starting oscillatory behavior,

while below it, QCL exhibits only the onset of CW emission (the insets in Fig. 5.2(a) show the output waveforms obtained for different pump rates). Surprisingly, in the second case depicted in Fig. 5.2(b), for the pump rate adiabatically decreasing below the instability threshold ($p_{th2}=2.4$), the self-sustained oscillations continue even below p_{th2} . However, if we “restart” the simulations at $p < p_{th2}$ and zero initial field in the cavity, the output waveform reveals CW lasing regime as opposed to the self-starting self-pulsations. Thus, for decreasing p we notice a hysteresis, indicating bistable operation (SP/CW) in the region between $p=1.55$ and 2.4 [compare Fig. 5.2(a) and Fig. 5.2(b)]. For p below 1.55 , only CW regime is observed in both cases. This indicates that SP in short-cavity QCL can be excited with an initial “kick,” much like in famous Kerr-lens mode-locked Ti:S lasers. The hysteresis can be attributed to the minimum initial pulse area of the “kick” [72], [112] required for the pulse energy growth on a cavity round-trip [45], [46].

With increasing p , we observe period doubling (at $p=4$) associated with distortion of harmonic SPs. To illustrate this change in the output waveform, we resolve QCL dynamics on the fast (within one cavity round-trip) and slow time scales (envelope change with p on multiple cavity round-trips). In Fig. 5.3(a) we show such contour plot representing the evolution of the output power waveform for p decreasing from very high initial pump rates. For p between 10 and 7.8 , the period of SP in the output power waveform is equal to the half of the cavity round-trip time. Then between $p=7.8$ and 4 , the period doubling occurs (the period of SP is equal to the round-trip time). Below $p=4$, the period of SP is reduced back and once again equal to the half of the cavity round-trip. In Fig. 5.3(b) we calculate the normalized recurrence period density entropy (RPDE) [113], by applying a so-called time-delay embedding [114] (see Appendix G). The entropy value of 0 corresponds to a perfectly periodic signal, while the value of 1 indicates a chaos. In this way normalized

entropy provides a clue about the character of the self-pulsations, whether they are periodic or quasi-periodic (chaotic).

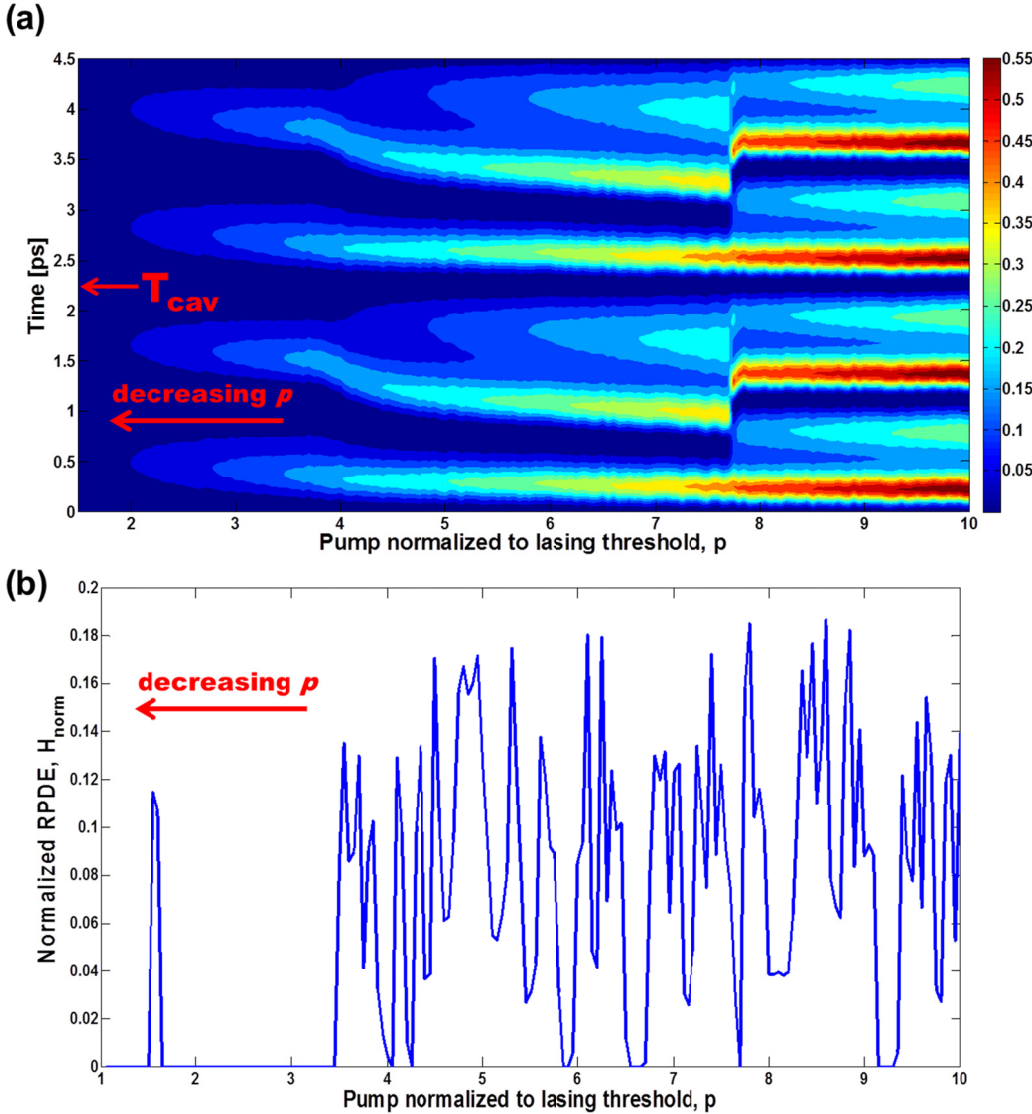


Fig. 5.3 (a) Contour plot of P_{out} distribution when decreasing p , during time equal to 2 cavity round-trips (short time scale, y-axis) for different p (long time scale, x-axis). (b) Behavior of H_{norm} -normalized Recurrence Period Density Entropy (RPDE) [113] with decreasing p . The following time-embedding parameters are used: embedding dimension $m=4$, embedding delay $\tau=10$, embedding ball radius $r=0.003$. For more details about meaning of these parameters and how to choose them please see [113], [114].

For a standalone short cavity QCL chip in Fig. 5.3(b), the RPDE entropy oscillates nearby 0 attesting for a perfectly periodic waveforms even at high pump rates, when the output waveform reveals a strong anharmonicity. The spike on the RPDE curve at the lowest p side of the SP/CW hysteresis loop can be attributed to the loss of stability of the SP regime and consequently to a higher sensitivity of the waveform to polarization noise, which is continuously introduced in the model system [45], [98].

In the considered example of a standalone short-cavity QCL, the “memory” effect between the subsequent cavity round-trips persists in the active region, yielding a regular pulse train. However, the pulse repetition frequency is too high for any practical application (see Section 5.1). In the following sections we analyze a possibility of reduction of the self-pulsation frequency by using an external cavity.

5.3.2. QCL in \sim mm long external cavity

We now consider QCL gain chip of the same length $L=0.1$ mm, but in the 0.9 mm long external cavity. The overall cavity round-trip time T_{cav} is of 8.2 ps.

In general, an increase of the second threshold is observed in the EC configuration. We attribute this to a reduced effect of SHB and coherence gratings because of the fractional cavity filling with the gain medium. Our numerical simulations attest that, in contrast to the standalone chip considered previously, excitation of SP in the EC configuration requires a stronger initial “kick” to switch from CW to SP behavior. In the case of 0.9 mm long external cavity QCL, the self-starting self-pulsations with zero initial field condition in the numerical simulations occur with certainty for normalized pump rate $p=4.3$. This conclusion is drawn on the basis of 80 repeated realizations, along the lines of approach discussed in Section 3.1 and Refs. [45], [46]. Fig. 5.4 shows an example of the field amplitude, optical and RF power spectra as well

as the 2nd order IAC at $p=4.3$. The dynamic behavior of EC QCL in Fig. 5.4(a) is very much similar to standalone monolithic QCL chip discussed in previous sub-section, including the sign change of the optical field at each half period of SP. Although the 2nd threshold is increased, SP do not change their form. However, the frequency is reduced from 454 GHz down to 110 GHz (the repetition rate of intensity pulses changes from 909 to 220 GHz) [98]. The QCL now operates on overtones of the external cavity. The round-trip time of the cold cavity is $T_{cav}=8.2$ ps. A slightly longer pulse train period of 8.8 ps in Fig. 5.4 is caused by the absorption of the leading edge and re-emission of the trailing pulse edge, the well-known effect accompanying propagation of an optical pulse in a gain medium [72], [112].

Like in a standalone FP-cavity QCL, the EC QCL does not operate in the ML regime. Its IAC trace in Fig. 5.4(c) has the peak-to-background ratio of 8:1.5 (as opposed to 8:1 for a perfect ML).

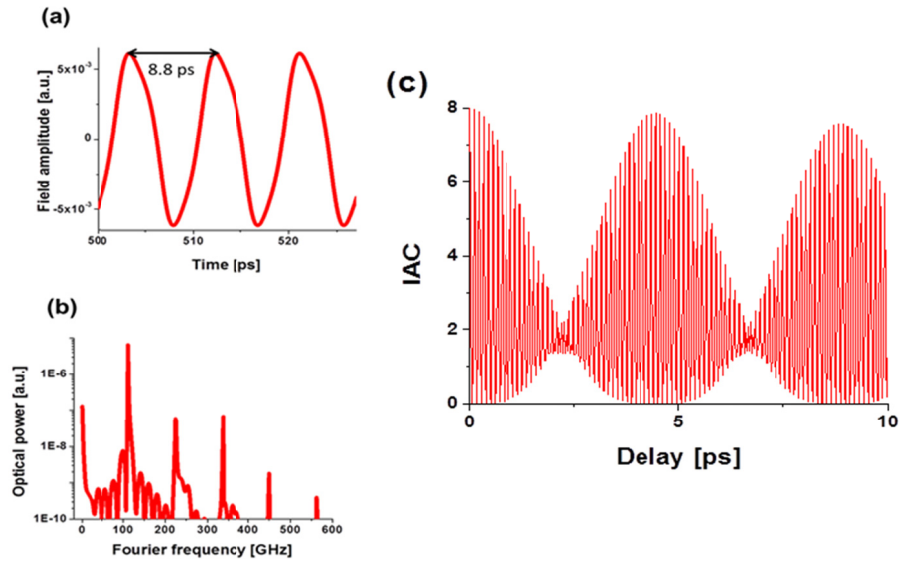


Fig. 5.4. Results of numerical simulations with TW model for QCL with the chip length of 100 μm and external reflector placed at 900 μm distance from the AR coated back chip facet. Normalized pump rate is $p=4.3$. (a) Field amplitude waveform (b) Optical power spectra and (c) 2nd order interferometric autocorrelation function (IAC). QCL parameters are from Table 1.

We attribute reduced IAC contrast to the pulse width being just a half of the SP period. For an incoherent multimode regime with random relative phases of the modes (CW noise regime), the peak-to-background ratio would be of 8:3 [12], [77], like the one observed [29], [39], [74] and numerically modeled [45] in mm-long FP-cavity QCLs (see also Appendix C).

The main lasing mode [at zero frequency in Fig. 5.4(b)] is highly inhibited in the optical spectrum. It is by more than 100 dB lower than the two dominant adjacent modes of the external cavity at ± 110 GHz offset frequencies (because of the mirror symmetry of the spectrum, the figure shows only the positive frequency part). Unlike the spectrum in Fig. 5.4(b), a conventional ML would reveal excitation of many cavity modes with a Gaussian (or hyperbolic secant) spectral envelope and the main central mode being of the highest amplitude.

Like in the case of standalone QCL, we observe a SP/CW hysteresis loop between the domains of self-starting SP and CW operation in function of the pump current p . For the sake of brevity we exemplify below only the case of decreasing p in small steps of $\delta p = 0.05$ starting from $p = 10$. Fig. 5.5(a) shows the bifurcation diagram of extrema of the output power. Comparing the waveform evolution in the EC QCL to its counterpart in Fig. 5.2 for the standalone QCL chip, the EC QCL shows not only more latent oscillations defined by the time scale of the external cavity round-trip but also the period doubling exists in the region at the higher pump rates extending down to $p = 4.7$. However, self-pulsations are more difficult to excite and require higher pump rates. Therefore in stand-alone FP cavity QCL the lowest p required for the “kick” excitation of SP is 1.5 while in EC QCL it is at $p \sim 2.5$ [98].

The contour plot in Fig. 5.5(b) is the bifurcation diagram of the output waveform resolved on the fast and slow time scales. It shows evolution of the fast oscillations in the output power waveform within two subsequent round-

trips in external cavity and in function of the adiabatically decreasing pump rate p . The waveform remains always periodic in the considered pump range. At normalized pump $p > 4.7$ the period of SP is roughly equal to the overall cavity round-trip time T_{cav} while at $2.5 < p < 4.7$, the period of the output power oscillations is close to $T_{cav}/2$.

The evolution of the normalized recurrence period density entropy with the pump rate is displayed in Fig. 5.5(c). The low value of RPDE confirms regular periodic oscillations in the studied range of p above $p \sim 2.5$ with a few regions of perfect periodicity. As in standalone QCL in Fig. 5.3(b), RPDE shows a spiking behavior at the SP switching-off threshold, which is caused by the loss of stability of the SP regime, as discussed in relation to Fig. 5.3(b).

Essentially, we reach a regular SP despite the period of such self-pulsations being much longer than the gain recovery time T_1 . This evidences that the EC provides a “memory effect” and sustain periodic pulsations on the time intervals larger than the gain medium can support [98].

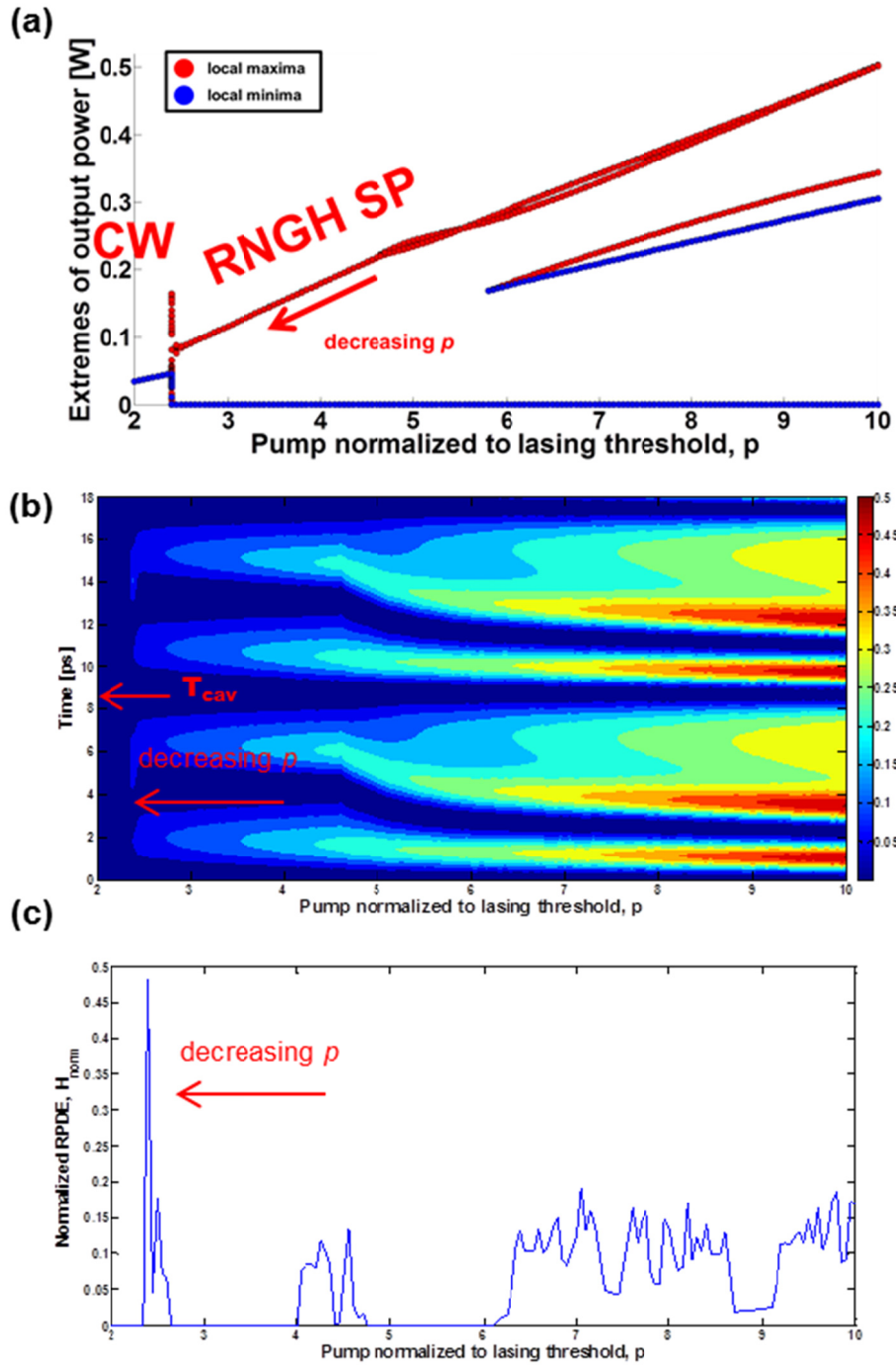


Fig. 5.5. Free tuning of the same EC QCL chip as in Fig. 5.4. (a) Extrema of output power waveform (red circles for P_{max} , blue for P_{min}) while decreasing normalized pump p with 0.05 step. Total number of periods per constant step is 50 and we cut the initial transient of the first 25 periods per step. (b) Contour plot for the same case as in (a). (c) Normalized RPDE with the same embedding parameters as in Fig. 5.3(b) ($m=4$, $\tau=10$, $r=0.003$).

5.3.3. QCL in ~cm long EC

Being encouraged with the ~100 GHz field flopping frequency obtained in mm-long EC QCL in the previous subsection, we examine if the EC length can be pushed further, e.g. to the cm length scale. However, further increase of the external reflector distance to 9.9 mm from the AR coated chip facet (total round-trip T_{cav} of 68.3 ps) results in existence of CW output in the whole range of the pumping rates representing any practical interest. Thus only this case of our numerical simulations is in agreement with the previous theoretical studies [102], [103] predicting enhanced stability of QCLs with optical feedback. Fig. 5.6 shows field amplitude waveform, optical spectra and 2nd order IAC function respectively, when the pump rate is set to very high level of $p=27$ while the initial field in the cavity is of zero amplitude [98]. Under these conditions we do observe self-starting SP in the output power waveform. However, these SP are not any more of the RNGH type. The output power waveform has a strong DC component like in the case of a long unidirectional ring laser discussed in [71]. The absence of RNGH self-pulsations can be attributed to a too low cavity filling with the gain medium and respectively to a negligibly small effect from the induced SHB and polarization gratings. Although self-pulsations are periodic, the frequency of SPs is at the 5th harmonic of the external cavity frequency. Such period fractioning is in contrast with the period multiplication behavior of the RNGH SP in FP-cavity QCL and mm-long EC QCL from previous sections [98]. The period of self-pulsations 13.5 ps does not match the propagation time neither in the gain chip nor in the EC.

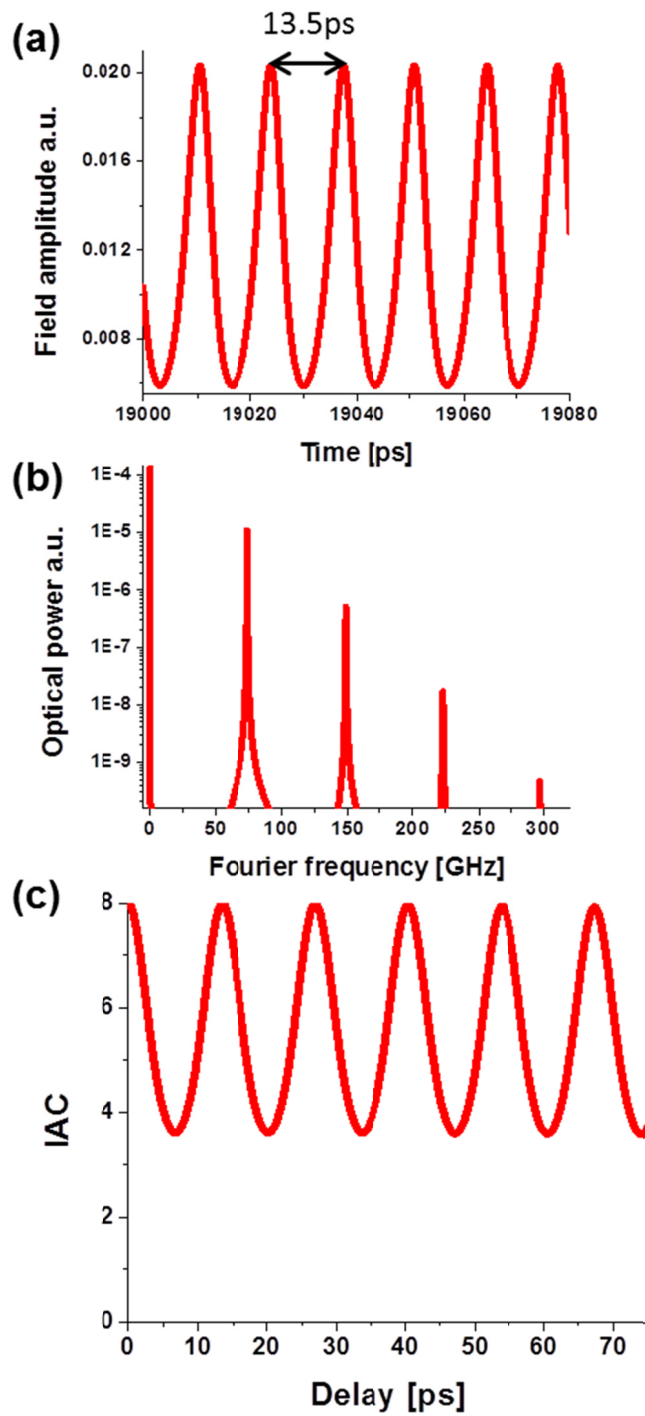
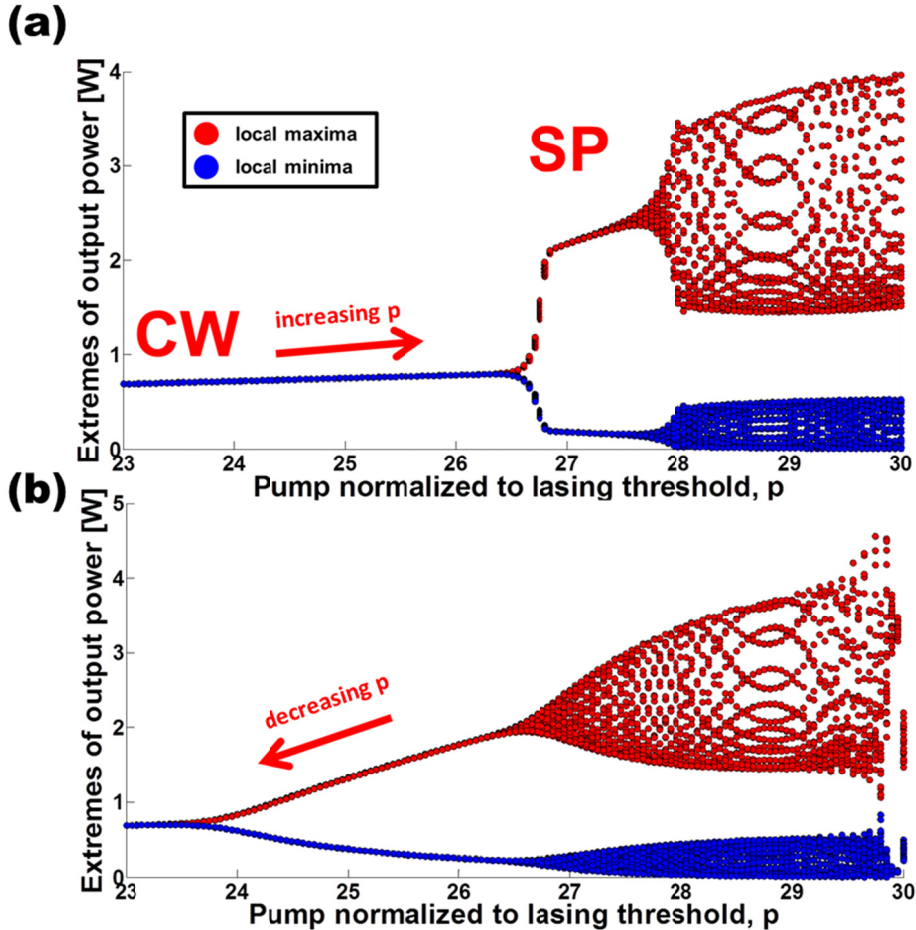


Fig. 5.6. EC QCL chip with the cavity length of 100 μm and external reflector placed at 9.9 mm distance from the AR coated front chip facet, pumped at $p=27$. Initial conditions assume zero field amplitude. (a) Field amplitude waveform showing (b) Optical power spectra (c) IAC trace.

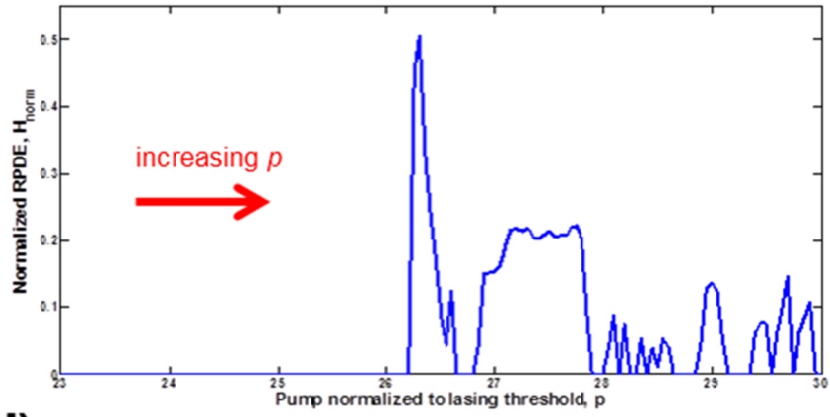
In Fig. 5.7 we plot the bifurcation diagrams of the extreme values of output power ((a) and (b)), normalized RPDEs ((c) and (d)) and waveform evolution contour plots ((e) and (f)) obtained for increasing and decreasing pump rate. With adiabatically increasing p , the self-starting SP occur at pump rates above $p=26.5$ [Fig. 5.7(a)], while adiabatic decrease of p shows switching from SP to CW at a lower pump rate of $p\sim 23.5$ [Fig. 5.7(b)]. Like in Fig. 5.2 we thus observe bistable SP/CW behavior. However, the threshold of self-pulsations is prohibitively high for attempting any practical realization. We may thus conclude that SP are suppressed in ~ 1 cm long EC. The RPDE entropy well below 0.5 in both cases [Fig. 5.7(c) and Fig. 5.7(d)] indicates that the output power waveform has a regular character as opposed to a quasi-periodic (chaotic) signal. This is true even at very high pump rates $p>28$, when the waveform exhibits a multitude of the local maxima and minima as seen from Fig. 5.7(a) and (b). Fig. 5.7(e) shows that in the range of p between 26.5 and 27.7 self-pulsing occurs at a frequency close to $T_{cav}/5$. However, above $p\sim 27.7$ the period changes to a value close to one cavity round-trip time T_{cav} . Likewise for decreasing pump rate, starting with initial period of $\sim T_{cav}$, the period of SP is reduced to $\sim T_{cav}/5$ at some point around $p\sim 27$ Fig. 5.7(f).

In the literature, there are also predictions [103] and experimental confirmations [100] of the possibility of producing regular self-pulsations at the external cavity frequency. However, in [100], further increase of feedback strength results in erratic pulsing output which is a result of both fast oscillations at EC frequency and the slower variations corresponding to low frequency fluctuations. Note that in our model we are in a regime of very high optical feedback, much higher than those reported in [100] and [103]. This is in agreement with the results in [103] where for low values of linewidth enhancement factor (LEF) (case of MIR QCLs as opposed to LDs) it is necessary to use higher critical feedback level to reach unstable regime. In addition, it was shown in [103] that longer EC results in lower critical value of

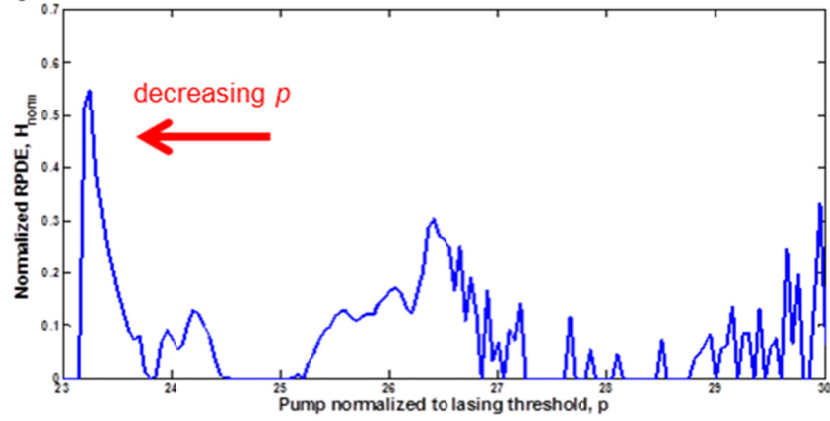
LEF which in return requires higher critical feedback for the start of unstable regime.



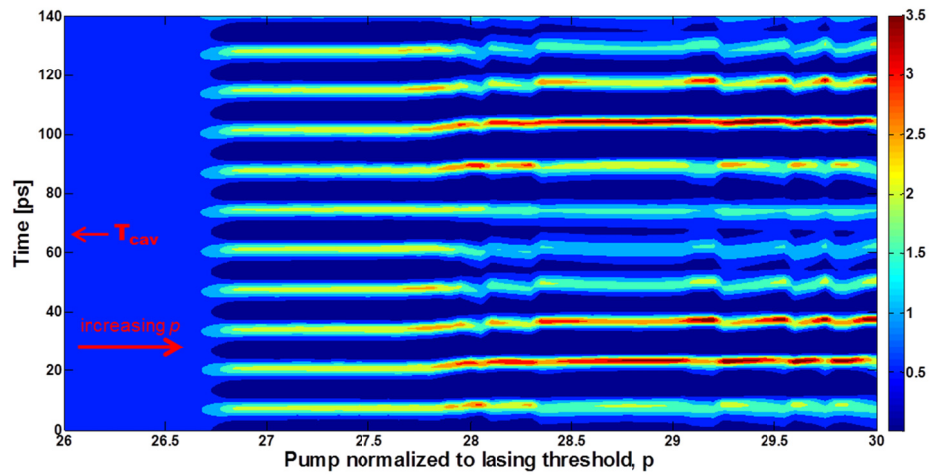
(c)



(d)



(e)



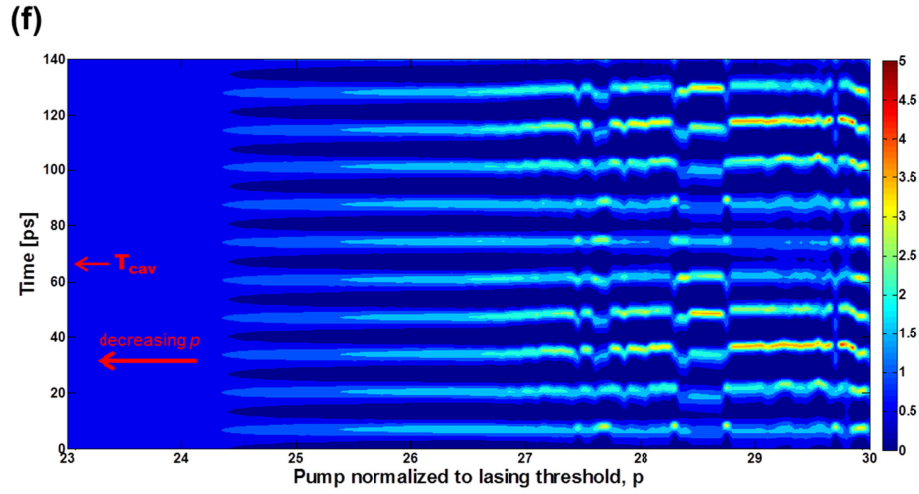


Fig. 5.7. Results of free tuning for the EC QCL chip with the cavity length of $100 \mu\text{m}$ and external reflector placed at 9.9 mm distance from the AR coated front chip facet. (a) Adiabatic increase of p with 0.05 step, extremes of output power waveform (red circles for P_{max} , blue for P_{min}) showing switching between regimes of CW and SP (at $p \sim 26.5$). (b) Adiabatic decrease of p with 0.05 step, extremes of output power waveform showing switching between regimes of SP and CW (at $p \sim 23.5$). (c) Normalized RPDE for the case of increasing p with the following embedding parameters: $m=4$, $\tau=10$, $r=0.003$. (d) Normalized RPDE for the case of decreasing p and the same embedding parameters as in (c). Total number of periods per constant step is 10 and we cut the initial transient of the first 5 periods per step. (e) Waveform evolution contour plot for increasing p and (f) the same diagram for decreasing p .

5.4. Numerical results for long QCL chip in EC configuration

In this section we present numerically calculated field waveforms, optical spectra, RF power spectra and second order interferometric autocorrelation of the QCL gain chips of 1.5 mm length placed in EC resonators of different lengths and compare these with the results obtained for the standalone QCL chips.

In Fig. 5.8(a) we show field amplitude waveforms in case of standalone QCL chip with the cavity round-trip time of $T_{\text{cav}} = 33 \text{ ps}$ with front and back facet

reflectivities of 27%. Fig. 5.8(b)-(d) show field waveforms for the same chip with the AR coated front facet and with the additional external reflector positioned at 6 mm, 13.5 mm or 28.5 mm from the front facet. In all four configurations pump rate normalized to lasing threshold is of $p=2$, but have in mind that this is different current density in each case. The optical field waveforms in Fig. 5.8(a)-(c) develops into a quasi-periodic square waves. The envelope of wave packet just slightly changes at each round-trip, yielding the quasi-periodic chaotic behavior [45]. Fig. 5.8(d) shows a train of much more regular pulses.

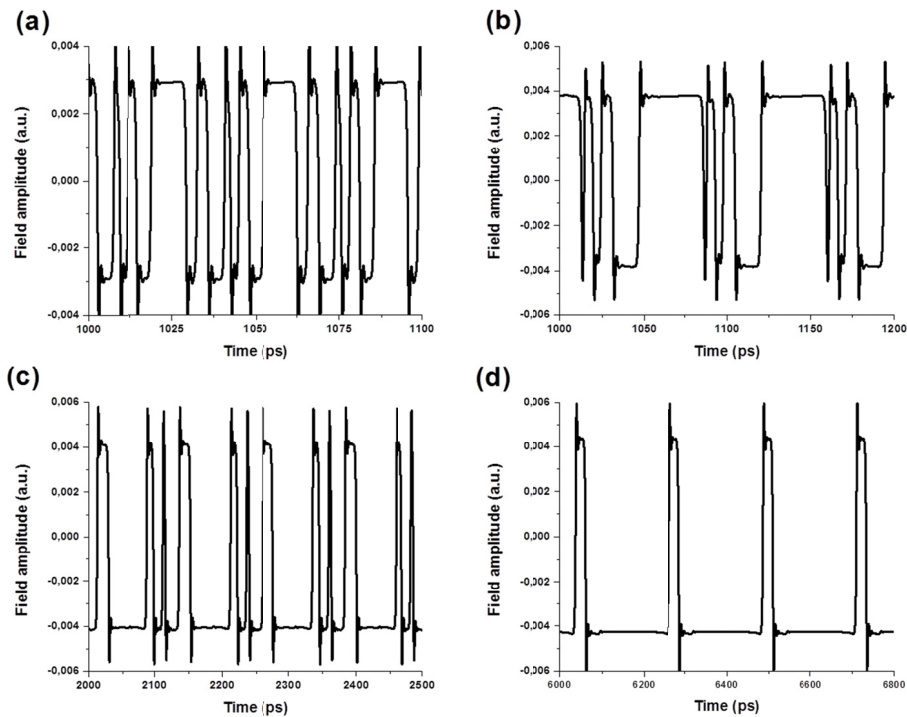


Fig. 5.8. Field amplitude waveforms for 1.5 mm QCL chip in case (a) monolithic QCL, (b) 6 mm EC (c) 13.5 mm EC (d) 28.5 mm EC. Total cavity round-trip times (gain section and the EC) in cases shown in (a)-(d) are 33 ps, 73 ps, 123.1 ps and 223.2 ps respectively. Pump normalized to lasing threshold $p=2$. All other parameters used are listed in Table 1.

Corresponding optical spectra for the four considered configurations from Fig. 5.8 are displayed in Fig. 5.9. Optical spectra for the monolithic chip in Fig. 5.9(a) shows suppression of the main lasing mode in agreement with multimode behavior observed experimentally in quantum cascade lasers without optical feedback [29], [39]. However, simulations for the 3 values of external feedback Fig. 5.9(b)-(d) show that main lasing component is not suppressed and with the increase of the length of EC, higher order modes disappear (Fig. 5.9(d)). This is also observed in the field waveforms by comparing Fig. 5.8(d) with Fig. 5.8(a). Separation of modes and repetition rate in EC configuration is lowered as compared to monolithic cavity. Thus the propagation delay in external cavity serves to filter the spectrum of excited modes.

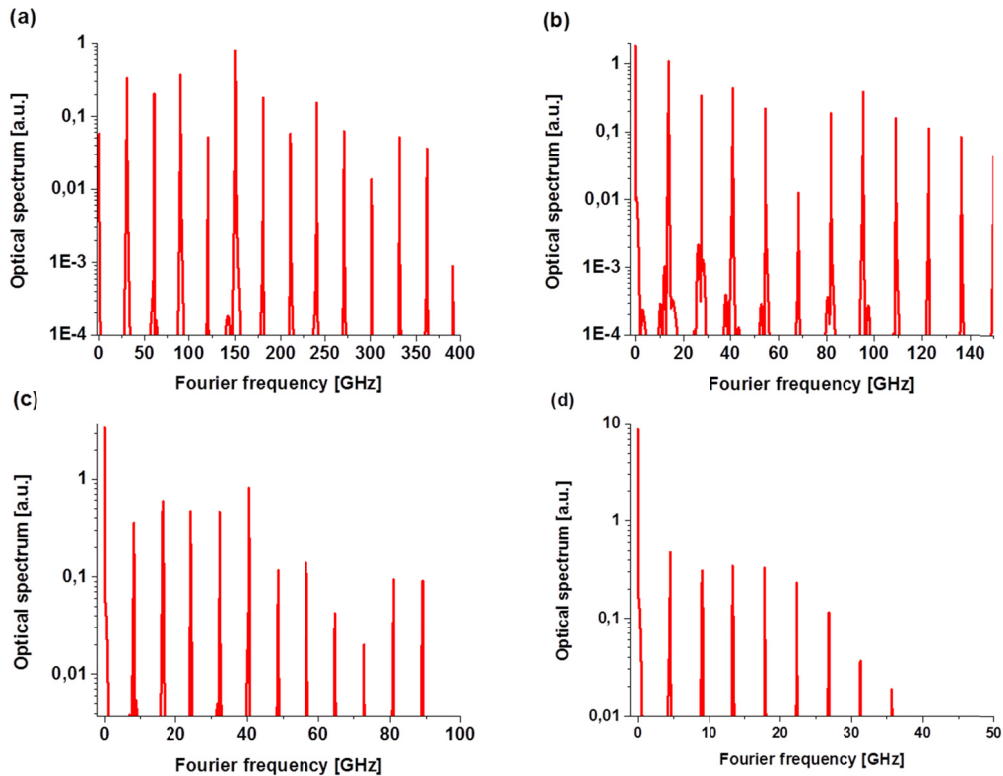


Fig. 5.9. Optical power spectra for 1.5 mm QCL chip in case (a) monolithic QCL, (b) 6 mm EC (c) 13.5 mm EC (d) 28.5 mm EC. All parameters are the same as in Fig. 5.8.

These observations are in agreement with the experimental results reported in the literature [99], [102] showing that external optical feedback indeed results in increased stability of QCLs. Moreover, the regime shown in Fig. 5.9(d) corresponds to the stable “regime V” described in [99], [108]. With the increase of the EC laser stays in the same stable regime, while the decrease of EC length towards the monolithic case results in the behavior similar to the so-called coherence-collapse regime or “fourth regime” in [99]. RF spectra displayed in Fig. 5.10(a)-(d) also testifies that case (d) has the most regular pattern of spectra with sideband modulations.

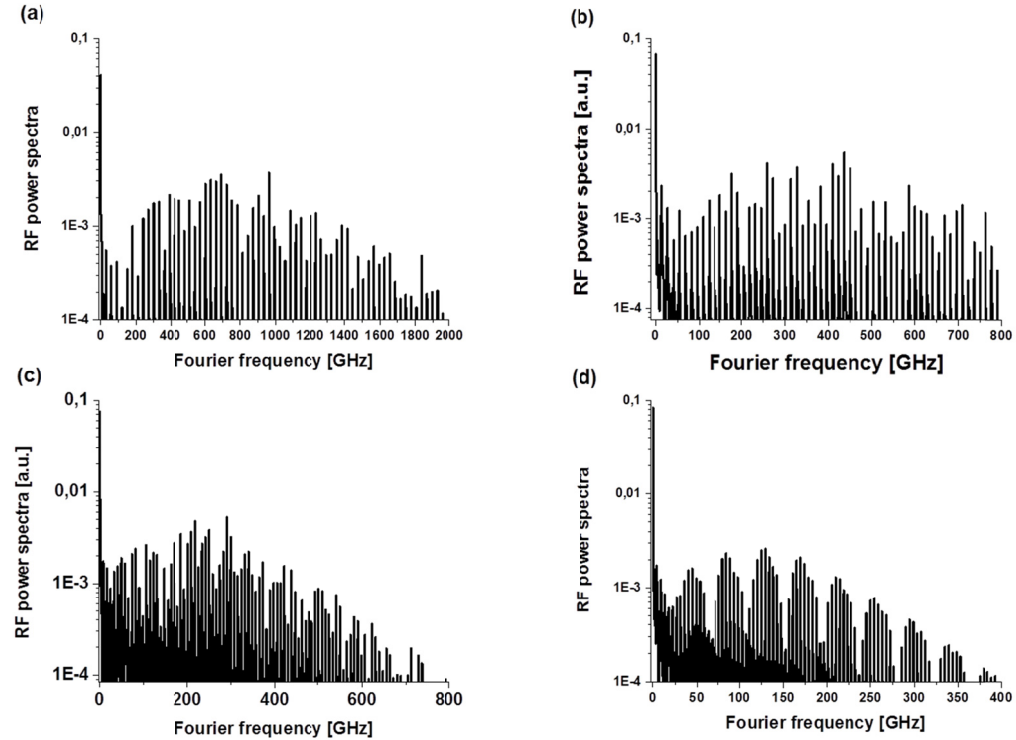


Fig. 5.10. RF power spectra corresponding to the same data as in Fig. 5.8: 1.5 mm QCL chip in case of (a) monolithic QCL, (b) 6 mm EC (c) 13.5 mm EC (d) 28.5 mm EC.

In Fig. 5.11 we calculate the interferometric autocorrelation traces for the four cases discussed above and observe that the coherence time seen from the

traces increases (we use HWHM of the interferometric autocorrelation peak at $\tau=0$) with the increase of the EC length.

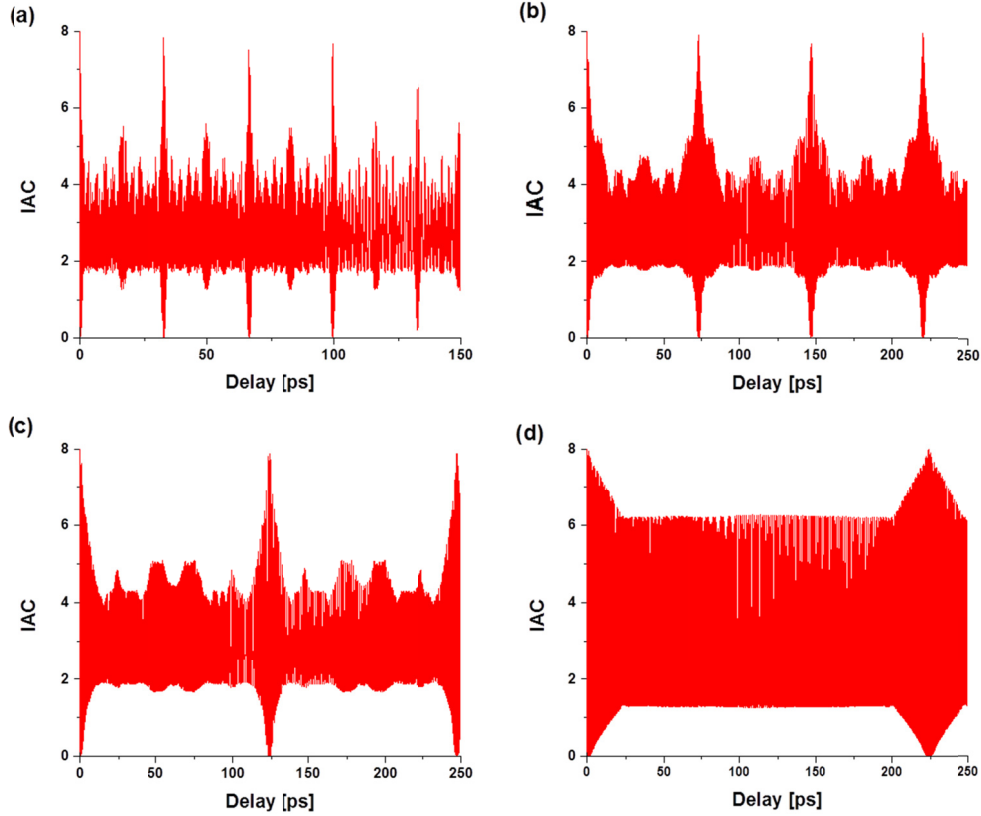


Fig. 5.11. Second-order interferometric autocorrelation functions for the 4 configurations displayed in Fig. 5.8-Fig. 5.10. (a) monolithic QCL, (b) 6 mm EC (c) 13.5 mm EC (d) 28.5 mm EC.

One can see that the peak to background ratio of interferometric AC trace in Fig. 5.11(a) in case of monolithic QCL chip is worse than 8:3 and our quasi-periodic chaotic pulse train from Fig. 5.8(a) perfectly explains the experimentally measured interferometric AC traces in [39], including nontrivial pulse structure in between cavity round-trips. IAC traces in Fig. 5.11(a), (b) and (c) with secondary peaks at fractional cavity round-trip times attest that multiple pulses travel through the cavity during one round-trip

time as seen in Fig. 5.8(a), (b) and (c). IAC trace in Fig. 5.11(d) attest that only one back and forth phase alternation occurs at one round-trip as indicated in square-shape pulses Fig. 5.8(d). Apart from this switching point, the amplitude remains constant. (Note that a waveform of constant amplitude along the whole cavity round-trip will produce just a uniform amplitude pattern in IAC interference fringes).

Our simulations thus indicate that with EC feedback it is possible to obtain regular pulse train with standard long cavity FP QCLs as opposed to the case of monolithic chip which shows irregular multimode behavior observed both from the field waveform and the optical power spectra. However, these pulses have square shape and are not yet ideal for practical needs.

5.4.1. Pulse correction with a two-beam interference

We notice that the square-shape waveform can be corrected into a train of narrow pulses using a two-beam interference, taking the field amplitude waveform and subtracting its delayed copy.

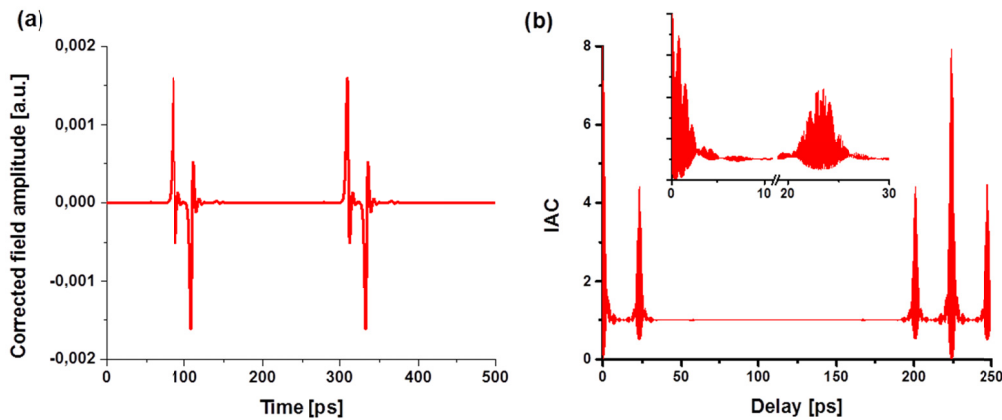


Fig. 5.12. (a) Corrected field waveform using two-beam interference. Original field waveform is shown in Fig. 5.8(d), its copy is delayed by 0.5 ps and then subtracted. (b) Interferometric autocorrelation of the corrected waveform shown in (a). Inset shows zoom-in at the pulses.

Firstly, we use the 1.5 mm chip with 28.5 mm EC and waveform shown in Fig. 5.8(d). When we apply the pulse correction using delay time of 0.5 ps we get the new field waveform and IAC trace shown in Fig. 5.12.

On the other hand, if on the same field amplitude from Fig. 5.8(d) we apply the shift equal to a half of the total cavity round-trip time (111.5 ps), resulting pulse corrected field amplitude and IAC become as shown in Fig. 5.13. Autocorrelation peaks in Fig. 5.13(b) have very high peak-to background ratio of 8:1 and are separated by half of cavity round-trip that corresponds to the separation between the pulses in waveform trace in Fig. 5.13(a). The FWHM of the pulses in autocorrelation is 25 ps. However, the waveform in Fig. 5.13(a) shows that the pulses are not ideal since they are square shaped.

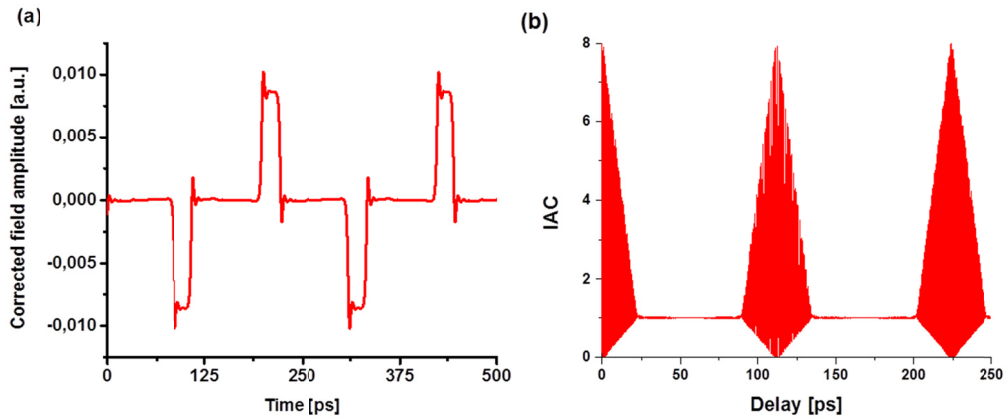


Fig. 5.13. (a) Field amplitude that corresponds to the delay of 111.5 ps (half of the round-trip) between the original and delayed copy. (b) Interferometric autocorrelation of waveform in (a).

6. Conclusion

In conclusion, in this dissertation (as well as in [45]) we have clarified conditions for multimode RNGH instability in a Fabry-Pérot cavity laser and proposed a new explanation for low second threshold in quantum cascade lasers, which is based on a combined effect of the carrier coherence and carrier population gratings. We have studied the impact of the cavity length on the waveform of RNGH self-pulsations and shown that short-cavity QCLs can produce a regular train of ultrashort pulses. There is even a possibility to obtain superradiant-like emission. Our findings open a practical way of achieving ultra-short pulse production regimes in the MIR spectral range. Applying the same analysis to conventional laser diodes we find that carrier diffusion in the active bulk semiconductor material or quantum wells prevents the LDs from RNGH self-pulsations. Next, this dissertation (and [46]) provides a simple analytical expression for the RNGH instability threshold in a quantum cascade laser with FP cavity which can serve as a versatile tool that can easily be applied in practical situations requiring analysis of QCL dynamic behavior and estimation of its RNGH instability threshold.

The dissertation provides an explanation of the difficulties for practical use of RNGH self-pulsations in millimeter cavity length QCLs. Namely, they originate from the quasiperiodic chaotic behavior of the pulse train when the coherence length is smaller than the length of the sample. The use of external cavity QCLs is proposed in order to obtain regular RNGH self-pulsations. The

propagation time in the external cavity (the pulse delay time) serves to provide a memory effect and thus improves coherence time of the QCL pulse train. In addition, the EC reduces the pulse repetition rate of self-pulsations. Our model system assumes an anti-reflection coated front facet of the QCL chip facing the EC reflector which is a very different approach compared to model systems in the literature, that is QCL subjected to the optical feedback with non-vanishing reflectivity on the front facet. Moreover, none of these previous studies on QCLs with optical feedback and in the EC considered coherence effects leading to RNGH self-pulsating instabilities observed in standalone QCLs. The main results indicate that for short (100 μm) chip there is a possibility of: (i) bistable operation in free-tuning (adiabatic increasing/decreasing of pump current), (ii) lowering of the pulse repetition rate for chip with 900 μm long EC and (iii) suppression of SP in 9 mm long EC. Additionally, we have applied recurrence period density entropy, a well-known method used in the field of time series analysis, to determine periodicity of the output power waveforms. Finally, the possibility of production of regular pulses using the long chip in EC with additional pulse correction is investigated as well.

The future work will consist in taking the inhomogeneous broadening of the gain curve and its shape into account, the feature that directly affects the observation of the QCL's RNGH instability in experiments.

References

- [1] J. Faist, F. Capasso, D. L. Sivco, C. Sirtori, A. L. Hutchinson, and A. Y. Cho, "Quantum Cascade Laser," *Science* (80-.), vol. 264, no. 5158, pp. 553–556, 1994.
- [2] J. Faist, F. Capasso, C. Sirtori, D. L. Sivco, A. L. Hutchinson, and A. Y. Cho, "Room temperature mid-infrared quantum cascade lasers," *Electron. Lett.*, vol. 32, no. 6, p. 560, 1996.
- [3] Y. Bai, N. Bandyopadhyay, S. Tsao, S. Slivken, and M. Razeghi, "Room temperature quantum cascade lasers with 27% wall plug efficiency," *Appl. Phys. Lett.*, vol. 98, no. 18, p. 181102, 2011.
- [4] O. Cathabard, R. Teissier, J. Devenson, J. C. Moreno, and A. N. Baranov, "Quantum cascade lasers emitting near 2.6 μm ," *Appl. Phys. Lett.*, vol. 96, no. 14, p. 141110, 2010.
- [5] G. Scalari *et al.*, "Magnetically assisted quantum cascade laser emitting from 740 GHz to 1.4 THz," *Appl. Phys. Lett.*, vol. 97, no. 8, p. 81110, 2010.
- [6] A. Hugi *et al.*, "External cavity quantum cascade laser tunable from 7.6 to 11.4 μm ," *Appl. Phys. Lett.*, vol. 95, no. 6, p. 61103, 2009.
- [7] Y. Bai, S. Slivken, S. Kuboya, S. R. Darvish, and M. Razeghi, "Quantum cascade lasers that emit more light than heat," *Nat. Photonics*, vol. 4, no. 2, pp. 99–102, 2010.
- [8] P. Q. Liu *et al.*, "Highly power-efficient quantum cascade lasers," *Nat. Photonics*, vol. 4, no. 2, pp. 95–98, 2010.
- [9] R. F. Curl *et al.*, "Quantum cascade lasers in chemical physics," *Chem. Phys. Lett.*, vol. 487, no. 1–3, pp. 1–18, 2010.

- [10] M. S. Vitiello, G. Scalari, B. Williams, and P. De Natale, "Quantum cascade lasers: 20 years of challenges," *Opt. Express*, vol. 23, no. 4, p. 5167, 2015.
- [11] C. Jirauschek and T. Kubis, "Modeling techniques for quantum cascade lasers," *Appl. Phys. Rev.*, vol. 1, no. 1, p. 11307, 2014.
- [12] J. Faist, *Quantum Cascade Lasers*. OUP Oxford, 2013.
- [13] A. Hugi, G. Villares, S. Blaser, H. C. Liu, and J. Faist, "Mid-infrared frequency comb based on a quantum cascade laser," *Nature*, vol. 492, no. 7428, pp. 229–233, 2012.
- [14] R. Huber, F. Tauser, A. Brodschelm, M. Bichler, G. Abstreiter, and A. Leitenstorfer, "How many-particle interactions develop after ultrafast excitation of an electron-hole plasma," *Nature*, vol. 414, no. 6861, pp. 286–289, 2001.
- [15] R. Torre, P. Bartolini, and R. Righini, "Structural relaxation in supercooled water by time-resolved spectroscopy," *Nature*, vol. 428, no. 6980, pp. 296–299, 2004.
- [16] J. M. Dudley, G. Genty, and S. Coen, "Supercontinuum generation in photonic crystal fiber," *Rev. Mod. Phys.*, vol. 78, no. 4, pp. 1135–1184, 2006.
- [17] J. J. Macklin, J. D. Kmetec, and C. L. Gordon, "High-order harmonic generation using intense femtosecond pulses," *Phys. Rev. Lett.*, vol. 70, no. 6, pp. 766–769, 1993.
- [18] E. A. Gibson *et al.*, "Coherent Soft X-ray Generation in the Water Window with Quasi-Phase Matching," *Science (80-.)*, vol. 302, no. 5642, pp. 95–98, 2003.
- [19] R. Paiella *et al.*, "Monolithic active mode locking of quantum cascade lasers," *Appl. Phys. Lett.*, vol. 77, no. 2, pp. 169–171, 2000.
- [20] T. Udem, R. Holzwarth, and T. W. Hänsch, "Optical frequency metrology," *Nature*, vol. 416, no. 6877, pp. 233–237, 2002.
- [21] H. A. Haus, "Mode-locking of lasers," *IEEE J. Sel. Top. Quantum Electron.*, vol. 6, no. 6, pp. 1173–1185, 2000.
- [22] H. Choi *et al.*, "Gain Recovery Dynamics and Photon-Driven Transport in Quantum Cascade Lasers," *Phys. Rev. Lett.*, vol. 100, no. 16, p. 167401, 2008.
- [23] H. Choi *et al.*, "Femtosecond dynamics of resonant tunneling and superlattice relaxation

- in quantum cascade lasers," *Appl. Phys. Lett.*, vol. 92, no. 12, p. 122114, 2008.
- [24] R. Paiella *et al.*, "High-speed operation of gain-switched midinfrared quantum cascade lasers," *Appl. Phys. Lett.*, vol. 75, no. 17, pp. 2536–2538, 1999.
- [25] C. Y. Wang *et al.*, "Stable Mode-Locked Pulses from Mid-Infrared Quantum Cascade Lasers," in *Conference on Lasers and Electro-Optics/Quantum Electronics and Laser Science Conference and Photonic Applications Systems Technologies*, 2008, p. CPDA11.
- [26] C. Y. Wang *et al.*, "Mode-locked pulses from mid-infrared Quantum Cascade Lasers," *Opt. Express*, vol. 17, no. 15, pp. 12929–12943, 2009.
- [27] V.-M. Gkortsas *et al.*, "Dynamics of actively mode-locked Quantum Cascade Lasers," *Opt. Express*, vol. 18, no. 13, p. 13616, 2010.
- [28] C. R. Menyuk and M. A. Talukder, "Self-Induced Transparency Modelocking of Quantum Cascade Lasers," *Phys. Rev. Lett.*, vol. 102, no. 2, p. 23903, 2009.
- [29] C. Y. Wang *et al.*, "Coherent instabilities in a semiconductor laser with fast gain recovery," *Phys. Rev. A*, vol. 75, no. 3, p. 31802, 2007.
- [30] H. Risken and K. Nummedal, "Self-pulsing in lasers," *J. Appl. Phys.*, vol. 39, no. 10, pp. 4662–4672, 1968.
- [31] R. Graham and H. Haken, "Quantum theory of light propagation in a fluctuating laser-active medium," *Zeitschrift für Phys.*, vol. 213, no. 5, pp. 420–450, 1968.
- [32] M. D. Crisp, "Adiabatic-following approximation," *Phys. Rev. A*, vol. 8, no. 4, pp. 2128–2135, 1973.
- [33] L. W. Hillman, J. Krasinski, R. W. Boyd, and C. R. Stroud, "Observation of higher order dynamical states of a homogeneously broadened laser," *Phys. Rev. Lett.*, vol. 52, no. 18, pp. 1605–1608, 1984.
- [34] E. M. Pessina, G. Bonfrate, F. Fontana, and L. A. Lugiato, "Experimental observation of the Risken-Nummedal-Graham-Haken multimode laser instability," *Phys. Rev. A - At. Mol. Opt. Phys.*, vol. 56, no. 5, pp. 4086–4093, 1997.
- [35] T. Voigt, M. O. Lenz, F. Mitschke, E. Roldán, and G. J. De Valcárcel, "Experimental investigation of Risken-Nummedal-Graham-Haken laser instability in fiber ring lasers,"

Appl. Phys. B Lasers Opt., vol. 79, no. 2, pp. 175–183, 2004.

- [36] J. L. Font, R. Vilaseca, F. Prati, and E. Roldán, “Coexistence of single-mode and multi-longitudinal mode emission in the ring laser model,” *Opt. Commun.*, vol. 261, no. 2, pp. 336–341, 2006.
- [37] E. Roldán, G. J. de Valcárcel, J. F. Urchueguía, and J. M. Guerra, “Observability of the Risken-Nummedal-Graham-Haken instability in Nd:YAG lasers,” *J. Opt. Soc. Am. B*, vol. 20, no. 5, p. 816, 2003.
- [38] E. M. Pessina, F. Prati, J. Redondo, E. Roldán, and G. J. de Valcárcel, “Multimode instability in ring fiber lasers,” *Phys. Rev. A - At. Mol. Opt. Phys.*, vol. 60, no. 3, pp. 2517–2528, 1999.
- [39] A. Gordon *et al.*, “Multimode regimes in quantum cascade lasers: From coherent instabilities to spatial hole burning,” *Phys. Rev. A*, vol. 77, no. 5, p. 53804, 2008.
- [40] H. Knapp, H. Risken, and H. D. Vollmer, “Instability of laser cw oscillation in the presence of a passive medium,” *Appl. Phys.*, vol. 15, no. 3, pp. 265–270, 1978.
- [41] T. S. Mansuripur *et al.*, “Single-mode instability in standing-wave lasers: The quantum cascade laser as a self-pumped parametric oscillator,” *Phys. Rev. A*, vol. 94, no. 6, p. 63807, 2016.
- [42] I. Gravé, M. Segev, and A. Yariv, “Observation of phase conjugation at 10.6 μm via intersubband third-order nonlinearities in a GaAs/AlGaAs multi-quantum-well structure,” *Appl. Phys. Lett.*, vol. 60, no. 22, pp. 2717–2719, 1992.
- [43] F. Capasso, C. Sirtori, and A. Y. Cho, “Coupled quantum well semiconductors with giant electric field tunable nonlinear optical properties in the infrared,” *IEEE J. Quantum Electron.*, vol. 30, no. 5, pp. 1313–1326, 1994.
- [44] T. Herr *et al.*, “Temporal solitons in optical microresonators,” *Nat. Photonics*, vol. 8, no. 2, pp. 145–152, 2014.
- [45] N. N. Vukovic, J. Radovanovic, V. Milanovic, and D. L. Boiko, “Low-Threshold RNGH Instabilities in Quantum Cascade Lasers,” *IEEE J. Sel. Top. Quantum Electron.*, vol. 23, no. 6, pp. 1–16, 2017.

- [46] N. Vukovic, J. Radovanovic, V. Milanovic, and D. L. Boiko, "Analytical expression for Risken-Nummedal-Graham-Haken instability threshold in quantum cascade lasers," *Opt. Express*, vol. 24, no. 23, p. 26911, 2016.
- [47] D. L. Boiko and P. P. Vasil'ev, "Superradiance dynamics in semiconductor laser diode structures," *Optics Express*, vol. 20, no. 9. p. 9501, 2012.
- [48] M. Bugajski, K. Pierscinski, D. Pierscinska, A. Szerling, and K. Kosiel, "Multimode instabilities in mid-infrared quantum cascade lasers," *Photonics Lett. Pol.*, vol. 5, no. 3, pp. 85–87, 2013.
- [49] N. Vukovic, J. Radovanovic, V. Milanovic, and D. L. Boiko, "Self-pulsing in monolithic and external cavity mid-IR QCLs," in *International School and Conference on Photonics - PHOTONICA2017*, 2017, p. 130.
- [50] N. Vukovic, J. Radovanovic, V. Milanovic, and D. L. Boiko, "Self-pulsations in QCLs," in *International Quantum Cascade Lasers School & Workshop IQCLSW 2016*, 2016, pp. 195–196.
- [51] B. Jonsson and S. T. Eng, "Solving the Schrodinger equation in arbitrary quantum-well potential profiles using the transfer matrix method," *IEEE J. Quantum Electron.*, vol. 26, no. 11, pp. 2025–2035, 1990.
- [52] C. Jirauschek, "Accuracy of Transfer Matrix Approaches for Solving the Effective Mass Schrödinger Equation," *IEEE J. Quantum Electron.*, vol. 45, no. 9, pp. 1059–1067, 2009.
- [53] C. Juang, K. J. Kuhn, and R. B. Darling, "Stark shift and field-induced tunneling in Al(x)Ga(1-x)As/GaAs quantum-well structures," *Phys. Rev. B*, vol. 41, no. 17, pp. 12047–12053, 1990.
- [54] U. Ekenberg, "Nonparabolicity effects in a quantum well: Sublevel shift, parallel mass, and Landau levels," *Phys. Rev. B*, vol. 40, no. 11, pp. 7714–7726, 1989.
- [55] N. Vuković, V. Milanović, and J. Radovanović, "Influence of nonparabolicity on electronic structure of quantum cascade laser," *Phys. Lett. A*, vol. 378, no. 30–31, pp. 2222–2225, 2014.
- [56] N. Vukovic, J. Radovanovic, and V. Milanovic, "Enhanced modeling of band nonparabolicity with application to a mid-IR quantum cascade laser structure," *Phys. Scr.*, vol. T162, p. 14014, 2014.

- [57] J. Ohtsubo, *Semiconductor Lasers*, vol. 111. Cham: Springer International Publishing, 2017.
- [58] N. Vukovic, J. Radovanovic, V. Milanovic, and D. L. Boiko, "Multimode RNGH instabilities of Fabry-Pérot cavity QCLs: impact of diffusion," *Opt. Quantum Electron.*, vol. 48, no. 4, p. 254, 2016.
- [59] V. V Kocharovsky, V. V Zheleznyakov, E. R. Kocharovskaya, and V. V Kocharovsky, "Superradiance: the principles of generation and implementation in lasers," *Usp. Fiz. Nauk*, vol. 187, no. 4, pp. 367–410, 2017.
- [60] V. V. Kocharovsky, A. A. Belyanin, E. R. Kocharovskaya, and V. V Kocharovsky, "Superradiant Lasing and Collective Dynamics of Active Centers with Polarization Lifetime Exceeding Photon Lifetime," in *Advanced Lasers*, vol. 193, O. Shulika and I. Sukhoivanov, Eds. Dordrecht: Springer Netherlands, 2015, pp. 1–388.
- [61] R. H. Pantell and H. E. Puthoff, *Fundamentals of quantum electronics*. Wiley, 1969.
- [62] R. W. Boyd, *Nonlinear Optics*, 3rd ed. Elsevier Science, 2008.
- [63] S. Appelt, A. Baranga, C. Erickson, M. Romalis, A. Young, and W. Happer, "Theory of spin-exchange optical pumping of ^3He and ^{129}Xe ," *Phys. Rev. A*, vol. 58, no. 2, pp. 1412–1439, 1998.
- [64] L. A. Lugiato, L. M. Narducci, E. V. Eschenazi, D. K. Bandy, and N. B. Abraham, "Multimode instabilities in a homogeneously broadened ring laser," *Phys. Rev. A*, vol. 32, no. 3, pp. 1563–1575, 1985.
- [65] N. V. Kravtsov, E. G. Lariontsev, and A. N. Shelaev, "Oscillation regimes of ring solid-state lasers and possibilities for their stabilization," *Laser Phys.*, vol. 3, pp. 21–62, 1993.
- [66] A. E. Siegman, *Lasers*. University Science Books, 1986.
- [67] C. Serrat and C. Masoller, "Modeling spatial effects in multi-longitudinal-mode semiconductor lasers," *Phys. Rev. A*, vol. 73, no. 4, p. 43812, 2006.
- [68] L. Gil and G. L. Lippi, "Phase Instability in Semiconductor Lasers," *Phys. Rev. Lett.*, vol. 113, no. 21, p. 213902, 2014.
- [69] L. Lugiato, F. Prati, and M. Brambilla, *Nonlinear Optical Systems*. Cambridge University Press, 2015.

- [70] N. Vuković, "Investigation of RNGH instabilities in quantum cascade lasers," in *SKIN AND TISSUE CANCER DETECTION USING LASER IMAGING The Book of Scientific Reports*, 1st ed., Ž. Cvejić, J. Radovanović, and D. Indjin, Eds. Novi Sad, Serbia: Liberte, 2017, pp. 112–116.
- [71] E. Roldan, G. J. de Valcarcel, F. Prati, F. Mitschke, and T. Voigt, "Multilongitudinal mode emission in ring cavity class B lasers," *arXiv Prepr. physics/0412071*, pp. 1–73, 2004.
- [72] S. L. McCall and E. L. Hahn, "Self-Induced Transparency," *Phys. Rev.*, vol. 183, no. 2, pp. 457–485, 1969.
- [73] X. Zeng and D. L. Boiko, "1/f noise in external-cavity InGaN diode laser at 420 nm wavelength for atomic spectroscopy," *Opt. Lett.*, vol. 39, no. 6, p. 1685, 2014.
- [74] A. V Antonov *et al.*, "Switching on and off the Risken-Nummedal-Graham-Haken instability in quantum cascade lasers," *arXiv Prepr. arXiv1711.10749*, pp. 1–31, 2017.
- [75] M. Wienold, L. Schrottke, M. Giehler, R. Hey, and H. T. Grahn, "Nonlinear transport in quantum-cascade lasers: The role of electric-field domain formation for the laser characteristics," *J. Appl. Phys.*, vol. 109, no. 7, p. 73112, 2011.
- [76] S. L. Lu, L. Schrottke, S. W. Teitworth, R. Hey, and H. T. Grahn, "Formation of electric-field domains in GaAs/Al_xGa_{1-x}As quantum cascade laser structures," *Phys. Rev. B*, vol. 73, no. 3, p. 33311, 2006.
- [77] J.-C. Diels and W. Rudolph, *Ultrashort laser pulse phenomena: fundamentals, techniques, and applications on a femtosecond time scale*. Elsevier, 2006.
- [78] D. von der Linde, "Characterization of the noise in continuously operating mode-locked lasers," *Appl. Phys. B*, vol. 39, no. 4, pp. 201–217, 1986.
- [79] M. J. W. Rodwell, D. M. Bloom, and K. J. Weingarten, "Subpicosecond laser timing stabilization," *IEEE J. Quantum Electron.*, vol. 25, no. 4, pp. 817–827, 1989.
- [80] E. N. Lorenz, "Deterministic Nonperiodic Flow," *J. Atmos. Sci.*, vol. 20, no. 2, pp. 130–141, 1963.
- [81] A. K. Wójcik, P. Malara, R. Blanchard, T. S. Mansuripur, F. Capasso, and A. Belyanin, "Generation of picosecond pulses and frequency combs in actively mode locked external

- ring cavity quantum cascade lasers," *Appl. Phys. Lett.*, vol. 103, no. 23, 2013.
- [82] Y. Wang and A. Belyanin, "Active mode-locking of mid-infrared quantum cascade lasers with short gain recovery time," *Opt. Express*, vol. 23, no. 4, p. 4173, 2015.
- [83] R. H. Dicke, "Coherence in spontaneous radiation processes," *Phys. Rev.*, vol. 93, no. 1, pp. 99–110, 1954.
- [84] D. L. Boiko and P. P. Vasil'ev, "Longitudinal polariton condensation and superradiant emission in semiconductor edge-emitting laser structures," *arXiv: 1112.1298*, 2011.
- [85] G. Timothy Noe *et al.*, "Giant superfluorescent bursts from a semiconductor magneto-plasma," *Nat. Phys.*, vol. 8, no. 3, pp. 219–224, 2012.
- [86] P. P. Vasil'ev, "Femtosecond superradiant emission in inorganic semiconductors," *Reports Prog. Phys.*, vol. 72, no. 7, p. 76501, 2009.
- [87] M. Xia, R. V. Penty, I. H. White, and P. P. Vasil'ev, "Femtosecond superradiant emission in AlGaInAs quantum-well semiconductor laser structures," *Opt. Express*, vol. 20, no. 8, p. 8755, 2012.
- [88] V. F. Olle, P. P. Vasil'ev, a. Wonfor, R. V. Penty, and I. H. White, "Ultrashort superradiant pulse generation from a GaN/InGaN heterostructure," *Opt. Express*, vol. 20, no. 7, p. 7035, 2012.
- [89] D. L. Boiko *et al.*, "Superfluorescent emission in electrically pumped semiconductor laser," *arXiv:1302.0263*, pp. 1–19, 2013.
- [90] F. T. Arecchi and E. Courtens, "Cooperative phenomena in resonant electromagnetic propagation," *Phys. Rev. A*, vol. 2, no. 5, pp. 1730–1737, 1970.
- [91] N. Vukovic, J. Radovanovic, V. Milanovic, and D. L. Boiko, "The Role of Carrier Diffusion in RNGH Instabilities of Quantum Cascade Lasers," in *2015 European Conference on Lasers and Electro-Optics - European Quantum Electronics Conference, 2015*, p. EF_P_10.
- [92] L. Kappei, "Dynamics and coherent effects of high density plasmas in semiconductor nanostructures," EPFL Lausanne, 2005.
- [93] A. A. Belyanin, V. V. Kocharovskiy, V. V. Kocharovskiy, and D. S. Pestov, "Novel schemes

- and prospects of superradiant lasing in heterostructures," *Laser Phys.*, vol. 13, pp. 161–167, 2003.
- [94] N. Vukovic, J. Radovanovic, V. Milanovic, and D. L. Boiko, "Determination of RNGH round-trip gain using bi-orthogonal perturbation approach," in *International School and Conference on Photonics - PHOTONICA2015*, 2015, p. 126.
- [95] P. M. Morse and H. Feshbach, *Methods of theoretical physics*. New York: McGraw-Hill, 1953.
- [96] D. L. Boiko, "Paraxial Hamiltonian for photons in two-dimensional photonic crystal microstructures," *arXiv Prepr. arXiv0710.5287*, 2007.
- [97] A. A. Antonov *et al.*, "Tailoring Risken-Nummedal-Graham-Haken Instability in Quantum Cascade Lasers," in *2017 European Conference on Lasers and Electro-Optics and European Quantum Electronics Conference*, 2017, p. CC_P_4.
- [98] N. N. Vukovic, J. Radovanovic, V. Milanovic, and D. L. Boiko, "Regular self-pulsations in external cavity mid-IR Fabry-Pérot quantum cascade lasers," manuscript under preparation, 2018.
- [99] L. Jumpertz, M. Carras, K. Schires, and F. Grillot, "Regimes of external optical feedback in 5.6 μ m distributed feedback mid-infrared quantum cascade lasers," *Appl. Phys. Lett.*, vol. 105, no. 13, p. 131112, 2014.
- [100] L. Jumpertz, K. Schires, M. Carras, M. Sciamanna, and F. Grillot, "Chaotic light at mid-infrared wavelength," *Light Sci. Appl.*, vol. 5, no. 6, p. e16088, 2016.
- [101] G. Friart, G. Van der Sande, G. Verschaffelt, and T. Erneux, "Analytical stability boundaries for quantum cascade lasers subject to optical feedback," *Phys. Rev. E*, vol. 93, no. 5, p. 52201, 2016.
- [102] F. P. Mezzapesa *et al.*, "Intrinsic stability of quantum cascade lasers against optical feedback," *Opt. Express*, vol. 21, no. 11, p. 13748, 2013.
- [103] L. L. Columbo and M. Brambilla, "Multimode regimes in quantum cascade lasers with optical feedback," *Opt. Express*, vol. 22, no. 9, p. 10105, 2014.
- [104] G. Agnew *et al.*, "Model for a pulsed terahertz quantum cascade laser under optical

- feedback," *Opt. Express*, vol. 24, no. 18, p. 20554, 2016.
- [105] R. W. Tkach and A. R. Chraplyvy, "Regimes of feedback effects in 1.5- μ m distributed feedback lasers," *J. Light. Technol.*, vol. 4, no. 11, pp. 1655–1661, 1986.
- [106] L. Jumpertz, S. Ferré, K. Schires, M. Carras, and F. Grillot, "Nonlinear dynamics of quantum cascade lasers with optical feedback," in *Quantum Sensing and Nanophotonic Devices XII*, 2015, vol. 9370, p. 937014.
- [107] D. M. Kane and K. A. Shore, *Unlocking dynamical diversity: optical feedback effects on semiconductor lasers*. John Wiley & Sons, 2005.
- [108] L. Jumpertz, *Nonlinear Photonics in Mid-infrared Quantum Cascade Lasers*. Cham: Springer International Publishing, 2017.
- [109] J.-F. Kischkat, "External Cavity Quantum Cascade Lasers," Humboldt-Universität zu Berlin, Mathematisch-Naturwissenschaftliche Fakultät, 2015.
- [110] N. Vuković, "Travelling wave model for external cavity QCL," in *SKIN AND TISSUE CANCER DETECTION USING LASER IMAGING The Book of Scientific Reports*, 1st ed., Ž. Cvejić, J. Radovanović, and D. Indjin, Eds. Novi Sad, Serbia: Liberte, 2017, pp. 242–245.
- [111] L. Mashal, G. Van der Sande, L. Gelens, J. Danckaert, and G. Verschaffelt, "Square-wave oscillations in semiconductor ring lasers with delayed optical feedback," *Opt. Express*, vol. 20, no. 20, p. 22503, 2012.
- [112] M. G. Benedict, *Super-radiance: Multiatomic coherent emission*. CRC Press, 1996.
- [113] M. A. Little, P. E. McSharry, S. J. Roberts, D. A. E. Costello, and I. M. Moroz, "Exploiting Nonlinear Recurrence and Fractal Scaling Properties for Voice Disorder Detection," *Biomed. Eng. Online*, vol. 6, no. 1, p. 23, 2007.
- [114] H. Kantz and T. Schreiber, *Nonlinear time series analysis*, vol. 7. Cambridge university press, 2004.
- [115] J. B. Khurgin, Y. Dikmelik, A. Hugi, and J. Faist, "Coherent frequency combs produced by self frequency modulation in quantum cascade lasers," *Appl. Phys. Lett.*, vol. 104, no. 8, p. 81118, 2014.
- [116] G. Villares and J. Faist, "Quantum cascade laser combs: effects of modulation and

- dispersion," *Opt. Express*, vol. 23, no. 2, p. 1651, 2015.
- [117] P. Tzenov, D. Burghoff, Q. Hu, and C. Jirauschek, "Time domain modeling of terahertz quantum cascade lasers for frequency comb generation," *Opt. Express*, vol. 24, no. 20, p. 23232, 2016.
- [118] F. Kärtner, "Pulse Characterization," in *6.977 Ultrafast Optics*, Massachusetts Institute of Technology: MIT OpenCourseWare, <https://ocw.mit.edu>, 2005, pp. 333–370.
- [119] J.-C. Diels, J. J. Fontaine, and F. Simoni, "Phase sensitive measurements of femtosecond laser pulses from a ring cavity," in *Lasers' 83; Proceedings of the International Conference*, 1983, pp. 348–355.
- [120] J.-C. M. Diels, J. J. Fontaine, I. C. McMichael, and F. Simoni, "Control and measurement of ultrashort pulse shapes (in amplitude and phase) with femtosecond accuracy," *Appl. Opt.*, vol. 24, no. 9, pp. 1270–1282, 1985.
- [121] A. Zavriyev, H. C. Liu, Z. Biglov, E. Dupont, and P. B. Corkum, "Direct autocorrelation measurements of mid-infrared picosecond pulses by quantum-well devices," *Opt. Lett.*, vol. 20, no. 18, pp. 1886–1888, 1995.
- [122] T. Maier, H. Schneider, M. Walther, P. Koidl, and H. C. Liu, "Resonant two-photon photoemission in quantum-well infrared photodetectors," *Appl. Phys. Lett.*, vol. 84, no. 25, pp. 5162–5164, 2004.
- [123] C. Y. Wang, "Multimode dynamics in Quantum Cascade Lasers: from coherent instability to mode locking," Harvard University, 2008.
- [124] M. Little, P. McSharry, I. Moroz, and S. Roberts, "Nonlinear, Biophysically-Informed Speech Pathology Detection," in *2006 IEEE International Conference on Acoustics Speed and Signal Processing Proceedings*, 2006, vol. 2, p. II-1080-II-1083.
- [125] E. G. Altmann and H. Kantz, "Recurrence time analysis, long-term correlations, and extreme events," *Phys. Rev. E*, vol. 71, no. 5, p. 56106, 2005.
- [126] D. P. Lathrop and E. J. Kostelich, "Characterization of an experimental strange attractor by periodic orbits," *Phys. Rev. A*, vol. 40, no. 7, pp. 4028–4031, 1989.
- [127] J. Stark, D. S. Broomhead, M. E. Davies, and J. Huke, "Delay Embeddings for Forced Systems. II. Stochastic Forcing," *J. Nonlinear Sci.*, vol. 13, no. 6, pp. 519–577, 2003.

Appendix A

Maxwell-Bloch equations

When the precise state of the system is unknown, the density matrix formalism can be used to describe the system in a statistical sense. The diagonal elements ρ_{nn} give the probability that the system is in energy eigenstate n . The off-diagonal elements ρ_{nm} give the “coherence” between levels n and m , in the sense that ρ_{nm} will be nonzero only if the system is in a coherent superposition of energy eigenstate n and m [62]. The off-diagonal elements of the density matrix are (in certain circumstances) proportional to the induced electric dipole moment of the atom.

Time evolution of density matrix elements (without collision terms) is given by the following equation [62]:

$$\partial_t \rho_{nm} = \frac{-i}{\hbar} \left[\hat{H}, \hat{\rho} \right]_{nm}, \quad (\text{A.1})$$

where $\hat{\rho}$ and \hat{H} are the density matrix and Hamiltonian operators respectively. Collisions between atoms are included in the formalism by adding phenomenological damping terms to the Eq. (A.1):

$$\partial_t \rho_{nm} = \frac{-i}{\hbar} \left[\hat{H}, \hat{\rho} \right]_{nm} - \gamma_{nm} (\rho_{nm} - \rho_{nm}^{(eq)}) + D \partial_z^2 \rho_{nm} \quad (\text{A.2})$$

where the second term on the right-hand side is a phenomenological damping term, which indicates that ρ_{nm} relaxes to its equilibrium value $\rho_{nm}^{(eq)}$ at rate γ_{nm} . Since γ_{nm} is a decay rate, we assume that $\gamma_{nm} = \gamma_{mn}$. In addition, we make the physical assumption that $\rho_{nm}^{(eq)} = 0$ for $n \neq m$ which means that in thermal equilibrium the excited states of the system may contain population ($\rho_{mm}^{(eq)}$ can be nonzero) but that thermal excitation, which is expected to be an incoherent process, cannot produce any coherent superpositions of atomic states. In addition, the third term on the right-hand side is due to diffusion and it is also added phenomenologically according to [63].

We will now apply the density matrix formalism to the simple case in which only the two atomic states “a” (lower atomic level) and “b” (upper level) interact appreciably with the incident optical field. The density matrix describing the atom is the two-by-two matrix:

$$\hat{\rho} = \begin{bmatrix} \rho_{aa} & \rho_{ab} \\ \rho_{ba} & \rho_{bb} \end{bmatrix}, \quad (\text{A.3})$$

where $\rho_{ab} = \rho_{ba}^*$. The matrix representation of the dipole moment operator reads:

$$\hat{\mu} = \begin{bmatrix} 0 & \mu_{ab} \\ \mu_{ba} & 0 \end{bmatrix} = \begin{bmatrix} 0 & \mu \\ \mu & 0 \end{bmatrix} \quad (\text{A.4})$$

where $\mu_{ij} = \mu_{ji}^* = -e \langle i | \hat{z} | j \rangle$, $-e$ is the electron charge and \hat{z} is the position operator for the electron. Diagonal elements of the dipole moment operator are equal to zero because we assume that “a” and “b” have definite parity, in which case diagonal elements vanish as a consequence of symmetry.

The expectation value of the dipole moment is according given by [62]:

$$\overline{\langle \hat{\mu} \rangle} = \text{tr}(\hat{\rho} \hat{\mu}) = \text{tr} \left(\begin{bmatrix} \rho_{aa} & \rho_{ab} \\ \rho_{ba} & \rho_{bb} \end{bmatrix} \begin{bmatrix} 0 & \mu \\ \mu & 0 \end{bmatrix} \right) = \mu(\rho_{ba} + \rho_{ba}^*), \quad (\text{A.5})$$

where “tr” denotes the trace operator. From (A.5) we see that the expectation value of the dipole moment depends upon the off-diagonal elements of the density matrix. The polarization of a medium is defined as:

$$\tilde{P} = N \overline{\langle \hat{\mu} \rangle} = N \mu (\rho_{ab}^* + \rho_{ab}). \quad (\text{A.6})$$

Hamiltonian for this system is given by $\hat{H} = \hat{H}_0 + \hat{V}(t)$ where \hat{H}_0 is the atomic Hamiltonian and $\hat{V}(t)$ represents the energy of interaction of the atom with the electromagnetic field. The energies of the states “a” and “b” are $E_a = \hbar \omega_a$ and $E_b = \hbar \omega_b$ respectively while the transition frequency is denoted by $\omega_{ba} = (E_b - E_a) / \hbar$. We assume that the interaction energy can be adequately described in the electric dipole approximation, in which case the interaction Hamiltonian has the form [62]:

$$\hat{V}(t) = -\hat{\mu} \tilde{E}(t) \quad (\text{A.7})$$

The only nonvanishing elements of $\hat{V}(t)$ are V_{ba} and V_{ab} which are given explicitly by:

$$V_{ba} = V_{ab}^* = -\mu \tilde{E}(t) \quad (\text{A.8})$$

Upper level “b” decays to the lower level “a” at a rate Γ_{ba} and therefore the lifetime of the upper level $T_1 = 1/\Gamma_{ba}$. Typically, the decay of the upper level would be due to spontaneous emission. We also assume that the atomic dipole moment is dephased in the characteristic time T_2 , leading to a transition linewidth (for weak applied fields) of characteristic width $\gamma_{ba} = 1/T_2$.

Using Eq. (A.2) in which indices m and n can take values a or b only, after some algebra we get for an *open two-level system*:

$$\begin{aligned}\partial_t \rho_{ba} &= -i\omega_{ba} \rho_{ba} - \frac{i\mu\tilde{E}(t)}{\hbar} (\rho_{bb} - \rho_{aa}) - \frac{1}{T_2} \rho_{ba} + D\partial_z^2 \rho_{ba} \\ &= -i\omega \rho_{ba} - \frac{i\mu\tilde{E}(t)}{\hbar} \Delta - \frac{1}{T_2} \rho_{ba} + D\partial_z^2 \rho_{ba}\end{aligned}\quad (\text{A.9})$$

$$\partial_t \rho_{bb} = \lambda_b - \frac{i\mu\tilde{E}(t)}{\hbar} (\rho_{ab} - \rho_{ba}) - \frac{\rho_{bb} - \rho_{bb}^{(eq)}}{T_1} + D\partial_z^2 \rho_{bb} \quad (\text{A.10})$$

$$\partial_t \rho_{aa} = \lambda_a - \frac{i\mu\tilde{E}(t)}{\hbar} (\rho_{ab} - \rho_{ba}) - \frac{\rho_{aa} - \rho_{aa}^{(eq)}}{T_1} + D\partial_z^2 \rho_{aa} \quad (\text{A.11})$$

Where λ_a, λ_b are pumping rates and we have used $\omega_{ba} = \omega$ and $\Delta = \rho_{bb} - \rho_{aa}$.

Since $\rho_{ab} = \rho_{ba}^*$, from (A.9) we get:

$$\partial_t \rho_{ab} = \partial_t \rho_{ba}^* = i\omega \rho_{ab} + \frac{i\mu\tilde{E}(t)}{\hbar} \Delta - \frac{1}{T_2} \rho_{ab} + D\partial_z^2 \rho_{ab} \quad (\text{A.12})$$

Thus we have derived Eq. (2.1) from the manuscript. From (A.10) and (A.11) by subtraction we get:

$$\partial_t \Delta = \frac{2i\mu\tilde{E}(t)}{\hbar} (\rho_{ab} - \rho_{ba}) - \frac{\Delta - \Delta_{pump}}{T_1} + D\partial_z^2 \Delta \quad (\text{A.13})$$

Where Δ_{pump} is Δ at steady state when $E=0$ (steady state inversion which characterizes the pumping rate). Equation (A.13) coincides with Eq. (2.2) from the main text. Equations (A.12) and (A.13) define an open two-level system meaning that the total number of electrons in the system is not conserved (it can flow in and out and vary depending on the bias) [62].

From (A.5), using (A.9) and (A.12) we get:

$$\partial_t \langle \widehat{\mu} \rangle = \mu \partial_t (\rho_{ba} + \rho_{ab}) = i\omega\mu(\rho_{ab} - \rho_{ba}) - \frac{1}{T_2} \langle \widehat{\mu} \rangle + D\partial_z^2 \langle \widehat{\mu} \rangle \quad (\text{A.14})$$

The electric field \bar{E} is written by a time-dependent Maxwell equation as:

$$\nabla^2 \bar{E}(z, t) - \frac{1}{c^2} \partial_t^2 (\varepsilon \bar{E}(z, t)) = \mu_0 \partial_t^2 \bar{P}(z, t) \quad (\text{A.15})$$

where \bar{P} is the polarization vector of matter, ε is the electric permittivity tensor, c is the speed of light in vacuum, and μ_0 is the magnetic permeability in vacuum. If we assume a uniform refractive index n_g of the laser medium and linearly polarized spatial modes for the x and y directions with the propagation for the z axis, the field and the polarization of matter reduce to scalar quantities propagating only to the z direction and (A.15) can be reduced to the following scalar equation:

$$\partial_z^2 \tilde{E} - \frac{n_g^2}{c^2} \partial_t^2 \tilde{E} = \Gamma \frac{N\mu}{\varepsilon_0 c^2} \partial_t^2 (\rho_{ab}^* + \rho_{ab}) \quad (\text{A.16})$$

where we have used (A.6) and accounted for optical mode confinement via factor Γ . Note that on the right hand side we can include $(n_g l'_0 / c) \partial_t E$ where l'_0 is a linear loss coefficient, in order to include losses and then we have recovered Eq. (2.3).

In the literature there are different models essentially based on MB equations in two or three-level approximation [26], [39], [45], [81], [115]–[117] where in some cases additional effects such as cubic nonlinearity, saturable absorption and cavity dispersion have been added phenomenologically to provide a proper interpretation of the experiments.

Appendix B

Adiabatic approximation test

In this appendix we consider adiabatic-following approximation that applies to *bidirectional ring lasers* operating on two counter-propagating waves or single-mode *FP cavity lasers*. In these lasers, the standing wave pattern of the field in the cavity leads to the spatial hole burning in the distribution of population inversion. At the same time, our considerations presented below do not apply for a single-frequency *unidirectional ring laser* from Refs. [30], [31] because there is no standing wave pattern in the cavity of such laser and associated with it spatial hole burning effect.

The adiabatic-following approximation for the medium polarization is valid when the polarization dynamics is slow and follows instantaneously the optical field in the cavity [32]. For solid state lasers, including semiconductor LDs and QCLs, the dephasing time T_2 is much smaller than the relaxation T_1 . Therefore under adiabatic-following approximation, the behavior of these systems fall into Class-B laser dynamics. These dynamical systems are very well studied, including the cases with mode coupling due to back-scattering and induced population grating. One example can be found in a review [65].

In order to obtain the adiabatic-following approximation for our coupled-mode system (2.7)-(2.11), we set the time derivatives in Eqs. (2.8) and (2.9) to

zero, yielding the following instantaneous amplitudes of polarization grating harmonics:

$$\eta_{\pm} = \frac{i\mu}{2\hbar} (E_{\pm}\Delta_0 + E_{\mp}\Delta_2^{\mp}) T_2 \quad (\text{B.1})$$

$$\eta_{\pm\pm} = \frac{i\mu}{2\hbar} (E_{\pm}\Delta_{\mp}) T_{2_g} \quad (\text{B.2})$$

where for the purpose of this test we have excluded the diffusion terms, assuming that $T_{2_eff} = T_{2_g} = T_2$, and $T_g = T_1$. Substituting these in Eqs. (2.7), (2.9) and (2.10), we find that

$$\frac{n}{c} \partial_t E_{\pm} = \mp \partial_z E_{\pm} + \frac{NT_{2_eff} \mu^2 \Gamma \omega}{2c\hbar n \epsilon_0} (E_{\pm}\Delta_0 + E_{\mp}\Delta_2^{\mp}) - \frac{1}{2} l_0 E_{\pm} \quad (\text{B.3})$$

$$\begin{aligned} \partial_t (\Delta_0 + \Delta_2^+ e^{2ikz} + \Delta_2^- e^{-2ikz}) &= \frac{\Delta_{pump}}{T_1} \\ - \frac{\Delta_0 + \Delta_2^+ e^{2ikz} + \Delta_2^- e^{-2ikz}}{T_1} &\left[1 + a \left((E_-^* E_- + E_+^* E_+) + 2 \text{Re}(E_-^* E_+ e^{-2ikz}) \right) \right] \end{aligned} \quad (\text{B.4})$$

where we have introduced the saturation parameter $a = T_1 T_2 \mu^2 / \hbar^2$. This system of equations is in perfect agreement with the well-known Class-B laser model (e.g. see Eqs. (1.10) and (1.11) in Ref. [65]). In contrast to our coupled-mode expansion, the adiabatic approximation that follows from the equations (8)-(10) of Ref. [39] disagrees with the well-established coupled-mode model for a Class-B laser.

Appendix C

Interferometric autocorrelation

In this appendix we will describe the meaning of interferometric autocorrelation following along the lines of Ref. [118]. For characterization of ultrashort laser pulses that are shorter than 20 ps, usually some type of autocorrelation or crosscorrelation in the optical domain using nonlinear optical effects has to be performed, which means that the pulse itself has to be used to measure its width, since there are no other controllable events available on such short time scales [118].

Pulse duration measurements using second-harmonic *intensity autocorrelation* is a standard method for pulse characterisation. The input pulse is split in two, and one of the pulses is delayed by τ . The two pulses are focused into a nonlinear optical crystal in a non-collinear fashion.

Interferometric autocorrelation which is introduced by J. C. Diels [119], [120] is a pulse characterization method, that besides the pulse duration also reveals the phase of the pulse. The input beam is again split into two and one of them is delayed. In the standard setup, once recombined, the two pulses are sent collinearly first into a nonlinear crystal, and then a filter, which allows only the second-harmonic generation (SHG) component to be detected.

The total field after the Michelson-Interferometer is given by the two identical pulses delayed by τ with respect to each other:

$$E(t, \tau) = E(t + \tau) + E(t) = A(t + \tau)e^{i\omega_0(t+\tau)}e^{i\varphi_{CE}} + A(t)e^{i\omega_0 t}e^{i\varphi_{CE}} \quad (C.1)$$

Here $A(t)$ is the complex amplitude, the term $e^{i\omega_0 t}$ describes the oscillation with the carrier frequency ω_0 and φ_{CE} is the carrier-envelope phase. The induced nonlinear polarization $P^{(2)}(t)$ satisfies the following relation [118]:

$$P^{(2)}(t) \propto E(t) \cdot E(t - \tau) \propto \left(A(t + \tau)e^{i\omega_0(t+\tau)}e^{i\varphi_{CE}} + A(t)e^{i\omega_0 t}e^{i\varphi_{CE}} \right)^2. \quad (C.2)$$

The radiated second harmonic electric field is proportional to the polarization

$$E(t, \tau) \propto \left(A(t + \tau)e^{i\omega_0(t+\tau)}e^{i\varphi_{CE}} + A(t)e^{i\omega_0 t}e^{i\varphi_{CE}} \right)^2 \quad (C.3)$$

The photo – detector integrates over the envelope of each individual pulse

$$\begin{aligned} I(\tau) \propto \int_{-\infty}^{+\infty} [& |A(t + \tau)|^4 + 4|A(t + \tau)|^2 |A(t)|^2 + |A(t)|^4 \\ & + 2A(t + \tau)|A(t)|^2 A^*(t)e^{i\omega_0 \tau} + c.c. \\ & + 2A(t)|A(t + \tau)|^2 A^*(t + \tau)e^{-i\omega_0 \tau} + c.c. \\ & + A^2(t + \tau)(A^*(t))^2 e^{i2\omega_0 \tau} + c.c.] dt \end{aligned} \quad (C.4)$$

The interferometric autocorrelation function is composed of the following terms:

$$I(\tau) = I_{back} + I_{int}(\tau) + I_{\omega}(\tau) + I_{2\omega}(\tau) \quad (C.5)$$

Background signal I_{back} :

$$I_{back} = \int_{-\infty}^{+\infty} \left(|A(t + \tau)|^4 + |A(t)|^4 \right) dt = 2 \int_{-\infty}^{+\infty} I^2(t) dt \quad (C.6)$$

Intensity autocorrelation (measured by non-colinear SHG) $I_{\text{int}}(\tau)$:

$$I_{\text{int}}(\tau) = 4 \int_{-\infty}^{+\infty} |A(t+\tau)|^2 |A(t)|^2 dt = 4 \int_{-\infty}^{+\infty} I(t+\tau) \cdot I(t) dt \quad (\text{C.7})$$

Coherence term oscillating with ω_0 , $I_{\omega}(\tau)$:

$$I_{\omega}(\tau) = 4 \int_{-\infty}^{+\infty} \text{Re} \left[(I(t) + I(t+\tau)) A^*(t) A(t+\tau) e^{i\omega_0 \tau} \right] dt \quad (\text{C.8})$$

Coherence term oscillating with $2\omega_0$, $I_{2\omega}(\tau)$:

$$I_{2\omega}(\tau) = 2 \int_{-\infty}^{+\infty} \text{Re} \left[A^2(t) (A^*(t+\tau))^2 e^{i2\omega_0 \tau} \right] dt \quad (\text{C.9})$$

We can normalize (C.5) relative to the background intensity I_{back} resulting in the interferometric autocorrelation trace [118]:

$$I_{\text{IAC}}(\tau) = 1 + \frac{I_{\text{int}}(\tau)}{I_{\text{back}}} + \frac{I_{\omega}(\tau)}{I_{\text{back}}} + \frac{I_{2\omega}(\tau)}{I_{\text{back}}} \quad (\text{C.10})$$

At $\tau = 0$ integrals in (C.10) take the following values:

$$I_{\text{back}} = 2 \int_{-\infty}^{+\infty} |A(t)|^4 dt \quad (\text{C.11})$$

$$I_{\text{int}}(\tau = 0) = 4 \int_{-\infty}^{+\infty} |A(t)|^4 dt = 2I_{\text{back}} \quad (\text{C.12})$$

$$I_{\omega}(\tau = 0) = 8 \int_{-\infty}^{+\infty} |A(t)|^4 dt = 4I_{\text{back}} \quad (\text{C.13})$$

$$I_{2\omega}(\tau) = 2 \int_{-\infty}^{+\infty} |A(t)|^4 dt = I_{\text{back}} \quad (\text{C.14})$$

Leading to the interferometric autocorrelation (C.10) at zero time delay:

$$I_{LAC}(\tau)|_{\max} = I_{LAC}(0) = 8 \quad (\text{C.15})$$

While $I_{LAC}(\tau \rightarrow \pm\infty) = 1$ and $I_{LAC}(\tau)|_{\min} = 0$.

If $E(t)$ is an isolated pulse that is nonzero only over an interval T , then for $\tau > T$ all terms in (C.6)-(C.10) which include both τ and $\tau+T$ vanish leading $I_{LAC}(\tau > T) = 1$ meaning that for in isolated pulse $I_{LAC}(0) / I_{LAC}(\tau > T) = 8$.

In case that $E(t)$ is a complex stationary random process whose phase at each point in time is uniformly distributed over $[0, 2\pi]$ and assume that for $\tau > T$ $E(t)$ and $E(t+\tau)$ are statistically independent, then the mean value of the terms in (C.10) containing $e^{i\omega_0\tau}$ and $e^{i2\omega_0\tau}$ is zero and (C.10) averages to 3. Therefore, for modes with completely random phases $I_{LAC}(0) / I_{LAC}(\tau > T) = 8:3$ [39].

Note that in [39] due to the extremely low SHG conversion efficiency of nonlinear crystals in the MIR, the standard setup was not feasible, and in order to overcome this problem authors used a two-photon quantum well infrared photodetector [121], [122] instead of using a nonlinear crystal plus a linear detector. For further details about the experimental setup see [39], [123].

Appendix D

The purpose of this Appendix is to clarify to an interested reader the origin of Eqs. (4.2)-(4.4) from the Section 4.1 of the main text.

Let us consider a biorthogonal set of basis vectors $|V_i\rangle, \langle U_k|$ which fulfill condition $\langle U_k|V_i\rangle = A_{ik}\delta_{ik}$ where δ_{ik} is Kronecker delta and A_{ik} is a constant (vectors are orthogonal but not normalized to 1). We will use Dirac notation, i.e. $\langle U_i|M|V_k\rangle = [U_i]^\dagger \cdot \|M\| \cdot V_k$.

We consider the following eigenproblem:

$$M|V_i\rangle = \Lambda_i|V_i\rangle \quad (\text{D.1})$$

and use the following expansions:

$$\begin{aligned} M &= M^{(0)} + M^{(1)} \\ |V_i\rangle &= |V_i^{(0)}\rangle + |V_i^{(1)}\rangle \\ |U_k\rangle &= |U_k^{(0)}\rangle + |U_k^{(1)}\rangle \\ \Lambda_i &= \Lambda_i^{(0)} + \Lambda_i^{(1)} + \Lambda_i^{(2)} \end{aligned} \quad (\text{D.2})$$

where M,V and U are vectors and Λ eigenvalue of matrix M. Vectors V have the meaning of eigenvectors of matrix M, while U are eigenvectors of matrix M^\dagger . Matrix $M^{(0)}$ is an unperturbed matrix and $M^{(1)}$ is perturbation matrix.

Superscripts (0), (1) and (2) in (D.2) thus stand for the unperturbed case, first order perturbation and second order perturbation respectively.

Combining (D.1) and (D.2) results in:

$$(M^{(0)} + M^{(1)})|V_i^{(0)} + V_i^{(1)}\rangle - (\Lambda_i^{(0)} + \Lambda_i^{(1)} + \Lambda_i^{(2)})|V_i^{(0)} + V_i^{(1)}\rangle = 0 \quad (D.3)$$

The last expression is then expanded in the following manner:

$$\begin{aligned} & M^{(0)}|V_i^{(0)}\rangle - \Lambda_i^{(0)}|V_i^{(0)}\rangle + M^{(1)}|V_i^{(0)}\rangle - \Lambda_i^{(1)}|V_i^{(0)}\rangle + M^{(0)}|V_i^{(1)}\rangle - \Lambda_i^{(0)}|V_i^{(1)}\rangle - \Lambda_i^{(1)}|V_i^{(0)}\rangle + \\ & M^{(1)}|V_i^{(1)}\rangle - \Lambda_i^{(1)}|V_i^{(1)}\rangle - \Lambda_i^{(2)}|V_i^{(0)}\rangle = 0 \end{aligned} \quad (D.4)$$

At this point we will use the standard procedure to represent the perturbation vectors $|V_i^{(1)}\rangle$ using the unperturbed basis vectors $|V_i^{(0)}\rangle$:

$$|V_i^{(1)}\rangle = \sum_{i \neq m} c_{im}^{(1)} |V_m^{(0)}\rangle, \quad c_{ii}^{(1)} = 0 \quad (D.5)$$

For convenience, from now on we will drop the superscript (1) from the expansion coefficient, i.e. we will adopt $c_{im}^{(1)} \equiv c_{im}$.

When we multiply Eq. (D.4) with $\langle U_k^{(0)}|$ from the left, we get:

$$\begin{aligned} & (\Lambda_k^{(0)} - \Lambda_i^{(0)})\langle U_k^{(0)}|V_i^{(0)}\rangle + \langle U_k^{(0)}|M^{(1)}|V_i^{(0)}\rangle - \Lambda_i^{(1)}\langle U_k^{(0)}|V_i^{(0)}\rangle \\ & + \sum_{i \neq m} c_{im} \langle U_k^{(0)}|M^{(0)}|V_m^{(0)}\rangle - \sum_{i \neq m} \Lambda_i^{(0)} c_{im} \langle U_k^{(0)}|V_m^{(0)}\rangle \\ & + \sum_{i \neq m} c_{im} \langle U_k^{(0)}|M^{(1)}|V_m^{(0)}\rangle - \sum_{i \neq m} \Lambda_i^{(1)} c_{im} \langle U_k^{(0)}|V_m^{(0)}\rangle - \Lambda_i^{(2)}\langle U_k^{(0)}|V_i^{(0)}\rangle \end{aligned} \quad (D.6)$$

Note that the first term $(\Lambda_k^{(0)} - \Lambda_i^{(0)})\langle U_k^{(0)}|V_i^{(0)}\rangle$ is obviously always equal to zero.

Let us consider first that $k \neq i$ and first order perturbation terms:

$$\langle U_k^{(0)} | M^{(1)} | V_i^{(0)} \rangle - \Lambda_i^{(1)} \langle U_k^{(0)} | V_i^{(0)} \rangle + \sum_{i \neq m} c_{im} \langle U_k^{(0)} | M^{(0)} | V_m^{(0)} \rangle - \sum_{i \neq m} \Lambda_i^{(0)} c_{im} \langle U_k^{(0)} | V_m^{(0)} \rangle = 0 .$$

(D.7)

Since $k \neq i$, the term $\Lambda_i^{(1)} \langle U_k^{(0)} | V_i^{(0)} \rangle$ is equal to zero because of orthogonality. Further transformation of the above expression (D.7) using orthogonality results in:

$$\langle U_k^{(0)} | M^{(1)} | V_i^{(0)} \rangle + c_{ik} (\Lambda_k^{(0)} - \Lambda_i^{(0)}) \langle U_k^{(0)} | V_k^{(0)} \rangle = 0 ,$$

(D.8)

from which we obtain the expansion coefficients c_{ik} :

$$c_{ik} = \frac{\langle U_k^{(0)} | M^{(1)} | V_i^{(0)} \rangle}{(\Lambda_i^{(0)} - \Lambda_k^{(0)}) \langle U_k^{(0)} | V_k^{(0)} \rangle}, k \neq i .$$

(D.9)

In case when $k = i$, we can write the first order perturbation terms as:

$$\langle U_i^{(0)} | M^{(1)} | V_i^{(0)} \rangle - \Lambda_i^{(1)} \langle U_i^{(0)} | V_i^{(0)} \rangle = 0 ,$$

(D.10)

from which we get first order perturbation expression for eigenvalue Λ_i :

$$\Lambda_i^{(1)} = \frac{\langle U_i^{(0)} | M^{(1)} | V_i^{(0)} \rangle}{\langle U_i^{(0)} | V_i^{(0)} \rangle}$$

(D.11)

We now need to determine the second order perturbation of eigenvalue Λ_i .

Using (D.6) we can write:

$$\sum_{i \neq m} c_{im} \langle U_k^{(0)} | M^{(1)} | V_m^{(0)} \rangle - \sum_{i \neq m} \Lambda_i^{(1)} c_{im} \langle U_k^{(0)} | V_m^{(0)} \rangle - \Lambda_i^{(2)} \langle U_k^{(0)} | V_i^{(0)} \rangle = 0 .$$

(D.12)

Since $k = i$, (D.12) reduces to:

$$\sum_{i \neq m} c_{im} \langle U_i^{(0)} | M^{(1)} | V_m^{(0)} \rangle - \Lambda_i^{(2)} \langle U_i^{(0)} | V_i^{(0)} \rangle = 0 ,$$

(D.13)

because the term $\sum_{i \neq m} \Lambda_i^{(1)} c_{im} \langle U_i^{(0)} | V_m^{(0)} \rangle$ is obviously zero.

Using Eq. (D.9) and Eq. (D.13) we can write:

$$\Lambda_i^{(2)} = \frac{\sum_{i \neq m} c_{im} \langle U_i^{(0)} | M^{(1)} | V_m^{(0)} \rangle}{\langle U_i^{(0)} | V_i^{(0)} \rangle} = \sum_{i \neq m} \frac{\langle U_m^{(0)} | M^{(1)} | V_i^{(0)} \rangle \langle U_i^{(0)} | M^{(1)} | V_m^{(0)} \rangle}{(\Lambda_i^{(0)} - \Lambda_m^{(0)}) \langle U_m^{(0)} | V_m^{(0)} \rangle \langle U_i^{(0)} | V_i^{(0)} \rangle} \quad (\text{D.14})$$

Finally, expression for eigenvalue Λ_i of the matrix M obtained from biorthogonal perturbation theory reads:

$$\begin{aligned} \Lambda_i &= \Lambda_i^{(0)} + \Lambda_i^{(1)} + \Lambda_i^{(2)} \\ &= \Lambda_i^{(0)} + \frac{\langle U_i^{(0)} | M^{(1)} | V_i^{(0)} \rangle}{\langle U_i^{(0)} | V_i^{(0)} \rangle} + \sum_{i \neq m} \frac{\langle U_m^{(0)} | M^{(1)} | V_i^{(0)} \rangle \langle U_i^{(0)} | M^{(1)} | V_m^{(0)} \rangle}{(\Lambda_i^{(0)} - \Lambda_m^{(0)}) \langle U_m^{(0)} | V_m^{(0)} \rangle \langle U_i^{(0)} | V_i^{(0)} \rangle}. \end{aligned} \quad (\text{D.15})$$

Thus we have derived Eq. (4.3) from the manuscript.

We will now apply (D.15) in our particular case when matrices M , $M^{(0)}$ and $M^{(1)}$ are given by (4.1) and determine the eigenvalue Λ with the largest real part. For convenience, we will rewrite (4.1) in the following form:

$$\|M\| = \|M^{(0)}\| + \|M^{(1)}\| = \begin{bmatrix} -\gamma_{2,eff} & -\frac{\gamma_{2,eff}(2\nu_0 - 1)}{2} & \frac{E}{2} & 0 \\ -\gamma_p & -\frac{\gamma_p}{2} - i\Omega & 0 & 0 \\ -2E & E \left[1 + (\nu_0 - 1) \frac{\gamma_{2,eff}}{\gamma_{2,g}} \right] & -\gamma_g & 2E \\ 0 & -\gamma_{2,eff} \frac{(\nu_0 - 1)}{2} & -\frac{E}{2} & -\gamma_{2,g} \end{bmatrix}, \quad (\text{D.16})$$

where we have used the following change of variables:

$$\gamma_{2,eff} = \frac{1}{T_{2,eff}}, \gamma_p = \frac{c}{n_g} l_0, \gamma_g = \frac{1}{T_g}, \gamma_{2,g} = \frac{1}{T_{2,g}}.$$

Unperturbed matrix is given by:

$$\|M^{(0)}\| = \begin{bmatrix} -\gamma_{2,eff} & -\frac{\gamma_{2,eff}(2\nu_0-1)}{2} & 0 & 0 \\ -\gamma_p & -\frac{\gamma_p}{2} - i\Omega & 0 & 0 \\ 0 & 0 & -\gamma_g & 2E \\ 0 & 0 & -\frac{E}{2} & -\gamma_{2,g} \end{bmatrix} \quad (D.17)$$

And perturbation matrix is:

$$\|M^{(1)}\| = \begin{bmatrix} 0 & 0 & \frac{E}{2} & 0 \\ 0 & 0 & 0 & 0 \\ -2E & E \left[1 + (\nu_0 - 1) \frac{\gamma_{2,eff}}{\gamma_{2,g}} \right] & 0 & 0 \\ 0 & -\gamma_{2,eff} \frac{(\nu_0 - 1)}{2} & 0 & 0 \end{bmatrix} \quad (D.18)$$

Eigenvalues of $\|M^{(0)}\|$ are then determined to be:

$$\Lambda^{(0)} = \begin{bmatrix} \Lambda_1^{(0)} \\ \Lambda_2^{(0)} \\ \Lambda_3^{(0)} \\ \Lambda_4^{(0)} \end{bmatrix} = \begin{bmatrix} -\frac{\gamma_+}{2} + \frac{\sqrt{\gamma_+^2 - \Omega^2 - 2i\gamma_- \Omega + 4\gamma_p \gamma_{2,eff}(\nu_0 - 1)}}{2} - \frac{i\Omega}{2} \\ -\frac{\gamma_+}{2} - \frac{\sqrt{\gamma_+^2 - \Omega^2 - 2i\gamma_- \Omega + 4\gamma_p \gamma_{2,eff}(\nu_0 - 1)}}{2} - \frac{i\Omega}{2} \\ \frac{-(\gamma_{2,g} + \gamma_g) + \sqrt{D_{34}}}{2} \\ \frac{-(\gamma_{2,g} + \gamma_g) - \sqrt{D_{34}}}{2} \end{bmatrix} \quad (D.19)$$

where we have introduced three more variables: $\gamma_+ = \gamma_{2,eff} + \frac{\gamma_p}{2}$, $\gamma_- = \gamma_{2,eff} - \frac{\gamma_p}{2}$

and $(\gamma_{2,g} - \gamma_g)^2 - 4E^2$.

Unperturbed eigenvectors $|V_i^{(0)}\rangle \equiv V_i^{(0)}$ of matrix $\|M^{(0)}\|$ corresponding to zeroth-order perturbation eigenvalues $\Lambda_i^{(0)}$ read:

$$V_1^{(0)} = \begin{bmatrix} \frac{\gamma_{2,\text{eff}}(2\nu_0 - 1)}{2} \\ -\frac{\gamma_-}{2} - \frac{\sqrt{\gamma_+^2 - \Omega^2 - 2i\gamma_- \Omega + 4\gamma_p \gamma_{2,\text{eff}}(\nu_0 - 1)}}{2} + \frac{i\Omega}{2} \\ 0 \\ 0 \end{bmatrix} \quad (\text{D.20})$$

$$V_2^{(0)} = \begin{bmatrix} \frac{\gamma_{2,\text{eff}}(2\nu_0 - 1)}{2} \\ -\frac{\gamma_-}{2} + \frac{\sqrt{\gamma_+^2 - \Omega^2 - 2i\gamma_- \Omega + 4\gamma_p \gamma_{2,\text{eff}}(\nu_0 - 1)}}{2} + \frac{i\Omega}{2} \\ 0 \\ 0 \end{bmatrix} \quad (\text{D.21})$$

$$V_3^{(0)} = \begin{bmatrix} 0 \\ 0 \\ 2E \\ \frac{\gamma_g - \gamma_{2,g} + \sqrt{D_{34}}}{2} \end{bmatrix} \quad (\text{D.22})$$

$$V_4^{(0)} = \begin{bmatrix} 0 \\ 0 \\ 2E \\ \frac{\gamma_g - \gamma_{2,g} - \sqrt{D_{34}}}{2} \end{bmatrix} \quad (\text{D.23})$$

Unperturbed eigenvectors $|U_i^{(0)}\rangle \equiv U_i^{(0)}$ of matrix $\|M^{(0)}\|^\dagger$ are found to be:

$$U_1^{(0)} = \begin{bmatrix} \gamma_p \\ -\frac{\gamma_-}{2} - \frac{\sqrt{\gamma_+^2 - \Omega^2 - 2i\gamma_- \Omega + 4\gamma_p \gamma_{2,eff}(\nu_0 - 1)}}{2} + \frac{i\Omega}{2} \\ 0 \\ 0 \end{bmatrix} \quad (D.24)$$

$$U_2^{(0)} = \begin{bmatrix} \gamma_p \\ -\frac{\gamma_-}{2} + \frac{\sqrt{\gamma_+^2 - \Omega^2 - 2i\gamma_- \Omega + 4\gamma_p \gamma_{2,eff}(\nu_0 - 1)}}{2} + \frac{i\Omega}{2} \\ 0 \\ 0 \end{bmatrix} \quad (D.25)$$

$$U_3^{(0)} = \begin{bmatrix} 0 \\ 0 \\ -E/2 \\ \frac{\gamma_g - \gamma_{2,g} + \sqrt{D_{34}}}{2} \end{bmatrix} \quad (D.26)$$

$$U_4^{(0)} = \begin{bmatrix} 0 \\ 0 \\ -E/2 \\ \frac{\gamma_g - \gamma_{2,g} - \sqrt{D_{34}}}{2} \end{bmatrix} \quad (D.27)$$

From (D.11) we can find that the first order perturbations $\Lambda_i^{(1)}$ are all zero:

$$\Lambda_i^{(1)} = \frac{\langle U_i^{(0)} | M^{(1)} | V_i^{(0)} \rangle}{\langle U_i^{(0)} | V_i^{(0)} \rangle} = \frac{[U_i^{(0)}]^\dagger \cdot \|M^{(1)}\| \cdot V_i^{(0)}}{[U_i^{(0)}]^\dagger \cdot V_i^{(0)}} = 0, \quad \text{for } i \in \{1, 2, 3, 4\}, \quad (D.28)$$

since the matrix products in the numerators are zero in all cases.

At this point we can easily find second order perturbations for all 4 eigenvalues, $\Lambda_i^{(2)}$, using (D.14) from above. Nevertheless, for the purpose of finding the RNGH instability threshold we are interested only in the

eigenvalue with the largest real part. It can be shown (see also Section 3.1) that it is the eigenvalue Λ_1 . Thus, for the sake of brevity, we will only write the expression $\Lambda_1^{(2)}$. From (D.14) it follows:

$$\begin{aligned}
\Lambda_1^{(2)} &= \frac{1}{\Lambda_1^{(0)} - \Lambda_2^{(0)}} \frac{[U_1^{(0)}]^\dagger \cdot \|M^{(1)}\| \cdot V_2^{(0)}}{[U_1^{(0)}]^\dagger \cdot V_1^{(0)}} \frac{[U_2^{(0)}]^\dagger \cdot \|M^{(1)}\| \cdot V_1^{(0)}}{[U_2^{(0)}]^\dagger \cdot V_2^{(0)}} \\
&+ \frac{1}{\Lambda_1^{(0)} - \Lambda_3^{(0)}} \frac{[U_1^{(0)}]^\dagger \cdot \|M^{(1)}\| \cdot V_3^{(0)}}{[U_1^{(0)}]^\dagger \cdot V_1^{(0)}} \frac{[U_3^{(0)}]^\dagger \cdot \|M^{(1)}\| \cdot V_1^{(0)}}{[U_3^{(0)}]^\dagger \cdot V_3^{(0)}} \\
&+ \frac{1}{\Lambda_1^{(0)} - \Lambda_4^{(0)}} \frac{[U_1^{(0)}]^\dagger \cdot \|M^{(1)}\| \cdot V_4^{(0)}}{[U_1^{(0)}]^\dagger \cdot V_1^{(0)}} \frac{[U_4^{(0)}]^\dagger \cdot \|M^{(1)}\| \cdot V_1^{(0)}}{[U_4^{(0)}]^\dagger \cdot V_4^{(0)}} \\
&= a_1 + b_1 + c_1
\end{aligned} \tag{D.29}$$

When we insert (D.19)-(D.27) in (D.29) we find:

$$a_1 = \frac{1}{\Lambda_1^{(0)} - \Lambda_2^{(0)}} \frac{[U_1^{(0)}]^\dagger \cdot \|M^{(1)}\| \cdot V_2^{(0)}}{[U_1^{(0)}]^\dagger \cdot V_1^{(0)}} \frac{[U_2^{(0)}]^\dagger \cdot \|M^{(1)}\| \cdot V_1^{(0)}}{[U_2^{(0)}]^\dagger \cdot V_2^{(0)}} = 0 \tag{D.30}$$

since the matrix product $[U_1^{(0)}]^\dagger \cdot \|M^{(1)}\| \cdot V_2^{(0)}$ is zero.

After some algebra we find b_1 and c_1 which can be expressed as:

$$b_1 = \left[\frac{\gamma_p E^2}{\Lambda_1^{(0)} + \frac{(\gamma_g + \gamma_{2-g}) - \sqrt{D_{34}}}{2}} \right] \left[\frac{\left(-\frac{E}{2}\right) [2E\rho_1 + \alpha_2 S_1^-] + S_2^+ \alpha_3 S_1^-}{(-\gamma_p \rho_1 + (S_1^-)^2)(-E^2 + (S_2^+)^2)} \right] \tag{D.31}$$

$$c_1 = \left[\frac{\gamma_p E^2}{\Lambda_1^{(0)} + \frac{(\gamma_g + \gamma_{2-g}) + \sqrt{D_{34}}}{2}} \right] \left[\frac{\left(-\frac{E}{2}\right) [2E\rho_1 + \alpha_2 S_1^-] + S_2^- \alpha_3 S_1^-}{(-\gamma_p \rho_1 + (S_1^-)^2)(-E^2 + (S_2^-)^2)} \right] \tag{D.32}$$

where we have introduced the variables:

$$\begin{aligned}
\rho_1 &= -\frac{\gamma_{2,eff}(2\nu_0 - 1)}{2}, & \alpha_2 &= E \left[1 + (\nu_0 - 1) \frac{\gamma_{2,eff}}{\gamma_{2,g}} \right], & \alpha_3 &= -\gamma_{2,eff} \frac{(\nu_0 - 1)}{2}, \\
S_1^- &= -\frac{\gamma_-}{2} - \frac{\sqrt{\gamma_+^2 - \Omega^2 - 2i\gamma_- \Omega + 4\gamma_p \gamma_{2,eff}(\nu_0 - 1)}}{2} + \frac{i\Omega}{2}, \\
S_2^+ &= -\frac{\gamma_-}{2} + \frac{\sqrt{\gamma_+^2 - \Omega^2 - 2i\gamma_- \Omega + 4\gamma_p \gamma_{2,eff}(\nu_0 - 1)}}{2} + \frac{i\Omega}{2} \\
S_2^+ &= \frac{\gamma_g - \gamma_{2,g} + \sqrt{D_{34}}}{2}, & S_2^- &= \frac{\gamma_g - \gamma_{2,g} - \sqrt{D_{34}}}{2}.
\end{aligned}$$

Finally, when we combine (D.19), (D.28)-(D.32) we find the eigenvalue of the matrix M which has the largest real part:

$$\begin{aligned}
\Lambda_1 \equiv \Lambda_{\max} &= \Lambda_1^{(0)} + \left[\frac{\gamma_p E^2}{\Lambda_1^{(0)} + \frac{(\gamma_g + \gamma_{2,g}) - \sqrt{D_{34}}}{2}} \right] \left[\frac{\left(-\frac{E}{2} \right) [2E\rho_1 + \alpha_2 S_1^-] + S_2^+ \alpha_3 S_1^-}{(-\gamma_p \rho_1 + (S_1^-)^2)(-E^2 + (S_2^+)^2)} \right] \\
&+ \left[\frac{\gamma_p E^2}{\Lambda_1^{(0)} + \frac{(\gamma_g + \gamma_{2,g}) + \sqrt{D_{34}}}{2}} \right] \left[\frac{\left(-\frac{E}{2} \right) [2E\rho_1 + \alpha_2 S_1^-] + S_2^- \alpha_3 S_1^-}{(-\gamma_p \rho_1 + (S_1^-)^2)(-E^2 + (S_2^-)^2)} \right]
\end{aligned} \tag{D.33}$$

Here $\Lambda_1^{(0)}$ is given in (D.19) [also in Eq. (4.2) in the main text-in slightly different form]:

$$\Lambda_1^{(0)} = -\frac{\gamma_+}{2} + \frac{\sqrt{\gamma_+^2 - \Omega^2 - 2i\gamma_- \Omega + 4\gamma_p \gamma_{2,eff}(\nu_0 - 1)}}{2} - \frac{i\Omega}{2}.$$

Note that from (D.33) after some algebra we find the real part of Λ_{\max} and recast it in the form of Eq. (4.4) in the main text and Appendix E.

Appendix E

The coefficients C_0 , C_1 , C_2 and C_3 in Eq. (4.4) read:

$$C_0 = -\frac{\rho}{\tau T_{2,eff}} \quad (\text{E.1})$$

$$C_1 = \frac{1}{\tau} \frac{E}{A^2 - T_{2,eff}^{-2}} \left(AE\rho + \frac{A\alpha}{T_{2,eff}} + \frac{2E\rho}{T_{2,eff}} + A^2\alpha \right) + \frac{2}{\tau} \frac{E^2 \rho (A + T_{2,eff}^{-1})}{(A^2 - T_{2,eff}^{-2})^2 T_{2,eff}^2} \quad (\text{E.2})$$

$$C_2 = -\frac{1}{\tau} \frac{E}{A^2 - T_{2,eff}^{-2}} \left(AE\rho + \frac{A\alpha}{T_{2,eff}} + \frac{2E\rho}{T_{2,eff}} + \frac{\alpha}{T_{2,eff}^2} \right) - \frac{2}{\tau} \frac{E^2 \rho (A + T_{2,eff}^{-1})}{(A^2 - T_{2,eff}^{-2})^2 T_{2,eff}^2} \quad (\text{E.3})$$

$$C_3 = \frac{2}{\tau} \frac{E^2 \rho (A + T_{2,eff}^{-1})}{(A^2 - T_{2,eff}^{-2}) T_{2,eff}^2} \quad (\text{E.4})$$

where we have introduced the following parameters:

$$\rho = -\frac{2\nu_0 - 1}{2T_{2,eff}}, \quad \alpha = \frac{E}{2} \left[1 + (\nu_0 - 1) \frac{T_{2,g}}{T_{2,eff}} \right], \quad A = \frac{1}{2T_g} + \frac{1}{2T_{2,g}} - \frac{1}{2} \sqrt{\left(\frac{1}{T_{2,g}} - \frac{1}{T_g} \right)^2 - 4E^2} \quad (\text{E.5})$$

This solution is valid when $\Omega_{Rabi} < T_{2,eff}^{-1}$ ($T_{2,eff}^{-1} \leq T_{2,g}^{-1}$ due to the diffusion terms).

In the range of pump rates around the RNGH instability threshold,

$\Omega_{Rabi}^2 \ll T_{2,eff}^{-2}$ (which assumes $p - \nu_0 \ll T_1 / T_{2,eff}$) and hence further

simplification of Eqs. (E.1)-(E.5) is possible, yielding, with accuracy to the correction terms of relative order $\Omega_{Rabi}^4 T_{2,eff}^2$ in Eq. (4.4),

$$C_1 \approx -\frac{1}{2\tau} \frac{T_g T_{2,g} E^2}{(T_g - T_{2,eff})^2} \left[\nu_0 \left(1 + 2 \frac{T_{2,eff}}{T_{2,g}} \right) - 1 \right] \cdot \left(1 + \frac{E^2 T_g^3 T_{2,g}}{(T_g - T_{2,g})(T_g - T_{2,eff})} \right) \quad (E.6)$$

$$C_2 \approx \frac{1}{2\tau} \frac{T_g^2 T_{2,g} E^2}{T_{2,eff} (T_g - T_{2,eff})^2} \left[\nu_0 \left(1 + \frac{T_{2,eff}}{T_g} \right) - 1 + \frac{T_{2,eff}}{T_{2,g}} \right] \quad (E.7)$$

$$C_3 \approx \frac{1}{\tau} \frac{E^2 T_g (2\nu_0 - 1)}{T_{2,eff}^2 (T_g - T_{2,eff})}, \quad A \approx \frac{1}{T_g} + \frac{T_g T_{2,g} E^2}{T_g - T_{2,g}} \approx \frac{1}{T_g} + \frac{1}{2} T_{2,g} \Omega_{Rabi}^2 \quad (E.8)$$

It follows that

$$-\frac{C_1}{C_0} \approx T_{2,g}^2 T_{2,eff}^2 \Omega_{Rabi}^4 \frac{1}{4} \frac{\nu_0 \left(1 + 2 T_{2,eff} T_{2,g}^{-1} \right) - 1}{2\nu_0 - 1} \cdot \left(1 + \frac{2}{\Omega_{Rabi}^2 T_g T_{2,g}} \right) \quad (E.9)$$

Therefore $-C_1 / C_0 \ll \frac{T_{2,g}}{T_g} \ll 1$ for the pump rates considered here.

Appendix F

In this appendix we solve an equation of the form $p - \nu(p) = \theta$ [see Eq. (4.7)] with respect to the pump rate p . Using expression for ν_0 from Eq. (2.14), after rearrangement of terms and squaring, we obtain:

$$\left(\frac{2\theta - p + \phi}{2}\right)^2 = \left(\frac{p + \phi}{2}\right)^2 - p\left(\phi - \frac{2T_1T_{2,eff}}{T_gT_{2,g}}\right) - \frac{2T_1T_{2,eff}}{T_gT_{2,g}} \quad (F.1)$$

Where we have introduced a new parameter

$$\varphi = 1 + \frac{T_{2,eff}}{T_{2,g}} + \frac{2T_1T_{2,eff}}{T_gT_{2,g}} \quad (F.2)$$

Eq. (F.1) is of the first order with respect to variable p . Its solution reads

$$p = 1 + \theta \left(1 + \left[\frac{2T_1}{T_g} + \frac{T_{2,g}}{T_{2,eff}} \theta \right]^{-1} \right) \quad (F.3)$$

Appendix G

Recurrence period density entropy (RPDE)

This method which is used in the field of dynamical systems and time series analysis measures repetitiveness in the phase space of the system and it has been successfully used to detect abnormalities in speech signal [113], [124].

A solution that satisfies Langevin equation:

$$\dot{\mathbf{x}} = \mathbf{f}(\mathbf{x}) + G(\mathbf{x})\xi \quad (\text{G.1})$$

we will call a trajectory. Here the state of the system at time t is represented by the phase space vector $\mathbf{x}(t)$ of size d , \mathbf{f} is a deterministic vector field and $G(\mathbf{x})\xi$ is a vector of stochastic forcing terms [114]. Recurrent trajectories are those that return to a given region of phase space [125]. Recurrence time statistics provide useful information about the properties of both purely deterministic dynamical systems and stochastic systems [125]. Recurrence analysis forms the basis of the method of recurrence plots in nonlinear time series analysis [114]. Phase-space recurrence is defined as:

$$\mathbf{x}(t) \subset B(\mathbf{x}(t + \delta t), r) \quad (\text{G.2})$$

where $B(\mathbf{x}, r)$ is a ball of small radius r around the point \mathbf{x} in phase-space, and $\mathbf{x}(t) \not\subset B(\mathbf{x}(t + s), r)$ for $0 < s < \delta t$, where δt is called the recurrence time [113].

The RPDE method requires the embedding of a time series in phase space, which is carried out by forming m -dimensional time-delayed vectors (time-delay embedding) [114]:

$$\mathbf{x}_n = [x_n, x_{n-\tau}, \dots, x_{n-(m-1)\tau}] \quad (\text{G.3})$$

where *embedding time delay* and *embedding dimension* are denoted as τ and m respectively. Following the approach of [113], the method of close returns [126] is applied: a small ball $B(\mathbf{x}_{n_0}, r)$ of radius $r > 0$ is placed around the embedded data point \mathbf{x}_{n_0} . Trajectory is followed forward in time until $\|\mathbf{x}_{n_0} - \mathbf{x}_{n_0+k}\| > r$ (the trajectory leaves the ball) for some $k > 0$. The time n_1 at which the trajectory first returns to the same ball, when $\|\mathbf{x}_{n_0} - \mathbf{x}_{n_1}\| \leq r$, is recorded and the difference of the two times is the discrete recurrence time $T = n_1 - n_0$ [113]. When the same method is repeated for all the embedded data points \mathbf{x}_n we get a histogram of recurrence times $R(T)$ which when normalized gives us the recurrence time probability density $P(T)$. The normalized entropy which is a simple measure of any probability density (measures its average uncertainty):

$$H_{norm} = - \frac{\sum_{t=1}^{T_{max}} P(t) \ln P(t)}{\ln(T_{max})} \quad (\text{G.4})$$

represents the RPDE value, where is the largest recurrence value. For purely periodic signals $H_{norm} = 0$ whereas for uniform white noise $H_{norm} \approx 1$ [113]. For the prescription how to find optimal values of embedding parameters m and τ and optimal ball radius r see [113], [114], [127] (one must perform a systematic search for the optimal set of parameters).

Biographical details (in Serbian)

Никола (Ненад) Вуковић рођен је у Београду 5.5.1989. године где је завршио основну школу као ђак генерације и носилац награда са републичких такмичења из математике. Математичку гимназију завршио је са одличним успехом и на основу награде са републичког такмичења из физике 2008. године, уписао је Електротехнички факултет без полагања пријемног испита. Дипломирао је 2012. на Одсеку за физичку електронику, смер Наноелектроника, оптоелектроника и ласерска техника (НОЛТ) са просеком 9.70, затим је био на двомесечној стручној пракси у Немачкој, на Универзитету у Килу². Мастер студије уписао је 2012. године на модулу НОЛТ и завршио их са просечном оценом 10.00 у септембру 2013. Тема мастер рада је „Утицај непараболичности на електронску структуру квантног каскадног ласера“, а ментор је проф. др Јелена Радовановић. Током завршне године основних и током мастер студија био је стипендиста Фонда за младе таленте републике Србије - Доситеја. У октобру 2013. уписао је докторске студије на изборном подручју Наноелектроника и фотоника и у међувремену је положио све испите (10) на докторским студијама са просечном оценом 10.00. Од јануара 2014. године запослен је на Електротехничком факултету у Београду као учесник на пројекту

² *Christian-Albrechts-Universität zu Kiel, Faculty of Engineering, Institute of Electrical Engineering and Information Technology (EE&IT), Chair of Communications.*

Министарства просвете, науке и технолошког развоја, а учествовао је и на још неколико међународних пројеката. Током 2015. и 2017. године у оквиру COST акције VM1205 боравио је три пута по месец дана у научној посети код др Дмитрија Боика у *Centre Suisse d'Electronique et de Microtechnique* (CSEM) у Нушателу (Швајцарска) и обављао активности везане за пројекте FastIQ и VM1205. Од 1. октобра 2017. године је у звању асистента, а пре тога је био у звањима истраживач-приправник и истраживач-сарадник. Током досадашњег научно-истраживачког рада објавио је 6 радова у часописима са импакт фактором, од тога 2 рада у врхунским међународним часописима категорије M21, као и 15 радова на конференцијама.

Списак публикација

Радови у врхунским међународним часописима (M21):

- [1] N. Vuković, J. Radovanović, V. Milanović, D. L. Boiko, "Low-threshold RNGH Instabilities in Quantum Cascade Lasers," *IEEE Journal of Selected Topics in Quantum Electronics* 23, 1200616 (1-16) (2017)., DOI: 10.1109/JSTQE.2017.2699139, ISSN 1077-260X, импакт фактор 3.971 (2016).
- [2] N. Vuković, J. Radovanović, V. Milanović, D. L. Boiko, "Analytical expression for Risken-Nummedal-Graham-Haken instability threshold in quantum cascade lasers," *Optics Express* 24, pp. 26911-26929, (2016). ISSN 1094-4087, импакт фактор 3.307 (2016).

Радови у истакнутим међународним часописима (M22):

- [3] N. Vuković, A. Daničić, J. Radovanović, V. Milanović, and D. Indjin, "Possibilities of achieving negative refraction in QCL-based semiconductor metamaterials in the THz spectral range," *Optical and Quantum Electronics* 47, 883-891, ISSN 0306-8919, (2015) импакт фактор 1.290.
- [4] N. Vuković, V. Milanović and J. Radovanović, "Influence of nonparabolicity on electronic structure of quantum cascade laser," *Physics Letters A* 378 (2014), pp. 2222-2225, DOI: 10.1016/j.physleta.2014.04.069, ISSN 0375-9601, импакт фактор 1.683 (2014).
- [5] N. Vuković, J. Radovanović and V. Milanović, "Enhanced modeling of band nonparabolicity with application to mid-IR quantum cascade laser structure," *Physica Scripta T* 162 (2014) 014014 (1-4), DOI:10.1088/0031-8949/2014/T162/014014, ISSN 0031-8949, импакт фактор 1.126 (2014).

Радови у међународним часописима (M23):

- [6] N. Vuković, J. Radovanović, V. Milanović, D. L. Boiko, "Multimode RNGH instabilities of Fabry - Perot cavity QCLs: impact of diffusion," *Optical and Quantum Electronics* 48, 254 (1-10), 2016. ISSN 0306-8919, импакт фактор 1.055 (2016).

Саопштење са међународног скупа штампано у целини (M33):

- [7] N. Vuković, A. Daničić, J. Radovanović and V. Milanović, "Conduction-band nonparabolicity and gain calculations for THz Quantum cascade laser in strong magnetic field," Proceedings of 1st International Conference on Electrical, Electronic and Computing Engineering IcETRAN Vrnjačka Banja, June 2-5 2014, pp. MOI2. 2. 1-4 (2014).

Саопштење са међународног скупа штампано у изводу (M34):

- [8] N. Vuković, J. Radovanovic, V. Milanovic, D. L. Boiko, "Self-pulsing in monolithic and external cavity mid-IR QCLs," International School and Conference on Photonics - PHOTONICA2017, Belgrade 08/2017, Book of Abstracts, p. 130, (2017).
- [9] N. Vuković, J. Radovanović, V. Milanović, D.L Boiko, "Self-pulsations in QCLs", International Quantum Cascade Lasers School & Workshop IQCLSW 2016, 4.-9. September 2016, Cambridge UK, Book of Abstracts, p.195-196, (2016).
- [10] N. Vuković, J. Radovanović, V. Milanović, D. L. Boiko, "Determination of RNGH Round-trip Gain in QCLs," 4th Annual Conference of COST Action MP1204 & SMMO2016 Conference, Lisbon, Portugal, 21.-24. March 2016, Book of Abstracts, P.08, (2016).
- [11] M. Dubajić, A. Daničić, N. Vuković, V. Milanović, J. Radovanović, "Possibilities of achieving negative refraction conditions in quantum well structures based on cubic nitrides," 4th Annual Conference of COST Action MP1204 & SMMO2016 Conference, Lisbon, Portugal, 21.-24. March 2016, Book of Abstracts, P.23, (2016).
- [12] N. Vukovic, J. Radovanovic, V. Milanovic, D.L. Boiko, "The Role of Carrier Diffusion in RNGH Instabilities of Quantum Cascade Lasers," Conference on Lasers and Electro-Optics Europe & European Quantum Electronics Conference, 21-25 June 2015 Munich, Advance programme, p. 202 (2015).
- [13] N. Vukovic, J. Radovanovic, V. Milanovic, D. L. Boiko, "Influence of Carrier Diffusion on RNGH Instabilities in Semiconductor Lasers," 3rd Annual Conference of COST Action MP1204 & 6th International

Conference on Semiconductor Mid-IR Materials and Optics-SMM02015, Book of Abstracts, p. 61, 8-11. April 2015, Prague, Czech Republic (2015).

- [14] N. Vukovic, J. Radovanovic, V. Milanovic, D. L. Boiko, "Determination of RNGH round-trip gain using bi-orthogonal perturbation approach," International School and Conference on Photonics - PHOTONICA2015, Belgrade 08/2015, Book of Abstracts, p. 126, (2015).
- [15] A. Danicic, N.Vukovic, J. Radovanovic, V. Milanovic, "Modeling and applications of Quantum Cascade in external magnetic field," International School and Conference on Photonics - PHOTONICA2015, Belgrade 08/2015, Book of Abstracts, p. 38, (2015).
- [16] N. Vuković, A. Daničić, J. Radovanović and V. Milanović, "Effects of Conduction-band Nonparabolicity on Electronic Structure and Gain of THz Quantum Cascade Laser in Magnetic field," International quantum cascade lasers school & workshop 2014 , 7-14. September 2014, Policoro, Italy, Workbook, pp. 242-243 (2014).
- [17] N. Vuković, J. Radovanović, V. Milanović and D. L. Boiko, "Exploring the relation between Risken-Nummedal-Graham-Haken instabilities and conditions for superradiance in a quantum cascade laser," European Semiconductor Laser Workshop 2014 , Workbook, 18-19. September 2014, Paris, France (2014).
- [18] A. Daničić, N. Vuković, J. Radovanović, V. Milanović, "Realization of negative refraction in the THz spectral range via quantum cascades," STSM Workshop & Management Committee Meeting, 13-15. November 2014, Warsaw, Poland, Workbook, (2014).
- [19] N. Vukovic, J. Radovanovic, V. Milanovic, D. L. Boiko, "Investigation of Risken-Nummedal-Graham-Haken instabilities in quantum cascade lasers," 13th YOUNG RESEARCHERS' CONFERENCE, Materials Science and Engineering, Belgrade 12/2014. Book of Abstracts, p. 18, (2014).

Саопштење са скупа националног значаја штампано у изводу (M64):

- [20] N. Vuković, J. Radovanović, V. Milanović, D. Boiko, "Recent progress on RNGH Instabilities in QCLs," 9th Photonics Workshop, Kopaonik, Serbia, March 2-6, 2016., Book of Abstracts, p. 20, (2016).
- [21] N. Vukovic, J. Radovanovic, V. Milanovic, D. L. Boiko, "Multimode Risken-Nummedal-Graham-Haken Instabilities of Fabry-Perot Cavity Quantum Cascade Laser," 8th Photonics Workshop, Kopaonik, Serbia, March 2015., Book of Abstracts, p. 28, (2015).

Остало:

- [22] N. Vuković, "Investigation of RNGH instabilities in quantum cascade lasers," in *SKIN AND TISSUE CANCER DETECTION USING LASER IMAGING The Book of Scientific Reports*, 1st ed., Ž. Cvejić, J. Radovanović, and D. Indjin, Eds. Novi Sad, Serbia: Liberte, 2017, pp. 112–116.
- [23] N. Vuković, "Travelling wave model for external cavity QCL," in *SKIN AND TISSUE CANCER DETECTION USING LASER IMAGING The Book of Scientific Reports*, 1st ed., Ž. Cvejić, J. Radovanović, and D. Indjin, Eds. Novi Sad, Serbia: Liberte, 2017, pp. 242–245.

Прилог 1.

Изјава о ауторству

Име и презиме аутора: Никола (Ненад) Вуковић

Број индекса: 2013/5015

Изјављујем

да је докторска дисертација под насловом:

"Рискен-Нумедал-Грахам-Хакен нестабилности и само-пулсирање у квантним каскадним ласерима" (енгл. "Risken-Nummedal-Graham-Haken instabilities and self-pulsing in quantum cascade lasers").

- резултат сопственог истраживачког рада;
- да дисертација у целини ни у деловима није била предложена за стицање друге дипломе према студијским програмима других високошколских установа;
- да су резултати коректно наведени и
- да нисам кршио ауторска права и користио интелектуалну својину других лица.

Потпис докторанда

У Београду, 26.02.2018.

Никола Вуковић

Прилог 2.

**Изјава о истоветности штампане и електронске верзије
докторског рада**

Име и презиме аутора: Никола (Ненад) Вуковић

Број индекса: 2013/5015

Студијски програм: Електротехника и рачунарство (модул Наноелектроника и фотоника).

Наслов рада: "Рискен-Нумедал-Грахам-Хакен нестабилности и само-пулсирање у квантним каскадним ласерима" (енгл. "Risken-Nummedal-Graham-Haken instabilities and self-pulsing in quantum cascade lasers").

Ментор: др Јелена Радовановић, редовни професор

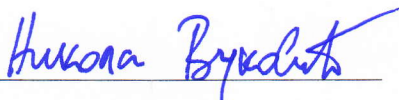
Изјављујем да је штампана верзија мог докторског рада истоветна електронској верзији коју сам предао/ла за објављивање на порталу **Дигиталног репозиторијума Универзитета у Београду.**

Дозвољавам да се објаве моји лични подаци везани за добијање академског назива доктора наука, као што су име и презиме, година и место рођења и датум одбране рада.

Ови лични подаци могу се објавити на мрежним страницама дигиталне библиотеке, у електронском каталогу и у публикацијама Универзитета у Београду.

Потпис докторанда

У Београду, 26.02.2018.



Прилог 3.

Изјава о коришћењу

Овлашћујем Универзитетску библиотеку „Светозар Марковић“ да у Дигитални репозиторијум Универзитета у Београду унесе моју докторску дисертацију под насловом:

"Рискен-Нумедал-Грахам-Хакен нестабилности и само-пулсирање у квантним каскадним ласерима" (енгл. "Risken-Nummedal-Graham-Haken instabilities and self-pulsing in quantum cascade lasers")

која је моје ауторско дело.

Дисертацију са свим прилозима предао/ла сам у електронском формату погодном за трајно архивирање.

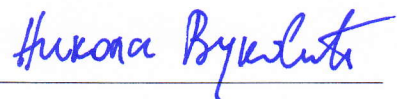
Моју докторску дисертацију похрањену у Дигиталном репозиторијуму Универзитета у Београду и доступну у отвореном приступу могу да користе сви који поштују одредбе садржане у одабраном типу лиценце Креативне заједнице (Creative Commons) за коју сам се одлучио.

1. Ауторство (CC BY)
2. Ауторство – некомерцијално (CC BY-NC)
3. Ауторство – некомерцијално – без прерада (CC BY-NC-ND)
4. Ауторство – некомерцијално – делити под истим условима (CC BY-NC-SA)
5. Ауторство – без прерада (CC BY-ND)
6. Ауторство – делити под истим условима (CC BY-SA)

(Молимо да заокружите само једну од шест понуђених лиценци. Кратак опис лиценци је саставни део ове изјаве).

Потпис докторанда

У Београду, 26.02.2018.



1. **Ауторство.** Дозвољаваате умножавање, дистрибуцију и јавно саопштавање дела, и прераде, ако се наведе име аутора на начин одређен од стране аутора или даваоца лиценце, чак и у комерцијалне сврхе. Ово је најслободнија од свих лиценци.
2. **Ауторство – некомерцијално.** Дозвољаваате умножавање, дистрибуцију и јавно саопштавање дела, и прераде, ако се наведе име аутора на начин одређен од стране аутора или даваоца лиценце. Ова лиценца не дозвољава комерцијалну употребу дела.
3. **Ауторство – некомерцијално – без прерада.** Дозвољаваате умножавање, дистрибуцију и јавно саопштавање дела, без промена, преобликовања или употребе дела у свом делу, ако се наведе име аутора на начин одређен од стране аутора или даваоца лиценце. Ова лиценца не дозвољава комерцијалну употребу дела. У односу на све остале лиценце, овом лиценцом се ограничава највећи обим права коришћења дела.
4. **Ауторство – некомерцијално – делити под истим условима.** Дозвољаваате умножавање, дистрибуцију и јавно саопштавање дела, и прераде, ако се наведе име аутора на начин одређен од стране аутора или даваоца лиценце и ако се прерада дистрибуира под истом или сличном лиценцом. Ова лиценца не дозвољава комерцијалну употребу дела и прерада.
5. **Ауторство – без прерада.** Дозвољаваате умножавање, дистрибуцију и јавно саопштавање дела, без промена, преобликовања или употребе дела у свом делу, ако се наведе име аутора на начин одређен од стране аутора или даваоца лиценце. Ова лиценца дозвољава комерцијалну употребу дела.
6. **Ауторство – делити под истим условима.** Дозвољаваате умножавање, дистрибуцију и јавно саопштавање дела, и прераде, ако се наведе име аутора на начин одређен од стране аутора или даваоца лиценце и ако се прерада дистрибуира под истом или сличном лиценцом. Ова лиценца дозвољава комерцијалну употребу дела и прерада. Слична је софтверским лиценцама, односно лиценцама отвореног кода.